THE UNIVERSITY *of* EDINBURGH

Observation of excited Ω_c^0 states, and commissioning of the RICH detector

Sara Mitchell

Doctor of Philosophy
The University of Edinburgh
April 2022

Abstract

The first observation of the $\Omega_b^- \to \Xi_c^+ K^- \pi^-$ decay is reported using pp collision data at centre-of-mass energies of 7, 8 and 13 TeV collected by the LHCb experiment, corresponding to an integrated luminosity of 9 fb^{-1}. The excited Ω_c^{**0} states are studied in the $\Xi_c^+ K^-$ mass projection of the $\Omega_b^- \to \Xi_c^+ K^- \pi^-$ decays. Four states are observed

$$M(\Omega_c(3000)^0) = 2999.2 \pm 0.9\,(\text{stat}) \pm 0.9(\text{syst})\ \text{MeV/c}^2,$$
$$\Gamma(\Omega_c(3000)^0) = 4.8 \pm 2.1\,(\text{stat}) \pm 2.5\,(\text{syst})\ \text{MeV},$$

$$M(\Omega_c(3050)^0) = 3050.1 \pm 0.3\,(\text{stat}) \pm 0.2\,(\text{syst})\ \text{MeV/c}^2,$$
$$\Gamma(\Omega_c(3050)^0) < 1.6\ \text{MeV},\ 95\%\ \text{CL},$$

$$M(\Omega_c(3065)^0) = 3065.9 \pm 0.4\,(\text{stat}) \pm 0.4\,(\text{syst})\ \text{MeV/c}^2,$$
$$\Gamma(\Omega_c(3065)^0) = 1.7 \pm 1.0\,(\text{stat}) \pm 0.5\,(\text{syst})\ \text{MeV},$$

$$M(\Omega_c(3090)^0) = 3091.0 \pm 1.1\,(\text{stat}) \pm 1.0\,(\text{syst})\ \text{MeV/c}^2,$$
$$\Gamma(\Omega_c(3090)^0) = 7.4 \pm 3.1\,(\text{stat}) \pm 2.8\,(\text{syst})\ \text{MeV},$$

where the uncertainties are statistical and systematic, respectively. Each resonance has a significance larger than 6 standard deviations. This thesis will also summarise the work completed for the ring imaging Cherenkov detectors, including laboratory work for the commissioning of the detectors and the analysis of the signal induced noise for the multi-anode photomultiplier tubes.

Lay Summary

The standard model of particle physics describes fundamental particles and their interactions, however, it is not a perfect description of the world around us. The quark model provides an almost accurate description of the ground state baryons and mesons. Excited states of particles are achieved by ground state particles being at a higher energy level. Heavy quark effective theory is used to describe the spectrum of excited hadrons. Since the discovery of pentaquark candidates and other states the theoretical and experimental interest in studying excited states has massively escalated. The LHC has discovered 62 new hadrons in the past 10 years. The LHCb experiment at CERN was built to study heavy flavour physics, and has had a huge impact to the study of excited particles.

The analysis presented in this thesis uses data collected by the LHCb experiment in 2011 to 2012 and 2015 to 2018 to search for heavy baryons containing a c quark and to measure their spin.

Many measurements made by the LHCb experiment are currently statistically limited, in order to push the boundaries of experimental physics the detectors must be upgraded. The second part of this thesis describes the commissioning work completed for the ring imaging Cherenkov detector upgrade. The upgraded LHCb detector will be able to collect significantly larger data sets than in previous years.

Declaration

I declare that this thesis was composed by myself, that the work contained herein is my own except where explicitly stated otherwise in the text, and that this work has not been submitted for any other degree or professional qualification except as specified.

(*Sara Mitchell, April 2022*)

Acknowledgements

Firstly, I would like to thank my supervisor Franz Muheim for his support, guidance, and expertise throughout my PhD. I would also like to thank Marco Pappagallo for teaching me about spectroscopy and always helping whenever I needed it. His guidance and expertise in the $\Omega_b^- \to \Xi_c^+ K^- \pi^-$ analysis was invaluable, and his support throughout the past 3.5 years means a lot to me. I would like to express my gratitude to Silvia Gambetta and Giovanni Cavallero for sharing their knowledge on the RICH detector and commissioning. Your patience and support was greatly appreciated. A special thanks to Neofytos Themistokleous and Eleanor Jones for keeping me sane throughout my PhD, especially while thesis writing. Lastly, my gratitude goes to the members of the B2OC and Charm working groups for constructive feedback and many interesting discussions.

Thanks to the University of Edinburgh, CERN, the LHCb experiment, and SUPA for providing me with the resources and funding to do my research.

I would like to thank all the friends I have made before and during my PhD for making the past 3.5 years unforgettable. Finally, I would like to thank my family for all their support. Especially my mum for her constant guidance and for only ever being a phone call away.

Contents

List of Figures

List of Tables

Chapter 1

Introduction

The standard model of physics describes three of the fundamental forces and the classification of all known fundamental particles, called quarks and leptons. Hadrons are formed from quarks and the quark model provides a way to describe the ground state baryons and mesons. A large number of the particles described by the quark model have been confirmed experimentally. The mass spectra of heavy excited particles are predicted by heavy quark effective theory, but they are still largely unknown due to the difficulty of the theoretical calculations. This provides the motivation behind searching for the excited baryon states. The discovery of new baryons and the measurement of their properties such as their mass and quantum numbers could provide us with a deeper understanding of the hadronic structure and allow us to probe the limits of the quark model. Moreover, studying heavy flavour spectroscopy allows us to expand our knowledge of how conventional hadrons, tetraquarks and pentaquarks are formed. The experimental and theoretical interest in spectroscopy has accelerated in recent years due to the observations of pentaquark and tetraquark candidates. The LHCb experiment has made a large number of contributions to the spectroscopy of heavy baryons, by observing numerous new states [1–5]. The spectrum of excited Ω_c^0 states, comprised of a charm quark and two strange quarks, has drawn lots of attention due to the observation of five new narrow Ω_c^{**0} states in 2017. The subject of this thesis will use physics data collected by the LHCb experiment to search for the Ω_c^{**0} states in the decays of Ω_b^- baryons, which contain a beauty quark.

The physics theory needed for heavy flavour physics is described in Chapter 2, where the standard model of particle physics, the quark model, and heavy quark

effective theory will be discussed. Next, the Ω_c^0 baryon, including the experimental status such as: the discovery of the Ω_c^0 and Ω_c^{*0} baryons, the theoretical predictions, and our knowledge of how to determine its quantum numbers will be presented. Chapter 3 will describe the LHCb detector, with which the data analysed in this thesis were collected. Next, work completed for the ring imaging Cherenkov detector upgrade will be discussed, along with the plans for the upgrade.

The second half of this thesis will present the observation of excited Ω_c^0 states from $\Omega_b^- \to \Xi_c^+ K^- \pi^-$ decays. Chapter 5 will give details on the analysis, including the strategy, data sets, selection requirements, and the Ω_b^- mass distribution fit model. It will finish off with a few results and a brief summary. The strategy for finding the excited Ω_c^0 states in the $\Xi_c^+ K^-$ mass spectrum will then be detailed in Chapter 6, it will include the results found and the systematic studies. The concluding statement and outlook will be given in the final chapter.

Chapter 2

Theory

This chapter will describe the theoretical knowledge needed for the study of heavy flavour baryon spectroscopy. There will be a focus on the Ω_c^0 baryon, including its discovery and the experimental status. This is motivated by the analysis described in this thesis, namely the observation of the excited Ω_c^0 states (Ω_c^{**0}) in $\Omega_b^- \to \Xi_c^+ K^- \pi^-$ decays.

The standard model of particle physics will be presented first, followed by an overview of the quark model, explaining the spectrum of ground state mesons and baryons. There will be a review of how to determine the quantum numbers of heavy baryons, as well as a brief section on heavy quark effective theory. Finally, the Ω_c^0 baryon will be discussed, as well as its production from the Ω_b^- baryon.

2.1 The Standard Model of particle physics

The standard model (SM) is a framework, which describes three fundamental forces and the classification of all known fundamental particles. It correctly predicts how the strong, electromagnetic, and weak forces behave with matter via their force carriers, called gauge bosons. Fundamental particles cannot be broken up into smaller constituents. The SM contains 17 particles, including 12 fermions which are divided into six quarks and six leptons. This is shown in Fig. 2.1. The others are four gauge bosons and the Higgs boson. The Higgs mechanism allows particles to become massive and it has at least one scalar Higgs boson. It was the final piece of the SM, found in 2012 at the Large Hadron Collider (LHC). All

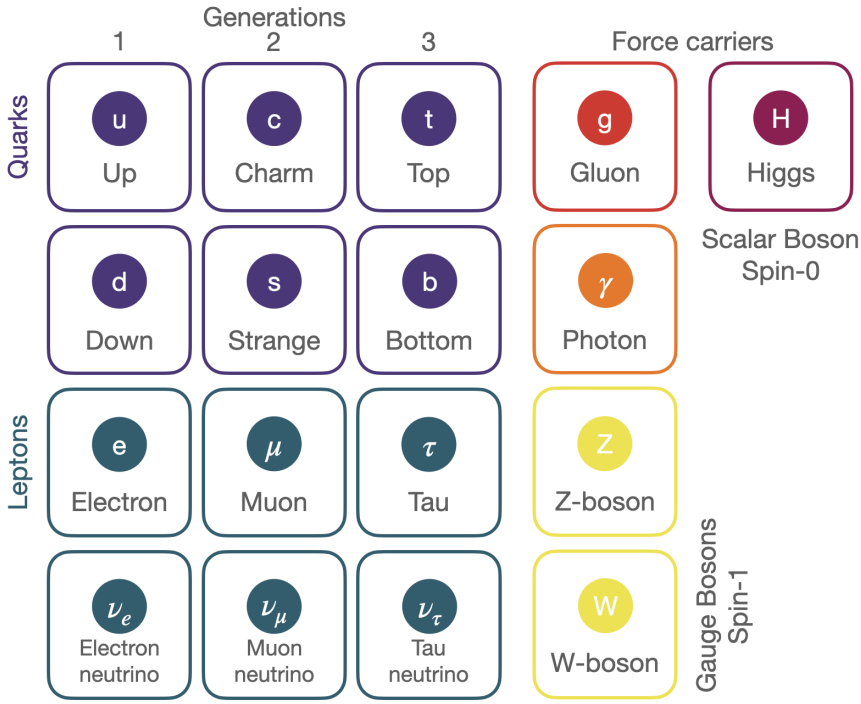

Figure 2.1 The standard model of particle physics. Showing the quarks, leptons, gauge bosons and the Higgs boson.

matter has an anti-matter partner, where the charge, Q, baryon number, $\mathcal{B}$, and the lepton number, $\mathcal{L}$, are reversed, but the mass is unchanged.

The first five rows in Table 2.1 lists the four gauge bosons and the Higgs boson, alongside their charge, spin, and mass. The force column indicates which force they interact with, where S denotes the strong force, EM denotes the electromagnetic force and W denotes the weak force. The gluons govern the strong force, photons mediate the electromagnetic force and the W- and Z-bosons carry the weak force.

Fundamental particles are classed as a fermion or a boson depending on its spin. Fermions, which make up all known matter, have half-integer spin. Bosons have integer spin and they govern how our fundamental forces interact. All bosons obey Bose-Einstein statistics, which describes how identical particles can occupy discrete energy states. This implies that the boson wave function is symmetric under exchange of two indistinguishable particles as they can occupy the same energy state. All fermions obey the Pauli exclusion principle, which dictates that two identical fermions cannot be in the same quantum state. This implies that the fermion wave function is anti-symmetric under exchange of two identical particles as they cannot occupy the same energy state. The fermions are split into quarks and leptons. Every fundamental force, omitting gravity, can interact with the

Table 2.1 All known fundamental particles in the standard model, including the gauge bosons and fermions. With their charge, spin, and mass listed. The forces which each particle interacts with is given by the right column. The information in this table is taken from the PDG [6].

Bosons	Charge	Spin	Mass [MeV/c^2]	Forces
Gluon	0	1	0	S
Photon (γ)	0	1	$< 1 \times 10^{-27}$	EM
W-boson	± 1	1	$(80.379 \pm 0.012) \times 10^3$	W
Z-boson	0	1	$(91.188 \pm 0.002) \times 10^3$	W
Higgs boson	0	0	$(125.25 \pm 0.17) \times 10^3$	-
Fermions	**Charge**	**Spin**	**Mass**	**Forces**
Up	$+2/3$	$1/2$	$2.16^{+0.49}_{-0.26}$	S,EM,W
Down	-1/3	$1/2$	$4.67^{+0.48}_{-0.17}$	S,EM,W
Charm	$+2/3$	$1/2$	$(1.27 \pm 0.02) \times 10^3$	S,EM,W
Strange	-1/3	$1/2$	93^{+11}_{-5}	S,EM,W
Top	$+2/3$	$1/2$	$(172.76 \pm 0.30) \times 10^3$	S,EM,W
Bottom	-1/3	$1/2$	$(4.18^{+0.03}_{-0.02}) \times 10^3$	S,EM,W
Electron	-1	$1/2$	0.51 ± 0.00	EM,W
Electron neutrino	0	$1/2$	< 0.000001	W
Muon	-1	$1/2$	105.66 ± 0.00	EM,W
Muon neutrino	0	$1/2$	< 0.19	W
Tau	-1	$1/2$	1776.86 ± 0.12	EM,W
Tau neutrino	0	$1/2$	< 18.2	W

quarks, however, only the electromagnetic and weak forces can interact with the leptons. The standard model cannot explain gravity and is incompatible with general relativity. The fermions are summarised in Table 2.1. The quarks only appear in bound states (hadrons) through a process called hadronisation, making their masses hard to measure. This gives rise to the large uncertainties on the light quark masses. Due to the large mass and short lifetime of the top quark, it decays too quickly to hadronise. Hadrons are states which contain quark and gluon fields and their quantum numbers are defined by the constituent quarks and antiquarks. The most common hadrons are mesons, which are a $q\overline{q}$ pair, and baryons, which consist of three quarks qqq. These are classified according to their baryon number, $\mathcal{B}$, where mesons have $\mathcal{B} = 0$, and baryons have $\mathcal{B} = 1$. Analogous to mesons and baryons, there are also the anti-mesons and anti-baryons. Recently, more complex states such as pentaquarks ($qqq\overline{q}q$) and tetraquarks ($\overline{q}q\overline{q}q$) have been observed [3, 7–9]. In 2003, the Belle collaboration discovered the X(3872) state, which has quark content $c\overline{c}u\overline{u}$ [10]. This state was confirmed by other experiments in later years. The Belle experiment also discovered the $Z^{+}(4430)$ tetraquark in 2007, which was later confirmed by the LHCb experiment [11]. The first pentaquark discoveries were seen by the LHCb experiment in 2015, named the $P_c^{+}(4380)$ and $P_c^{+}(4450)$ states, with quark content $uudc\overline{c}$ [12].

There are three generations of quarks and leptons, seen in Fig. 2.1. Quarks can interact with each other by changing flavour using the weak force, where a charged current process is given by:

$$q \rightarrow q' + W^{+}, \text{ where } q = u, c, t \text{ and } q' = d, s, b. \tag{2.1}$$

The Cabbibo-Kobayashi-Maskawa (CKM) matrix elements give information on the relative strength of the weak force for each flavour-changing interaction. The CKM matrix is given by:

$$V_{CKM} = \begin{pmatrix} V_{ud} & V_{us} & V_{ub} \\ V_{cd} & V_{cs} & V_{cb} \\ V_{td} & V_{ts} & V_{tb} \end{pmatrix} \tag{2.2}$$

where V_{ij} denotes the relative strength of the i- and j-quark undergoing a flavour changing interaction. The diagonal matrix elements describe the internal interactions of each generation and are close to one. This shows that quarks in the same generation are far more likely to interact with one another, compared to

their interactions with different generations. According to the SM the electroweak gauge bosons have an indistinguishable coupling to all three leptons, this means that decays to electrons, muons and taus happen with the same coupling strength, called lepton flavour universality (LFU). There are many models in beyond the standard model theories which involve violating LFU, and tests are currently being performed with the LHCb experiment [13, 14]. Evidence for LFU violation in b-quark decays at a significance of 3.1σ was recently published [15].

There are a few imperfections of the SM, it cannot explain baryon asymmetry and neutrino oscillations, or incorporate gravity and dark matter/energy. One of the main objectives of the LHCb experiment is to search for charge parity (CP) violation, which is one of the conditions to satisfy the matter anti-matter asymmetry of the universe.

2.2 Group Theory

Group theory is necessary to describe the standard model as it helps us represent its symmetries. This section is based off the group theory explanations detailed in [16] and [17]. Symmetry implies that we can perform a transformation on a system, leaving the properties of that system unchanged. A group describes our symmetry, and is composed of a finite or infinite number of objects $G = \{g_1, g_2\}$, with an operation $\diamond$. The operation gives us the ability to combine two elements within the group. The properties of a group are as follows:

1. Closure: If $g_1, g_2 \in G \Rightarrow g_1 \diamond g_2 \in G$: combinations are also in the set.
2. Identity: If $I \in G, \Rightarrow \ I \diamond g_i = g_i$ for all $g_i \in G$: Identity does nothing.
3. Inverse: Every $g_i \in G$ has a $g_i^{-1} \in G$, giving $g_i \diamond g_i^{-1} = I$: Inverse can undo an operation.
4. Associativity: If $g_1, g_2, g_3 \in G \Rightarrow (g_1 \diamond g_2) \diamond g_3 = g_1 \diamond (g_2 \diamond g_3)$: Combinations can be rearranged.

Checking all four properties allows you to determine whether your set of objects is a group or not. The groups which we focus on in particle physics are sets of complex matrices, where the combining operation is multiplication. Every element in a group can be described by a matrix, called the representations of

the group. This means that for every $g \in G$ there is a matrix M_g such that $g_1 \diamond g_2 = g_3 \Rightarrow M_{g1} M_{g2} = M_{g3}$. Going through the properties of a group; the identity can be represented by the identity matrix, all matrices within a group must have an inverse, and matrix multiplication is associative, satisfying the final property. It is hard to know what all the representations of one group are as you can combine representations together to get new ones. We want the non-redundant sets of matrices that describe a group, which cannot divide down any further. These are defined as the irreducible representations.

A group where the elements are continuous and differential (smooth) is defined as a *Lie Group*. The smooth functions have some finite set of parameters $\theta_a \in \mathcal{R}$, and the operation depends smoothly on those parameters. This means that,

$$g = g(\theta_1, ..., \theta_N) = \exp[i\theta_a \mathbf{T}^a] = \exp[i\bar{\theta}.\bar{\mathbf{T}}], \text{where } a = 1, ..., N$$
$$\text{and } \{\theta_a\} \text{ are continuous parameters,}$$

where $\mathbf{T}^a$ are the generators of the group. It is possible to know every element within a group if you know the generators. The generators hold all relevant information about a group. Most symmetries in physics are continuous symmetries, which is why Lie groups are so important. Most notably are the unitary and orthogonal groups. Some examples are provided in Table 2.2.

Table 2.2 Lie groups in particle physics

Group	Properties	Example
U(n)	$n \times n$ unitary ($U^\dagger U = 1$)	Electromagnetism U(1)
SU(n)	$n \times n$ unitary ($U^\dagger U = 1$) det U = 1	Weak SU(2) Strong SU(3)
O(n)	$n \times n$ orthogonal ($O^\dagger O = 1$)	Rotations and reflections O(3)
SO(n)	$n \times n$ orthogonal ($O^\dagger O = 1$) det O = 1	Rotations SO(3)

Quantum Electrodynamics

The electromagnetic, strong and weak forces that govern particle interactions can be expressed using Lie groups. Firstly, electromagnetic interactions are described using quantum electrodynamics (QED), where charged particles interact through the exchange of a photon. A U(1) gauge symmetry is required to represent QED and hypercharge (Y). It provides electric charge conservation and a massless gauge

boson. The hypercharge of a particle is given by:

$$Y = 2(Q - I_3), \text{ with } I_3 = \frac{1}{2}(n_u - n_d), \tag{2.3}$$

where Q denotes the electric charge, I_3 denotes the third component of isospin, and n_u and n_d denotes the number of up and down type quarks, respectively.

The Weak Force

An up quark can undergo a transformation to a down quark through an SU(2) transformation. The weak force is the only fundamental interaction in which quarks can change flavours, indicating that SU(2) describes the weak interaction. It is mediated by the two massive gauge bosons, $W^{\pm}$ and Z^0. The weak interaction is responsible for all decays involving leptons and ones in which a flavour change occurs.

Quantum Chromodynamics

The theory of strong interactions in the SM is described by quantum chromodynamics (QCD). Particles which can interact via the strong force are the quarks and gluons. QCD requires a SU(3) gauge symmetry to describe its interactions, where the gluon is the mediator. It carries another quantum number, referred to as colour (red, blue, and green). Each flavour of quark comes in three distinct types. The colour symmetry SU(3) is an exact symmetry as two quarks of the same flavour and different colour have the same mass, charge and all other quantum numbers. The $SU_C(3)$ colour group has 8 generators, described using the Gell-Mann λ-matrices [18]. Each gluon comprises of a colour and anti-colour, and there are 8 coloured gluons and one colourless state which cannot be involved in QCD interactions.

2.3 Quark Model

Hadrons are states which contain quark and gluon fields, where their quantum numbers are defined by the constituent quarks and anti-quarks. All quarks are restricted to be within bound states. The constituent quark model provides an

almost accurate description of the ground state baryons and mesons, which will be described in detail in this section. The model is not exact due to neglecting that hadrons contain gluons and sea quarks, therefore they are not pure 2- or 3-quark objects. Heavy quark effective theory is used to describe the spectrum of excited baryons, which will be discussed in a later section.

Mesons are comprised of a quark and an anti-quark, meaning that there should be $3 \times 3 \times 2 = 18$ distinct states when considering the three lightest quarks (3 flavours, 2 particles and 2 spins). The quark model predicts that all lowest mass mesons are either spin-0 (scalar mesons) or spin-1 (vector mesons). There are nine possible flavour combinations for the light mesons, containing u, d, and s quarks, which follows the SU(3) flavour symmetry. The SU(3) flavour symmetry is only approximate, due to the mass of the strange quark being slightly larger than the up and down quark. However, the flavour combinations can be grouped into an octet and a singlet,

$$\mathbf{3} \otimes \bar{\mathbf{3}} = \mathbf{8} \oplus \mathbf{1}, \tag{2.4}$$

where $\mathbf{3}/\bar{\mathbf{3}}$ defines the three quark/anti-quark flavours. It is possible to add the c quark to the light quarks to extend the flavour symmetry to SU(4). However, this symmetry is much more strongly broken than SU(3) due to the large mass of the c quark. The SU(4) representation gives 16 mesons, grouped into a 15-plet and a singlet,

$$\mathbf{4} \otimes \bar{\mathbf{4}} = \mathbf{15} \oplus \mathbf{1}. \tag{2.5}$$

Adding an extra quark to the above models extends this description to the baryon sector. The Pauli principle requires the baryon wave function to be fully anti-symmetric under exchange of any pair of quarks. It can be written as,

$$|qqq\rangle_A = |\psi\rangle_A \times |\text{space, spin, flavour}\rangle_S \tag{2.6}$$

where S and A denote symmetry or anti-symmetry under the interchange of any two equal-mass quarks. The colour wavefunction is given by,

$$|\psi\rangle = \frac{1}{\sqrt{6}}(|rbg\rangle - |brg\rangle + |bgr\rangle - |gbr\rangle + |grb\rangle - |rgb\rangle). \tag{2.7}$$

It must be fully anti-symmetric to ensure all baryons are colour-neutral. The quark model describes the lowest mass baryons, which are the ground state particles in S-wave, where S-, P-, and D-waves correspond to an angular momentum, L = 0, 1, and 2, respectively. The S-wave state is fully symmetric, leading to the

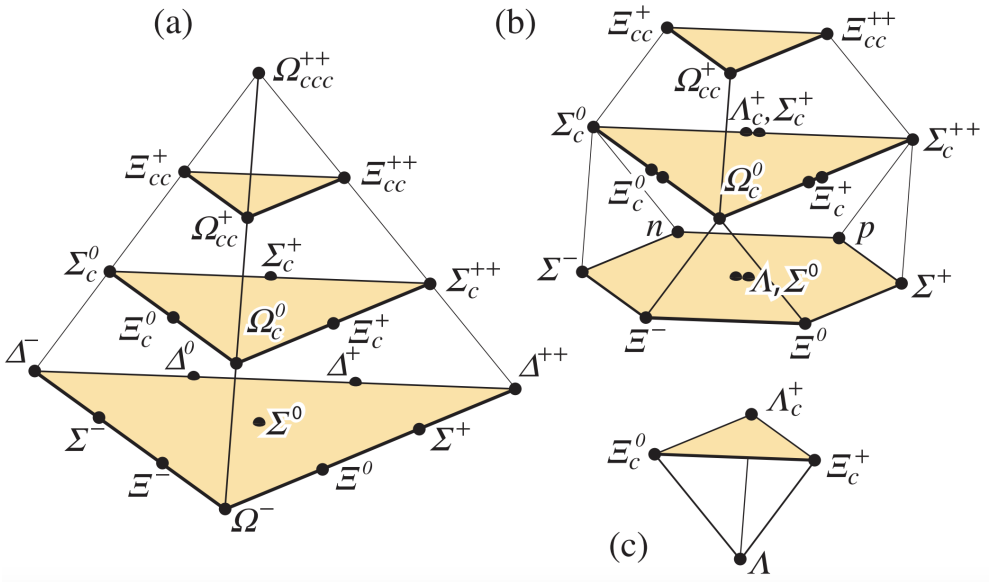

Figure 2.2 The SU(4) multiplets of baryons which are made of u, d, s and c quarks. (a) The 20_S-plet with the SU(3) decuplet on the bottom. (b) The $20'_M$-plet with an SU(3) octet on the bottom and (c) the 4_A-plet with the SU(3) singlet at the bottom. Figure from Ref. [19]

requirement of a fully symmetric spatial wavefunction under the interchange of quark position. The product of the spin and flavour wavefunctions must also be fully symmetric.

The lightest baryons are comprised of the three lightest quarks, u, d, and s. The three flavours give an approximate SU(3) flavour symmetry. This symmetry is broken due to the non-equal mass of the quarks. The flavour symmetry requires that baryons made of the lightest quarks must belong to four multiplets,

$$\mathbf{3} \otimes \mathbf{3} \otimes \mathbf{3} = \mathbf{10}_S \oplus \mathbf{8}_M \oplus \mathbf{8}_M \oplus \mathbf{1}_A, \tag{2.8}$$

where there is a symmetric decuplet, two mixed-symmetric octets and an anti-symmetric singlet. The flavour symmetry can be extended to SU(4) by the addition of the c quark, given by

$$\mathbf{4} \otimes \mathbf{4} \otimes \mathbf{4} = \mathbf{20}_S \oplus \mathbf{20'}_M \oplus \mathbf{20'}_M \oplus \mathbf{4}_A. \tag{2.9}$$

All particles within the same multiplet have the same spin and parity. Figure 2.2 shows the SU(4) baryon multiplets with their bottom levels as SU(3) multiplets. The symmetric $\mathbf{20}_S$ multiplet (Fig. 2.2(a)) has the SU(3) decuplet as a subset, where the spin-parity of each of the ground-state baryons is $J^P = \frac{3}{2}^+$. The mixed-

symmetric $\mathbf{20'}_M$ multiplet given in Fig. 2.2(b) consists of the SU(3) octet and have spin-parity $J^P = \frac{1}{2}^+$. Lastly, the anti-symmetric $\mathbf{4}_A$ multiplet is shown in Fig. 2.2(c) with $J^P = \frac{1}{2}^+$, involving the SU(3) singlet. For a fully anti-symmetric baryon wavefunction the spin part is required to be anti-symmetric. Fermi statistics forbid $\mathbf{4}_A$-plet states in the ground state.

All of the ground state baryons have been observed, however, many of the quantum numbers are yet to be measured. The quantum numbers can provide information on how the constituent quarks interact with one another, which will be described in detail in the following sections. The multiplets shown in Fig. 2.2 can be constructed replacing the c quark with a b quark, or it can be two sets of SU(4) within an SU(5) flavour symmetry group, accounting for all baryons containing u, d, s, c, and b quarks. The SU(4) and SU(5) multiplets are primarily used for determining the possible states as these symmetries are badly broken [20]. The main particle of interest throughout this work is the Ω_c^0 baryon, with quark content css and a spin-parity of $J^P = \frac{1}{2}^+$. The Ω_b^- baryon has quark composition bss and a spin-parity of $J^P = \frac{1}{2}^+$. This system is usually described in terms of the heavy b quark and the ss quark pair.

2.4 Singly heavy baryons

A baryon containing two light quarks and either one charm or bottom quark can be modelled as a diquark-quark system, where the light quarks act as a diquark. Modelling the baryons in this manor restricts the number of physical states, as a model with three independent quark degrees of freedom would provide a much richer spectrum.

The Ω_c^0 baryon has quark content css, where the ss quarks are modelled as a diquark. There are two ground state Ω_c^0 baryons, Ω_c^0 and $\Omega_c(2770)^0$, with quantum numbers $J^P = \frac{1}{2}^+$ and $J^P = \frac{3}{2}^+$, respectively. The Ω_c^0 baryon is in the sextet of flavour symmetric states with $J^P = \frac{1}{2}^+$ and $j_{qq} = 1$, and the $\Omega_c(2770)^0$ is in the SU(4) symmetric 20_S multiplet with $J^P = \frac{3}{2}^+$ and $j_{qq} = 1$. Here j_{qq} refers to the angular momentum of the light diquark system.

The quark-diquark system is modelled so that the heavy quark is considered alone, and it interacts with the light diquark. A diagram of this system is shown in Fig. 2.3 [21]. The following quantum numbers are used to characterise it: the

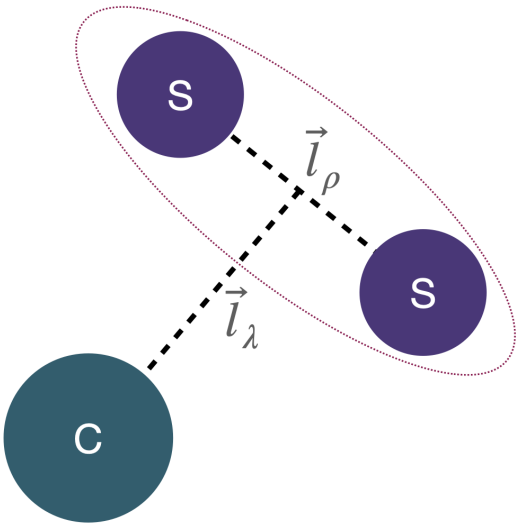

Figure 2.3 Model of the quark-diquark system

Table 2.3 Definitions of the relative quantum numbers for the diquark-quark model.

Quantum Number	Description
$\vec{l}_\rho$	Orbital angular momentum between the two light quarks
$\vec{l}_\lambda$	Orbital angular momentum between the heavy quark and the diquark system
$\vec{L} = \vec{l_\rho} + \vec{l_\lambda}$	Total orbital angular momentum
$\vec{s}_{qq} = \vec{s}_{q1} + \vec{s}_{q2}$	Sum of the light quark spins
$\vec{s}_{Q=b,c}$	Spin of the heavy quark
$\vec{j}_{qq} = \vec{L} + \vec{s}_{qq}$	Angular momentum of the diquark system
$\vec{J} = \vec{j}_{qq} + \vec{s}_Q$	Total angular momentum of the heavy baryon

orbital angular momentum between the two light quarks ($\vec{l_\rho}$), the orbital angular momentum between the diquark and the heavy quark system ($\vec{l_\lambda}$), the total orbital angular momentum ($\vec{L} = \vec{l_\rho} + \vec{l_\lambda}$), the sum of the light quark spins ($\vec{s}_{qq} = \vec{s}_{q1} + \vec{s}_{q2}$), the spin of the heavy quark ($\vec{s}_{Q=b,c}$), the angular momentum of the diquark system ($\vec{j}_{qq} = \vec{L} + \vec{s}_{qq}$) and the total angular momentum of the heavy baryon ($\vec{J} = \vec{j}_{qq} + \vec{s}_Q$). The quantum number definitions are listed in Tab. 2.3.

The states predicted by the quark model are constructed in the coupling scheme using the following equation [20]:

$$|J^P, L, s_{qq}\rangle = |[(l_\rho l_\lambda)_L (s_{qq} s_Q)_S]_J\rangle \tag{2.10}$$

where the $(ab)_c$ notation denotes that angular momentum c is formed by vector addition from angular momenta a and b, and the parity P is $(-1)^L = (-1)^{l_\rho + l_\lambda}$.

The expansion of Eq. 2.10 will give the definitions listed in Table 2.3.

2.5 Heavy Quark Effective Theory

Heavy quark effective theory [22–29] (HQET) aims to simplify the description of processes where a heavy quark is bound to a diquark within a hadron. It provides the footing for factoring out the dynamics of the heavy quark, up to corrections in the first order of $1/m_Q$, where m_Q is the heavy quark mass. The spectra of excited heavy baryons is extremely complicated and is estimated using HQET. This is possible due to the large difference between the masses of the heavy and light quarks. HQET holds for instances where $\Lambda_{QCD} << m_Q$, where Λ_{QCD} is the QCD energy scale (of order 200 MeV). The limit $m_{Q=b,c} \to \infty$ is imposed to predict the excitation spectrum of heavy baryons. Correction terms in powers of $1/m_Q$ are applied afterwards. When this limit is used, the spin and parity of the light degrees of freedom in a hadron are conserved, as well as the spin and parity of the heavy quark. A result of this is that strong decays of excited heavy baryons are only dependant on the light quarks, so the light quark quantum numbers are used to derive the selection rules for the decays. In order to determine the rules for the total baryon state, the spin and parity of the heavy quark is combined. The quark model predicts states for baryons containing a single heavy quark, whether these states respect HQET is a big question of interest.

For the light diquark with spin $j_{qq} > 0$, the total spin of the baryon is given by $J = j_{qq} \pm 1/2$. This produces a doublet of heavy hadrons, where the two states are nearly degenerate. The masses of the two states are only split by a chromomagnetic interaction, which scales as Λ^2_{QCD}/m_Q, where you get a suppression due to the large mass of the heavy quark. The following coupling scheme is used for the HQET states:

$$|J^P, j_{qq}\rangle = |\left\{[(l_\rho l_\lambda)_L s_{qq}]_j s_Q\right\}_J\rangle. \tag{2.11}$$

This scheme provides the characterisation of the ground states of the single charmed baryons. The quantum numbers are $|j_{qq} = 1, J^P = \frac{1}{2}^+\rangle$, $|j_{qq} = 0, J^P = \frac{1}{2}^+\rangle$, and $|j_{qq} = 1, J^P = \frac{3}{2}^+\rangle$. In the HQET description J^P and j_{qq} are 'good' quantum numbers and therefore must be preserved during a strong decay of one state into another. Experimental searches need to be performed to determine if the theoretical predictions from the HQET match the experimentally observed excited heavy baryon spectra. Hopefully the search for excited Ω_c^0 states, described in

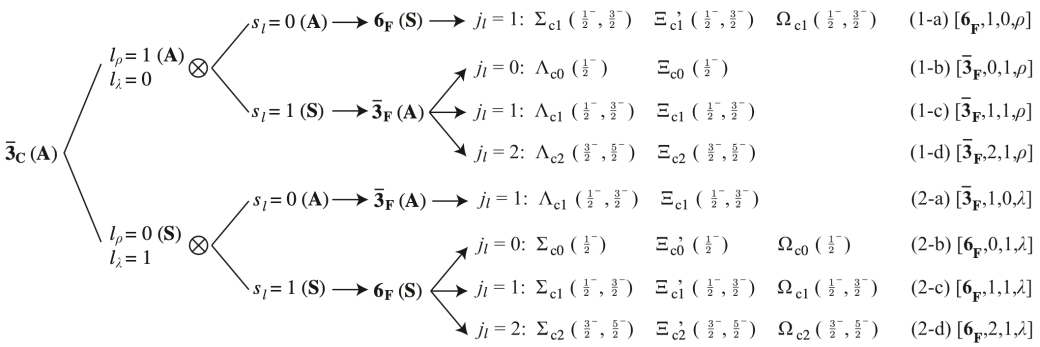

Figure 2.4 The notations for the P-wave charmed baryons. The $\mathbf{6}_F(\mathbf{S})$ and $\bar{\mathbf{3}}_F(\mathbf{A})$ groups denote the SU(3) flavour representations. The $\bar{\mathbf{3}}_C(\mathbf{A})$ is the SU(3) colour representation. The spin angular momentum of the light diquark is $s_l = s_{qq}$, and the total angular momentum of the light diquark is given by $j_l = j_{qq} = l_\lambda \otimes l_\rho \otimes s_l$. Figure from Ref. [32].

Chapter 6, will enable the exploration of this open question.

2.6 The Ω_c^0 baryon

Hints of the Ω_c^0 baryon were first seen by the CERN experiment WA-62 in the $\Xi^- K^- \pi^+ \pi^+$ final state [30]. There have been a lot of advancements in spectroscopy since then, and it has now been observed numerous times in a variety of final states. This section will discuss the predictions on the spin-parity of the excited Ω_c^0 states, its experimental status, and the motivations behind studying the excited Ω_c^0 states decaying into $\Xi_c^+ K^-$.

2.6.1 The P-wave excitations

The P-wave (L = 1) excitations can be acquired by the excitation of the angular momentum between the charm quark and the light diquark system ($l_\rho = 0$ and $l_\lambda = 1$) or between the two light quarks ($l_\rho = 1$ and $l_\lambda = 0$). There are seven P-wave Ω_c^0 states predicted, which reduce to five if the excitations between the two light quarks are neglected. Overall, five orbitally excited ($L = 1$) Ω_c^0 states are predicted due to the Pauli principle restricting the number of possible combinations. These are shown in Fig. 2.4, where there are two states with $J^P = 1/2^-$, two with $J^P = 3/2^-$, and one with $J^P = 5/2^-$ [6, 20, 21, 31–37].

In Fig. 2.4 the SU(3) flavour representations are denoted by the $\mathbf{6}_F(\mathbf{S})$ and $\bar{\mathbf{3}}_F(\mathbf{A})$,

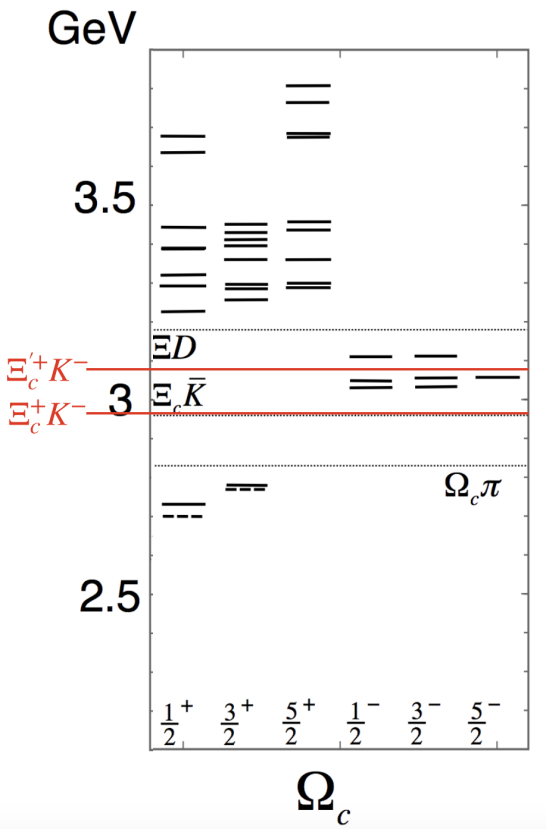

Figure 2.5 Predictions for the mass of many of the lowest lying Ω_c^0 baryons. The excited Ω_c^0 states which are predicted to decay into $\Xi_c^+ K^-$ are indicated between the red lines. The red line below 3 GeV indicates the $\Xi_c^+ K^-$ threshold and the other indicates the $\Xi_c'^+ K^-$ threshold. Figure from Ref. [20].

which correspond to the symmetric flavour sextet and anti-symmetric flavour triplet. The $\bar{\mathbf{3}}_C(\mathbf{A})$ corresponds to the anti-symmetric SU(3) colour symmetry. The notation j_l is equivalent to j_{qq} (angular momentum of the light diquark), and s_l is s_{qq}.

There are five excited Ω_c^0 states expected between the $\Xi_c^+ K^-$ and $\Xi_c'^+ K^-$ threshold, shown in Fig. 2.5. The predictions for the masses of the excited Ω_c^0 states spread over a large range of values. There are also predictions on the masses which are based on lattice calculations, shown in Fig. 2.6 [33, 38]. The sizes of the box are related to the uncertainties on their computation. The P-wave orbitally excited states are in the dotted box on the right side of the figure.

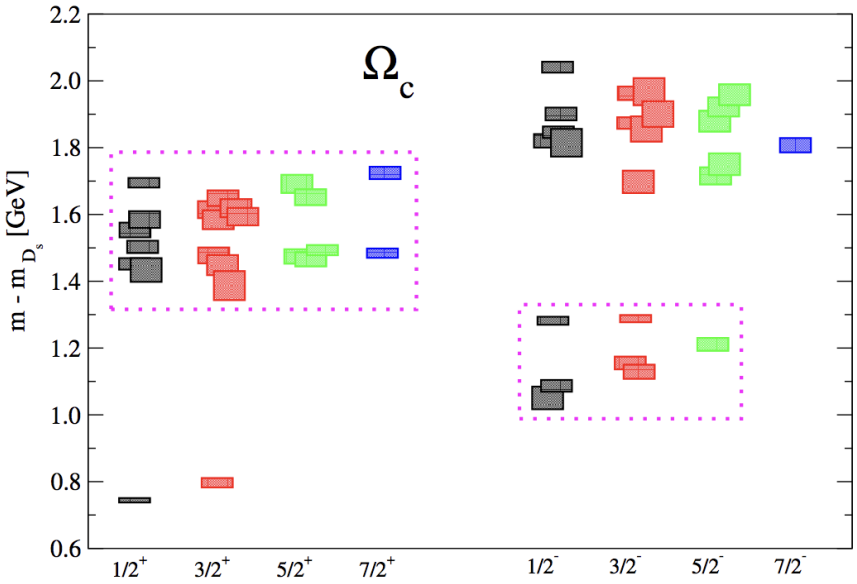

Figure 2.6 Mass predictions of the Ω_c^0 states with respect to the D_s mesons. The states in the dotted box on the left correspond to the D-wave radially excited states. The P-wave states are in the dotted box on the right side. The size of the boxes correspond to the uncertainties. Figure from Ref. [33]

2.6.2 Quantum numbers

It is possible to understand the excitations of baryons by considering the light degrees of freedom separately from the heavy quark. The low-lying states can be understood by the orbital excitations in the system of the heavy quark and diquark, where the diquark is in the lowest allowed state. The excitation spectrum of the diquark is shown in Fig. 2.7 (left). The Ω_c^0 baryon spectra is shown in Fig. 2.7 (right). For the Ω_c^0 baryon the lowest allowed diquark state is the 1^+ state, due to the two s-quarks giving a spatially and spin-symmetric 1S configuration.

The quark content of the Ω_c^0 baryon is css, therefore, the light quarks must be in a symmetric configuration overall (Eq. 2.6). Giving the diquark configuration as 1^+. The lowest levels of the baryon system with the diquark in the 1^+ configuration is; a doublet of 1S states ($1/2^+ \otimes 1^+$), five 1P states, and two 2S states (shown in Fig. 2.7 (right)). Orbital excitations of the diquark are often put down to the P-wave excitations as well, with anti-symmetric spin and anti-symmetric in space.

There are three main interpretations of the five observed Ω_c^0 states [5]:

1. The five 1P states with the 1^+ diquark configuration $(1/2^-, 1/2^-, 3/2^-, 3/2^-, 5/2^-)$.

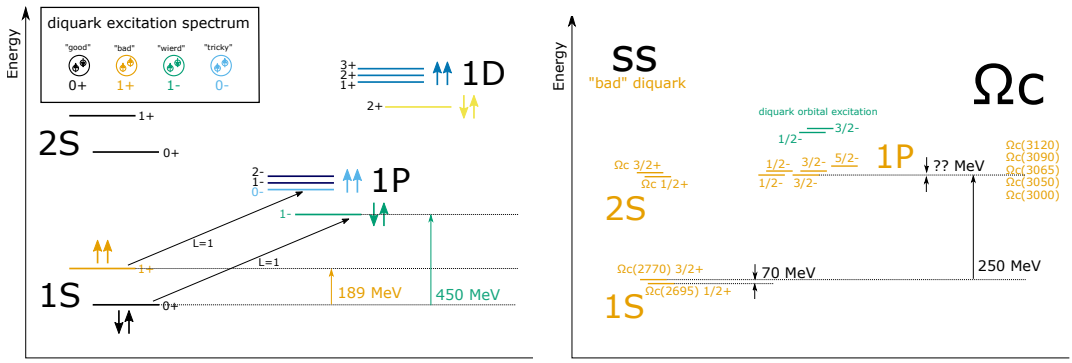

Figure 2.7 The left figure shows a schematic drawing of the light quark excitation. On the right is a schematic drawing of the Ω_c^0 baryon spectra. The coloured lines indicate the expected position of the hadron excitation with the colour corresponding to the levels in the diquark spectrum: 0^+ (black), 1^+ (orange), 1^- (green), and 0^- (blue). Labels attached to the levels represent the spin-parity J^P of the baryon. The quantum numbers in the system are given as 1S, 2S, 1P, and 1D.

2. The 2S and 1P states $(3/2^-, 3/2^-, 5/2^-, 1/2^+, 3/2^+)$. The relativistic potential model calculations show that the 2S states are in the region of the highest two peaks [39].

3. Some of the narrow states are suggested to be exotic (pentaquarks), with the others as P-wave states. The pentaquark states are suggested to have a positive parity, separating them from the P-wave states [40].

In summary, numerous theoretical calculations including; potential models, lattice QCD, and QCD sum rules interpret the newly discovered excited Ω_c^0 states [5] as orbitally or radially excited [20, 21, 31, 32, 38, 41–53]. A few studies suggest that their nature may be either molecular states or pentaquarks [54–59]. Note that the quark model calculations [20, 39, 49] do not agree with the order of the states in the 1P multiplet.

2.6.3 Experimental status

The Ω_c^0 baryon was at one point one of the least established charmed baryons. Numerous experimental groups searched for the Ω_c^0 baryon from a variety of decay modes, leading to significant differences in its calculated mass. The first evidence was found from the WA-62 experiment in the $\Xi^- K^- \pi^+ \pi^+$ decay mode at a mass of $2740.0 \pm 20.0\,\mathrm{MeV}/c^2$ [30], followed by another measurement by the ARGUS collaboration in the same final state at a mass of $2719.0 \pm 7.0(\mathrm{stat}) \pm$

$2.5(\text{syst})\,\text{MeV}/c^2$ [60]. The first observation of the Ω_c^0 baryon was seen in the $\Sigma^- K^- K^- \pi^+$ final state with a mass of $2699.9 \pm 1.5(\text{stat}) \pm 2.5(\text{syst})\,\text{MeV}/c^2$ by the E687 collaboration in 1994 [61]. The CLEO collaboration then confirmed this observation of the Ω_c^0 baryon by combining the $\Omega^-\pi^+$, $\Omega^-\pi^+\pi^0$, $\Xi^- K^-\pi^+\pi^+$, $\Xi^0 K^-\pi^+$, and $\Omega^-\pi^+\pi^+\pi^-$ final states, measuring a mass of $2694.6 \pm 2.6 \pm 1.9\,\text{MeV}/c^2$ [62].

The observation of the first excited Ω_c^0 baryon was found in the radiative decay to $\Omega_c^0\,\gamma$, with the Ω_c^0 baryon decaying to the $\Omega^-\pi^+$, $\Omega^-\pi^+\pi^0$, $\Omega^-\pi^+\pi^-\pi^+$, and $\Xi^- K^-\pi^+\pi^+$ final states. This Ω_c^{*0} state was found by the BaBar collaboration in 2006 [63], with a measured mass difference between the Ω_c^{*0} and Ω_c^0 baryons of $\Delta M = 70.8 \pm 1.0(\text{stat}) \pm 1.1(\text{syst})$ and a significance of 5.2σ.

Following from this, collaborations continued to measure the properties of the Ω_c^0 baryon and the excited state through many decay channels, but no new states were found. In 2017 the LHCb collaboration reported the observation of five new excited Ω_c^0 states decaying to $\Xi_c^+ K^-$ [5]. The search for excited Ω_c^0 states in the $\Xi_c^+ K^-$ mass spectrum was suggested in 1997 by G. Chiladze and A. Falk [31] due to the combination of the masses, $m(\Xi_c^+) + m(K^-)$, being the lowest hadronic threshold. Anything below this threshold can decay in one of two ways: either radiatively via the emission of a photon, or through an isospin-violating decay. The quantum numbers of the Ω_c^{**0} states may influence the width of the resonance due to the $\Omega_c^{**0} \to \Xi_c^+ K^-$ decay proceeding through different partial waves. States which proceed through D-wave transitions are predicted to be narrow, as well as P-wave transitions close to the kinematic threshold. In HQET the quantum numbers J^P and j_{qq} are conserved which affects the decay pattern of the excited states:

1. The lowest lying P-wave state, Ω_{c0} ($\frac{1}{2}^-$), can decay to $\Xi_c^+ K^-$ by an S-wave transition.

2. The next two P-wave states, Ω_{c1} ($\frac{1}{2}^-$ and $\frac{3}{2}^-$), cannot decay to $\Xi_c^+ K^-$ according to HQET. The decays to $\Xi_c^{'+}$ would be possible.

3. The final two P-wave states, Ω_{c2} ($\frac{3}{2}^-$ and $\frac{5}{2}^-$), can decay to $\Xi_c^+ K^-$ by a D-wave transition and are expected to be narrow.

The five excited Ω_c^0 states were observed in the prompt production of the Ω_c^0 baryon, where a promptly produced particle is one that is produced at the proton-proton collision point. The excited Ω_c^0 baryon decays strongly to $\Xi_c^+ K^-$, where the

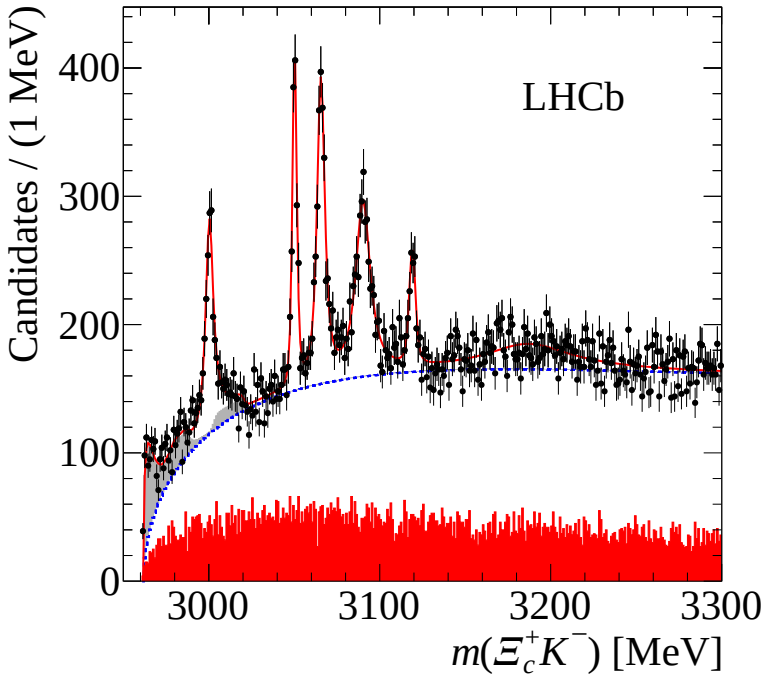

Figure 2.8 Invariant mass distribution of the $\Xi_c^+ K^-$ candidates. The total fit is shown by the solid red line, the blue dashed line indicates the background model, the light grey shaded area is due to feed-down components from partially reconstructed decays, and the solid red area is the Ξ_c^+ sidebands. Figure from Ref. [5].

Ξ_c^+ has quark content csu and decays weakly to $pK^-\pi^+$. The masses, widths, and yield of each state are shown in Table 2.4, where the first uncertainty is statistical and the second is systematic. Each state was observed with a significance of over 10 standard deviations (σ). Note that a sixth structure was added in the mass region around 3188 MeV to improve the fit shown in Fig. 2.8.

The quantum numbers have not been studied due to the unknown polarisation of the excited Ω_c^0 states. Therefore, no comparisons have been made to the HQET predictions. The states are also narrower than expected, giving further motivation for an investigation into these states using a different decay mode. This will hopefully provide us with a deeper insight to the nature of these states. It is possible that some of the signal observed could be partially reconstructed decays. For example, in the B^+K^- analysis three narrow peaks are observed [64]. Two of these peaks are partially reconstructed decays.

The list of currently observed Ω_c^0 states is given by Table 2.5, where the masses and widths are also provided. The spin-parity of the first two Ω_c^0 baryons are

Table 2.4 The measured mass and width of each excited Ω_c^0 state found in the prompt production of the Ω_c^0 [5]. The first uncertainty corresponds to statistical effects and the second is systematic.

Resonance	Mass [MeV]	Γ [MeV]	Yield
$\Omega_c(3000)^0$	$3000.4 \pm 0.2 \pm 0.1$	$4.5 \pm 0.6 \pm 0.3$	$1300 \pm 100 \pm 80$
$\Omega_c(3050)^0$	$3050.2 \pm 0.1 \pm 0.1$	$0.8 \pm 0.2 \pm 0.1$	$970 \pm 60 \pm 20$
		< 1.2 MeV, 95% CL	
$\Omega_c(3065)^0$	$3065.6 \pm 0.1 \pm 0.3$	$3.5 \pm 0.4 \pm 0.2$	$1740 \pm 100 \pm 50$
$\Omega_c(3090)^0$	$3090.2 \pm 0.3 \pm 0.5$	$8.7 \pm 1.0 \pm 0.8$	$2000 \pm 140 \pm 130$
$\Omega_c(3119)^0$	$3119.1 \pm 0.3 \pm 0.9$	$1.1 \pm 0.8 \pm 0.4$	$480 \pm 70 \pm 30$
		< 2.6 MeV, 96% CL	
$\Omega_c(3188)^0$	$3188.1 \pm 4.8 \pm 9.7$	$60.2 \pm 14.6 \pm 9.5$	$1668 \pm 451 \pm 525$

predicted from quark model calculations.

Table 2.5 List of observed Ω_c states, along with their measured masses, widths, and spin-parity which is inferred from quark model calculations. The first uncertainty is statistical and the second is systematic. Information taken from the PDG [6].

Particle	Mass [MeV]	Width [MeV]	J^P
Ω_c^0	2695.2 ± 1.7	-	$\frac{1}{2}^+$
$\Omega_c(2770)^0$	2765.9 ± 2.0	-	$\frac{3}{2}^+$
$\Omega_c(3000)^0$	$3000.4 \pm 0.2 \pm 0.1$	$4.5 \pm 0.6 \pm 0.3$	$?^?$
$\Omega_c(3050)^0$	$3050.2 \pm 0.1 \pm 0.1$	< 1.2, 95% CL	$?^?$
$\Omega_c(3065)^0$	$3065.6 \pm 0.1 \pm 0.3$	$3.5 \pm 0.4 \pm 0.2$	$?^?$
$\Omega_c(3090)^0$	$3090.2 \pm 0.3 \pm 0.5$	$8.7 \pm 1.0 \pm 0.8$	$?^?$
$\Omega_c(3120)^0$	$3119.1 \pm 0.3 \pm 0.9$	< 2.6, 95% CL	$?^?$

Measuring the spin-parity of the excited Ω_c^0 states is crucial in testing the validity of the HQET predictions, and it may help us understand why some of the states observed in the previous analysis [5] are so narrow by probing their structure. The best way to measure the quantum numbers is from the non-prompt production of the Ω_c^0 baryon, i.e. from the decay of a heavier baryon. This will give us the information on the polarisation of the heavy baryon, allowing for a test of spin-parity hypotheses. The polarisation of the Ω_c^{**0} states can be measured in Ω_b^- decays because the spin-parity of the Ω_b^- baryon is known. Therefore, the Ω_b^- baryon has a known polarisation, and is predicted to decay into the $\Xi_c^+ K^- \pi^-$ final state. The $\Omega_b^- \to \Xi_c^+ K^- \pi^-$ decay looks like the most promising final state and it is the subject of this thesis. The Ω_b^- decay can proceed via the Feynman diagram shown in Fig. 2.9. No previous searches of the $\Omega_b^- \to \Xi_c^+ K^- \pi^-$ have been performed by the LHCb collaboration to date, or any other collaboration. So this would be the first observation of this decay mode.

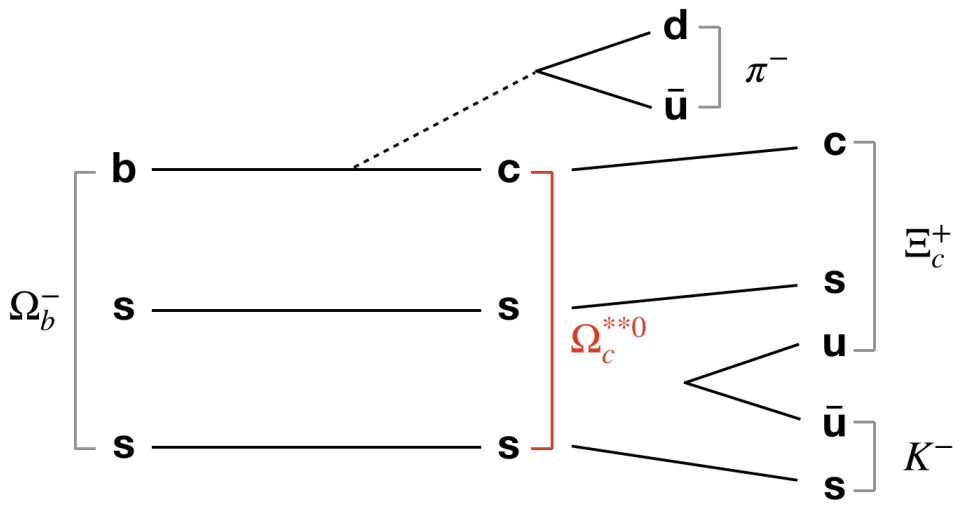

Figure 2.9 Lowest order Feynman diagram of the $\Omega_b^- \to \Xi_c^+ K^- \pi^-$ decay. The Ξ_c^+ decays weakly into $pK^-\pi^+$.

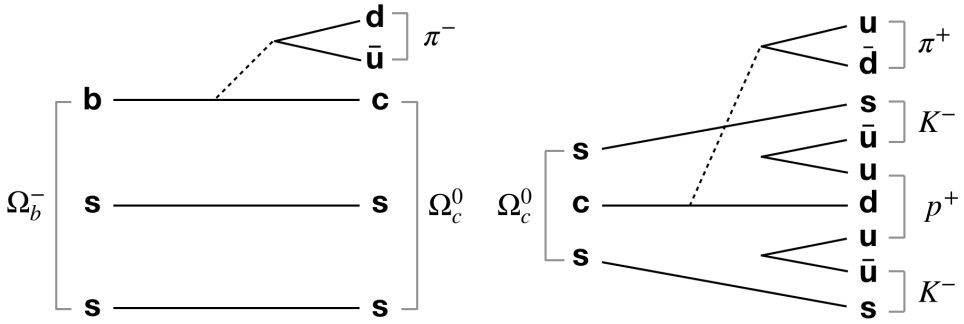

Figure 2.10 The lowest order Feynman diagram of the $\Omega_b^- \to \Omega_c^0 \pi^-$ decay.

The decay of $\Omega_b^- \to \Omega_c^0 \pi^-$ where the Ω_c^0 decays to $pK^-K^-\pi^+$ has been studied previously by the LHCb collaboration, where they made mass and lifetime measurements on the Ω_b^- baryon. From an experimental point of view the two decay modes are extremely similar due to the exact same final state, the only difference is in topology. These similarities allow this mode to be an excellent normalisation channel for calculating the relative branching ratio of the $\Omega_b^- \to \Xi_c^+ K^- \pi^-$ decay.

The lowest order Feynman diagram of the $\Omega_b^- \to \Omega_c^0 \pi^-$ decay is given in Fig. 2.10. The most recent measurement of the mass and lifetime of the Ω_b^- baryon was completed in 2016 by the LHCb collaboration. This study showed many sources of background in the Ω_b^- mass spectrum which may be helpful to consider in this analysis. The Ω_b^- baryon was found to have a mass of $6045.1 \pm 3.2 \pm 0.5 \pm 0.6\,\mathrm{MeV}/c^2$, and a significance of around 10σ. The results were shown to be consistent with

previous measurements [65].

Chapter 3

The LHCb Detector

3.1 The Large Hadron Collider

The large hadron collider (LHC) is a 27km ring of superconducting magnets which collides particles at extremely high energies. There are four main experiments stationed at different points along the ring, these are A Toroidal LHC ApparatuS (ATLAS), Compact Muon Solenoid (CMS), A Lead Ion Collision Experiment (ALICE) and LHC beauty (LHCb), shown in Fig. 3.1. The European Organisation for Nuclear Research (CERN) is where the LHC is located, it was built with the aim of discovering the Higgs boson, requiring extremely high energy collisions. When it last operated in 2018 it was capable of accelerating two beams of protons colliding at a centre-of-mass energy of $\sqrt{s} = 13$ TeV, this makes it the most powerful and largest particle accelerator to date.

Figure 3.1 shows the different accelerators and detectors at CERN. The protons travel through each accelerator, gradually gaining energy until they are of the required energy to enter the LHC. The protons are collected by ionising hydrogen gas, these are then accelerated in linear accelerator 2 (LINAC2) to an energy of 50 MeV which prepares them to enter the Proton Synchrotron Booster (PSB/BOOSTER). Next the protons are accelerated up to 1.4 GeV by the PSB, then to 25 GeV by the Proton Synchrotron (PS), where they are sent into the Super Proton Synchroton (SPS). The SPS is capable of accelerating the protons up to an energy of 450 GeV, once the desired energy is reached the protons are separated into two beams travelling in opposite directions and are sent into the

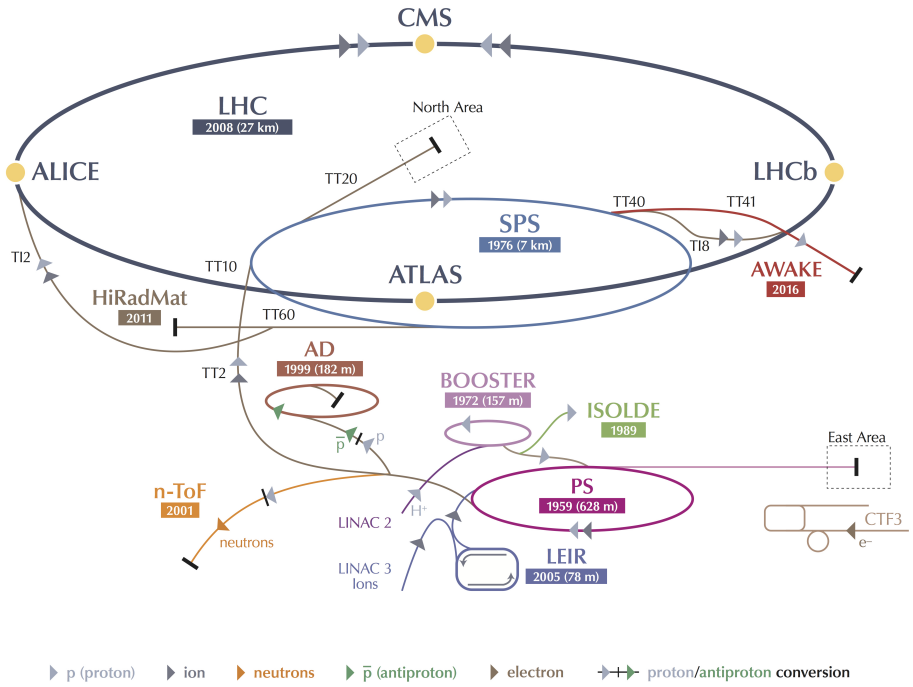

Figure 3.1 The CERN complex, showing the particle accelerators and detectors which are used at the LHC. Figure taken from Ref. [66].

LHC. The protons are grouped together in bunches of around 10^{11} particles per bunch.

The LHC started running in 2010 where it operated at energies of $\sqrt{s}$ = 7 and 8 TeV, the first long shutdown (LS1) was in 2013 where it prepared to run at $\sqrt{s}$ = 13 TeV from 2015 to 2018. The second long shutdown (LS2) started in December 2018, it is due to restart in 2022. The ATLAS and CMS experiments are both general purpose detectors, studying a large range of processes. ALICE is dedicated to heavy ion physics, specifically measuring collisions of lead nuclei. The LHCb experiment was built for the study of heavy flavour physics, this will be described in detail in the following sections.

3.2 The LHCb Detector

The LHCb detector is dedicated to observe rare decays of heavy hadrons, containing charm (c) and bottom (b) quarks, and measurements of charge-parity (CP) violation. It is a single-arm forward spectrometer covering the pseudorapidity

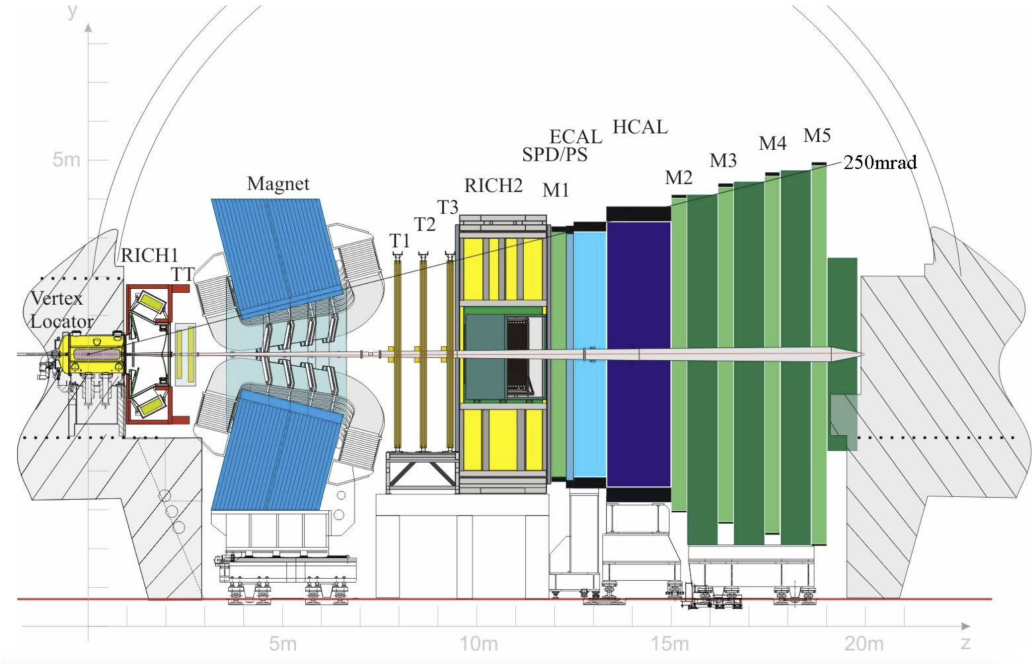

Figure 3.2 Cross section of the LHCb detector. Figure taken from Ref. [67].

range of $1.9 < \eta < 4.9$. Pseudorapidity is defined as:

$$\eta = -\log\tan(\theta/2)) \tag{3.1}$$

where θ is the angle between the particles momentum and the direction of the beam. Figure 3.2 shows a cross-section of the LHCb detector, the z-axis is in the direction of the beam and the y-axis is along the vertical direction. The pp collision takes place within the Vertex Locator (VELO), which provides tracking of the first particle interactions. The particles then travel into the first Ring Imaging Cherenkov Detector (RICH), which is used for accurate particle identification (PID) through the emission of Cherenkov radiation. Then they pass through the tracker turicensis (TT), followed by the magnet with a field of 4 Tm which bends the paths of charged particles. The magnet is succeeded by three trackers (T1-T3) and the second RICH detector. Following from this are the electronic (ECAL) and hadronic (HCAL) calorimeters where showers of particles are detected, and finally the set of muon chambers (M1-M5). The sub-detectors will be discussed in detail in the next sections.

The pseudorapidity range is chosen due to the b and $\bar{b}$ hadrons being predominantly produced in the forward and backward directions at high energies. Figure 3.3 shows the distribution of $b\bar{b}$ pairs using LHCb simulation at an energy of $\sqrt{s} = 14$ TeV. The red area shows the LHCb detector acceptance, where on average 1 in every 4

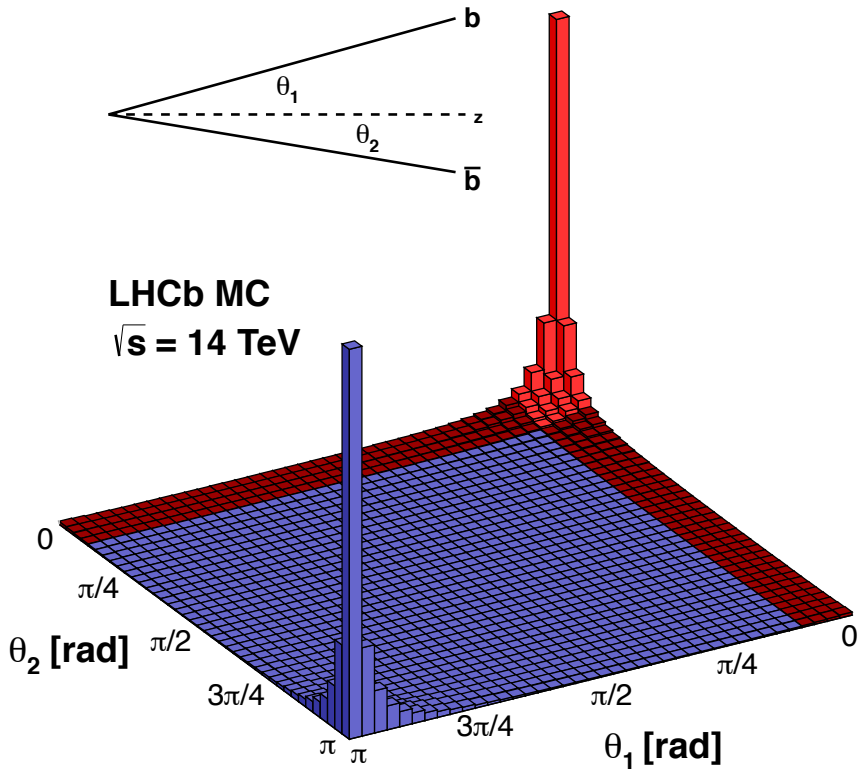

Figure 3.3 The simulated distribution of the $b\bar{b}$ pairs which are produced at $\sqrt{s} = 14$ TeV. The red area shows the LHCb detector acceptance. Figure taken from Ref. [68].

$b\bar{b}$ pair which is produced lies. The $b\bar{b}$ pairs are predominantly produced through gluon fusion, which occurs when two high-momentum gluons collide in the pp interaction. The $b\bar{b}$ pairs is boosted along the beam pipe, which is the direction of the high-momentum gluon.

The Run 1 data period refers to data collected in 2011 and 2012 and Run 2 data was collected in 2015 to 2018. Run 1 operated at centre-of-mass energies of $\sqrt{s} = 7$ and 8 TeV which at LHCb corresponds to an integrated luminosity of 3 fb^{-1} and Run 2 achieved $\sqrt{s} = 13$ TeV which gives an integrated luminosity of 6 fb^{-1}. Figure 3.4 shows the cumulative luminosity of LHCb over all data taking years. The total integrated luminosity at LHCb is currently 9.1 fb^{-1}.

3.3 Tracking System

The tracking system in LHCb is used to reconstruct the path which particles took while traversing the detector. This consists of the VELO, which is extremely

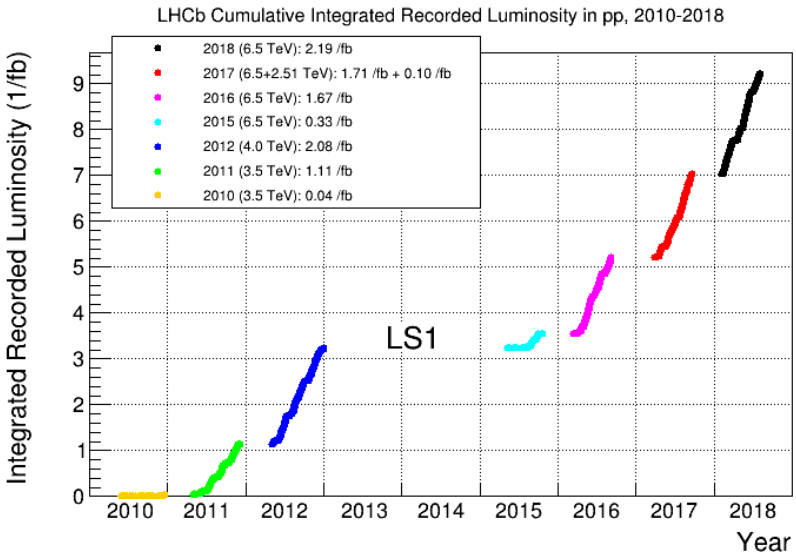

Figure 3.4 The cumulative integrated luminosity in pp collisions over all data taking years. Figure from Ref. [69]

close to the pp collision point, the TT before the dipole magnet and T1-T3 after the magnet. Silicon sensors are used for VELO, TT and the Inner Tracker (IT). Straw-tubes are used for the Outer Tracker (OT). The IT is the region close to the beam pipe for T1-T3 and the OT is on the outer region of these three trackers.

3.3.1 Vertex Locator

The VELO is designed to take precise measurements of particle trajectories close to the interaction point, with the most inner part being 8.2 mm away from the beam line. It is used to distinguish between the primary vertex (PV) and the displaced secondary vertex (SV). The SV is where the hadrons which contain b and c quarks decay. Figure 3.5 shows the cross-section of the VELO.

The VELO is made up of a series of silicon modules which are arranged along the beam direction, measuring the R and ϕ coordinates. There are 21 silicon modules in total. In Fig. 3.5 the R-type sensor is red and the ϕ-type sensor is blue. The R-type sensor consists of circular strips which measures the radius from the beam pipe and the ϕ-sensor is made up of radial strips which measures the azimuthal angle.

During injection of the protons the LHC requires an aperture which is larger than the VELO radius. To account for this the VELO is able to retract up to 30mm away from the beam line. Once a stable beam has been achieved the VELO can

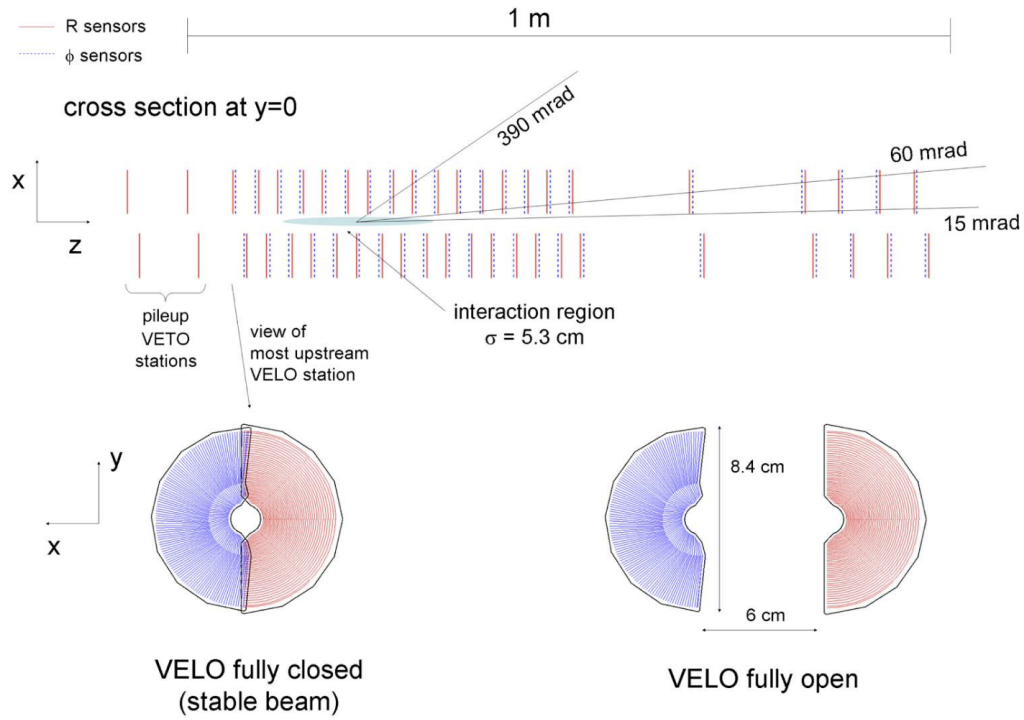

Figure 3.5 Cross section of the VELO. The R sensors are red and the ϕ sensors are in blue. Figure from Ref. [67].

be fully closed and data taking can start. A vacuum is maintained around the sensors, which is separated from the machine vacuum by aluminium foil. This minimises the amount of material the charged particles travel through.

3.3.2 Dipole Magnet

The momentum of charged particles can be determined by the degree that they're bent by due to a dipole magnet. The large dipole magnet used by the LHCb experiment has a total integrated magnetic field of 4 Tm. This value is found by integrating the magnetic field with respect to the length of the track. The magnetic field is known with a relative precision of around 10^{-4}. The magnet consists of a yoke with a weight of 1500 tons and two coils which weigh 54 tons. The two coils are saddle-shaped and are placed mirror-symmetrically to each other, creating the magnetic field. Each coil is made up of fifteen layers of hollow conductor with a cooling system. A perspective view of the magnet is shown in Fig. 3.6.

The magnet is placed after the TT and before T1-T3 to allow for the curvature of

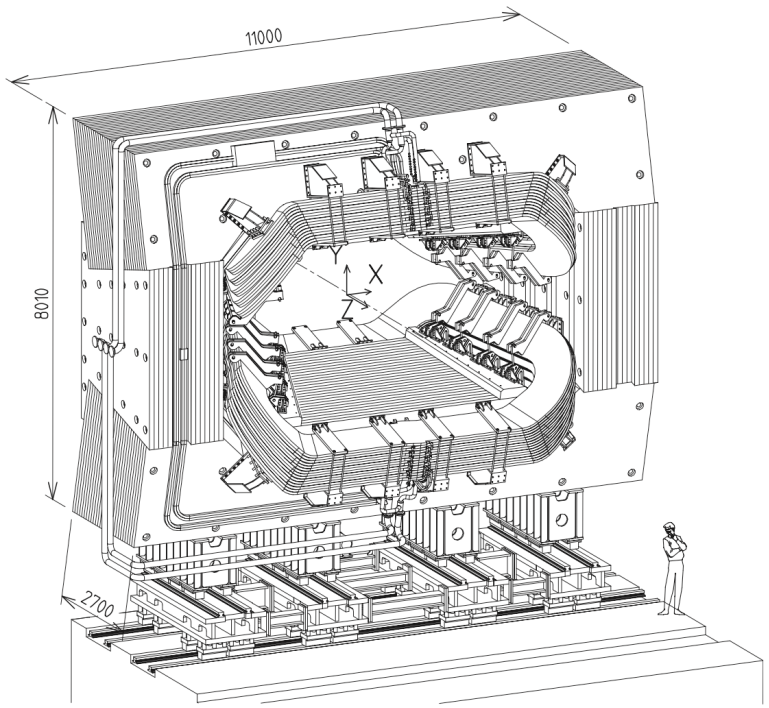

Figure 3.6 Perspective view of the LHCb magnet. The interaction point is behind the magnet. Figure from Ref. [67].

the particles to be reconstructed by the trackers. This is used to determine the momentum of the particle for any momentum up to 200 GeV/c with a momentum resolution of 1.0%. Two different configurations are used while data taking: magnet up, when the magnetic field is in the positive y-direction, and magnet down, which is in the negative y-direction. In order to reduce systematic effects of the detector the magnetic polarity is changed periodically, this reduces detector asymmetries between different datasets.

3.3.3 Silicon Tracker

The Tracker Turicensis (TT), which is upstream of the magnet, and Inner Tracker (IT), which is downstream of the magnet, are both parts of the Silicon Tracker (ST). Both the TT and IT use silicon microstrip sensors. The IT is the inner part of the T1-T3 trackers. The ST is installed close to the beam pipe due to the extremely high density of charged particles in this region. These silicon strips are designed to survive damage from radiation.

The TT is placed just after the VELO and hence it can be used to detect the decay of neutral particles which decay after it. One of the four layers is shown in

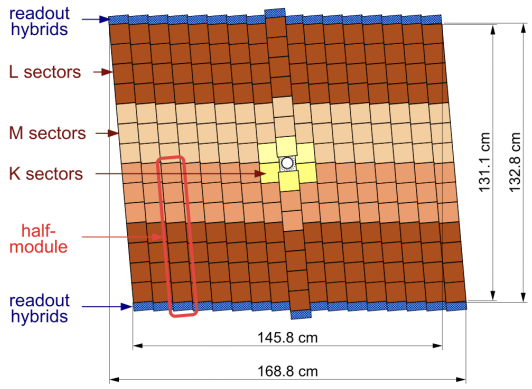

Figure 3.7 The layout of the third TT layer, the different shading indicates different readout sectors. Figure from Ref. [67].

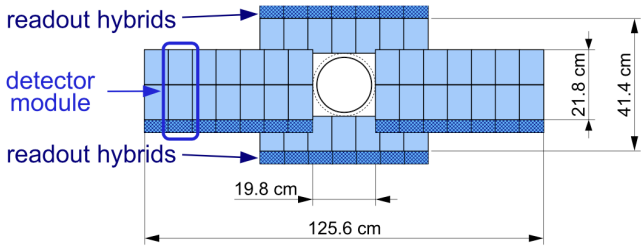

Figure 3.8 Layout of one of the Inner Trackers. Figure from Ref. [67].

Fig. 3.7, where the module covers the full LHCb acceptance. The half module indicated in Fig. 3.7 consists of 7 silicon sensors. There is a higher occupancy close to the beam line, to account for this different readout systems are used, which are indicated by the different shading of browns in Fig. 3.7.

Each IT is arranged from four detector boxes around the beam pipe, as shown in Fig. 3.8, and its dimensions are $1.2\ m\ \times\ 0.4\ m$. The IT is the inner region of the T1-T3 tracking stations which are located close to the beam pipe and downstream of the dipole magnet. The detector boxes in the vertical direction are larger due to the higher occupancy from the bending of the charged particles through the magnet.

3.3.4 Outer Tracker

The Outer Tracker (OT) is a large straw-tube detector which makes up the outer regions of the T1-T3 tracking stations. It tracks charged particles and measures their momentum through a drift-time detector which covers a large area of the LHCb acceptance. It delivers an extremely good momentum resolution which is

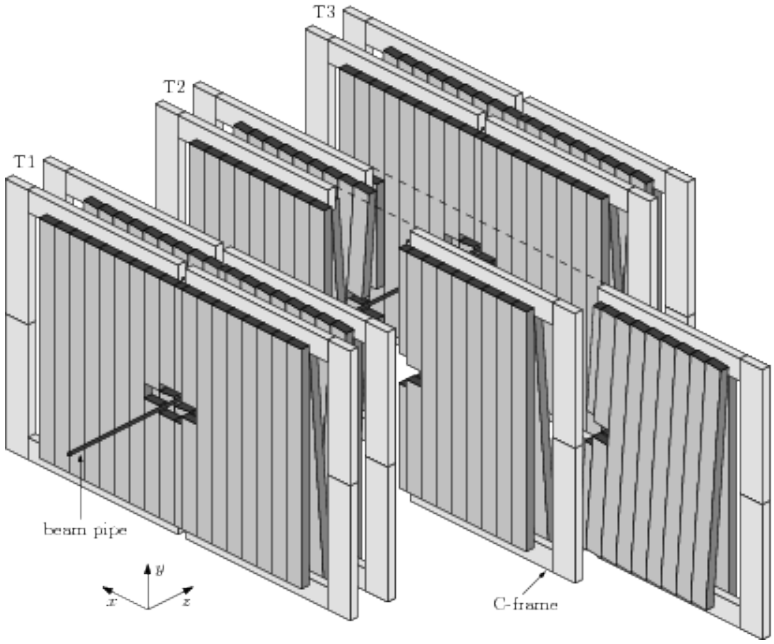

Figure 3.9 Layout of the OT straw-tube modules for T1-T3 [70].

required to precisely determine the invariant mass of the reconstructed b-hadrons. The three OT stations consist of four layers which are in the same configuration as the TT, where the middle two layers are rotated by $\pm 5°$. Figure 3.9 shows the layout of the OT. Each of the OT stations is comprised of two staggered layers of straw-tubes with an inner diameter of 4.9mm.

The total area covered corresponds to an acceptance of 300 mrad horizontally and 250 mrad vertically. To ensure a fast drift time (less than 50 ns) the straws are filled with a mixture of Argon (70%) and CO_2 (30%). The position of the charged particle track is reconstructed using the drift time and drift velocity.

3.4 Particle Identification

Analyses at the LHCb experiment require extremely good particle identification in order to make precise measurements on b-hadron physics, as it allows us to distinguish between pions and kaons. The particle identification (PID) system at LHCb was developed to precisely identify the different particle species which travel through the detector. The two ring imaging Cherenkov detectors (RICH) are used to distinguish between charged final state hadrons such as protons, pions and kaons. The PID system also includes two calorimeters, the electronic calorimeter (ECAL) and the hadronic calorimeter (HCAL). These determine the

energy released by photons, electrons and hadrons when traversing through the calorimeters. The final component is the muon chambers which identify the muons passing through the detector.

3.4.1 The RICH Detectors

The LHCb detector contains two Ring Imaging Cherenkov (RICH) detectors in order to cover the full momentum range that the particles reach. The RICH detectors exploit the emission of Cherenkov radiation. Cherenkov light is emitted from a particle when it's travelling faster than the speed of light in the medium it's travelling through. The photons are emitted in the direction of the particles momentum in a cone shape with an opening angle, θ_c. This is defined as:

$$\cos\theta_c = \frac{1}{n\beta}, \tag{3.2}$$

where n is the refractive index of the medium and $\beta = v/c$, where v is the velocity of the particle and c is the speed of light in a vacuum. The particle's mass can be determined by the combination of the Cherenkov angle with the momentum found from the tracking system. Figure 3.10 shows how θ_c varies over momentum for different particles, it is clear that at high momentum different particles are indistinguishable from each other. RICH1 is upstream of the magnet between the VELO and TT, it covers the low momentum particles in the range of around $1 - 60$ GeV/c and uses aerogel and C_4F_{10} radiators. RICH2 is downstream of the magnet between the last tracking station and the muon stations, it covers the high momentum range from around 15 GeV/c to over 100 GeV/c using a CF_4 radiator.

The low momentum particles are detected by RICH1 which has an acceptance covering the full LHCb acceptance. RICH2 covers a limited angular acceptance but it is able to provide a good separation between high momentum kaons and pions. For both detectors the Cherenkov light is focused by the combination of flat and spherical mirrors to reflect the image onto the Hybrid Photon Detectors (HPDs). The schematic view of RICH1 and RICH2 are shown in Fig. 3.11 and Fig. 3.12 respectively.

The HPDs within the RICH1 detector are split into two halves and are located above and below the beam line outside of the LHCb acceptance. In this region an iron shield can be utilised to protect the HPDs from the large magnetic fields

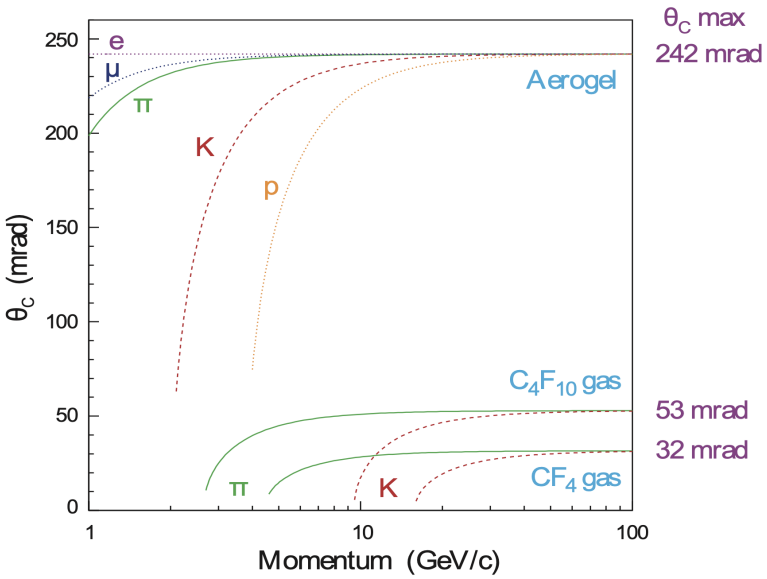

Figure 3.10 Cherenkov angle, θ_c, versus momentum for different particles. Figure from Ref. [67].

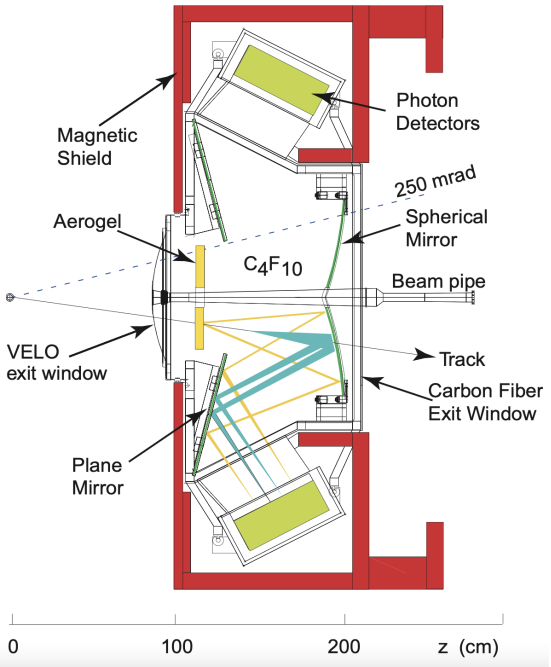

Figure 3.11 Schematic layout of RICH1 where the path of Cherenkov light is shown in blue. Figure from Ref. [67].

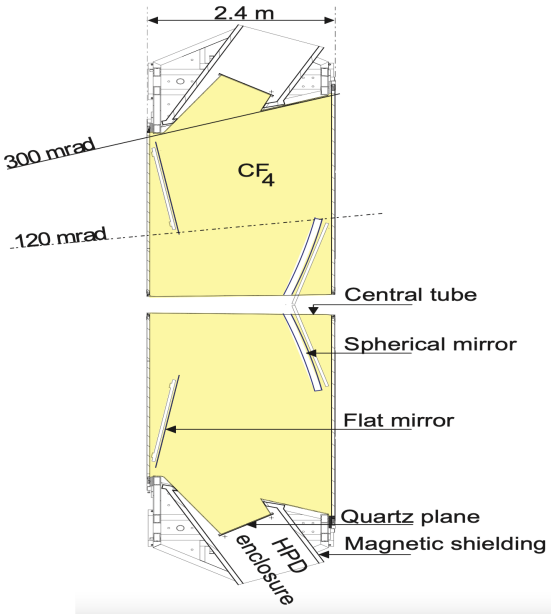

Figure 3.12 A top view schematic of the RICH2 detector. Figure from Ref.[67].

required during operation. The RICH2 detector covers an angular acceptance of 15 mrad up to 120 mrad in the horizontal plane and up to 100 mrad in the vertical plane. The limited angular acceptance is due to high momentum particles being less bent by the magnet. The RICH2 detector planes are split into two where each section is placed to the left or right of the beam line. As before, the Cherenkov radiation is reflected out of the LHCb acceptance and into the HPDs.

The HPDs are vacuum photon detectors with silicon pixels at the anode. Figure. 3.13 shows a schematic view of a HPD. A photoelectron is released from incident photons and is accelerated by an applied high voltage. When the photoelectrons hit the silicon pixels they form electron-hole pairs, with a yield of one for every 3.6 eV of deposited energy.

Note that during the second long shut down of the LHC the RICH detectors have undergone a full upgrade where the HPDs have been replaced with Multi-Anode Photomultiplier Tubes (MaPMTs) in order to successfully operate at a significantly larger luminosity. The upgrade will be described in Chapter 4.

3.4.2 Calorimeters

The calorimeter system (CALO) is used to measure the energy and positions of hadrons, electrons and photons, and to discriminate between them. It is

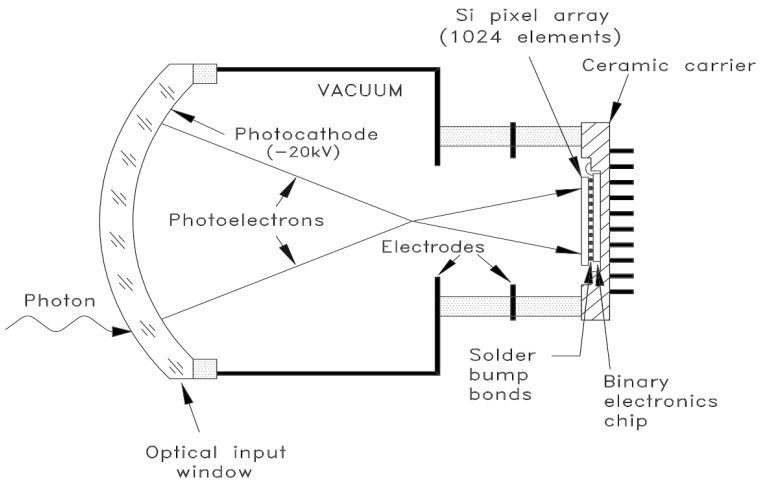

Figure 3.13 Schematic view of a HPD. Figure from Ref. [67].

made up of four sub-systems: the Scintillating Pad Detector (SPD), the Pre-Shower (PS) detector, the Electromagnetic Calorimeter (ECAL) and the Hadronic Calorimeter (HCAL). The CALO system provides valuable information on the energy of hadron, electron, and photon candidates, which is supplied to the level zero software trigger (L0). Flavour tagging and the study of B-meson decays requires an accurate reconstruction of π^0 and photon candidates, which makes the CALO system extremely important for LHCb. Showers of charged particles and photons are produced when particles interact with the material in the calorimeters. The amount of photons released in a particle shower is directly proportional to the energy of that particle.

The highest occupancy region is close to the beam pipe, smaller cells are chosen for the inner region of the detector to accommodate for this, shown in Fig. 3.14. The cell size increases with distance from the beam line. The ECAL is used for the detection of photons and electrons. It is formed of alternating layers of 2 mm thick lead and 4 mm thick scintillating tiles. The total thickness is 25 radiation lengths in order to fully absorb the photon and electron energies. The radiation length is a property of a material that is related to the energy loss of high-energy particles. The showers are converted to photons in the scintillating material which is then transmitted to PhotoMultipliers (PMT) by wavelength-shifting (WLS) fibres. The segmentation and schematic layout of the ECAL is shown in Fig. 3.14(left) and Fig. 3.15 respectively. The segmentation of the PS and SPD are the same as the ECAL. Both consist of a 15 mm lead layer between two scintillating pads. The PS helps to distinguish between electrons and pions, the SPD helps to distinguish between electrons and photons as only charged particles will induce a signal here.

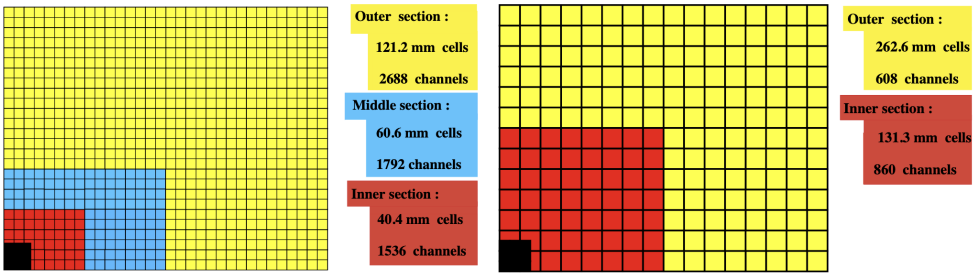

Figure 3.14 Segmentation of the ECAL (left) and the HCAL (right). Figure from Ref. [67].

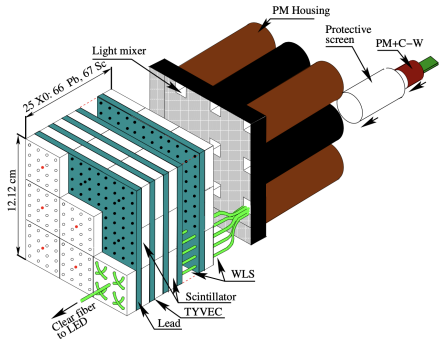

Figure 3.15 Layout of the ECAL module. Figure from Ref.[71].

The photons in the SPD and PS are collected using WLS fibres and read out using MaPMTs.

The HCAL provides measurements on the energy released by hadrons which produce showers as they traverse the detector. It consists of 1 cm thick lead plates and scintillator tiles. The total thickness is 5.6 interaction lengths. An interaction length is the average distance a hadronic particle travels before interacting with the material in the HCAL. Figure 3.14(right) shows the segmentation of the HCAL. The cells are larger than the ECAL and come in two different sizes. As with the ECAL, the photons are collected by WLS fibres and read out using PMTs. The layout of the HCAL is shown in Fig. 3.16, where the fibres and PMTs are illustrated along with the scintillators and absorbers.

3.4.3 Muon System

Many B-hadron decays involve muons in the final state, making muon identification a crucial requirement of the LHCb experiment due to measurements of CP violation and rare B decays. The mass of a Muon is around 200 times larger than the mass of an electron, and they tend to pass through the whole detector without decaying.

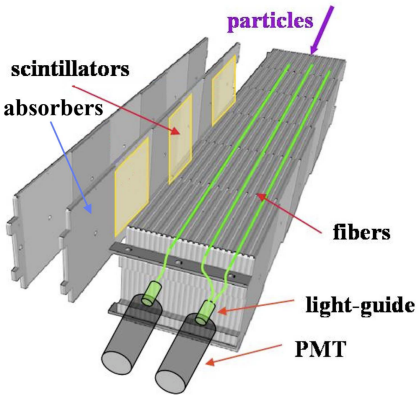

Figure 3.16 Schematic view of the HCAL module. Figure from Ref. [67].

As a consequence of their larger mass they lose less energy from Bremsstrahlung radiation compared to electrons. The muon system provides important information on the high-P_T muon trigger for the L0 and muon identification for the high-level trigger (HLT).

There are five muon stations (M1-M5) which are rectangular in shape and placed along the beam axis. The first chamber is placed after RICH2 and before the calorimeter system, the other four are placed after the calorimeters. The first station is used to improve the muon P_T measurement for the trigger. Between M2-M5 an 80 cm thick iron absorber is placed in order to stop hadrons from passing through the detector and allows the classification of muons depending on how far they reach within the chambers. To cross all five stations the muon must have a momentum of at least 6 GeV/c due to the total thickness being approximately 20 interaction lengths. Stations M1-M3 provide measurements of track direction and P_T as they have high resolution in the x-coordinate. The main purpose of stations M4 and M5 is to identify muons which travel through the whole detector, meaning that the spatial resolution can be limited.

The stations are separated into four regions, R1 to R4, depending on their distance from the beam line. This is shown in Fig. 3.17. The segmentation increases as the regions distance from the beam line increases. This allows for the channel occupancy to remain constant over the detector. The muon chambers work through muons ionising gas as they pass through the detector. The electrons are then collected on a gold-plated tungsten wire, where the drift time is measured. The system uses Multi-Wire Proportional Chambers (MWPC) filled with gas in all regions except the inner region of M1 to detect the muons. The inner most region of M1 uses Gas Electron Multipliers (GEM) detectors as they're more

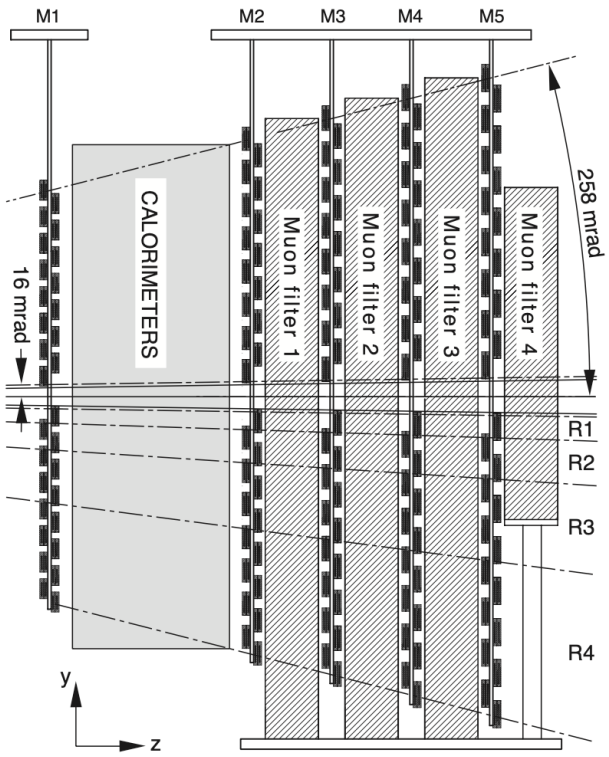

Figure 3.17 Layout of the muon system. Figure from Ref. [67].

resistant to radiation.

3.5 The LHCb Trigger

A huge amount of data is produced in pp collisions, to select the relevant processes to the LHCb experiment a trigger system is used which reduces the amount of data stored. The LHCb experiment can allow data-taking at a bunch crossing rate of 40 MHz, the trigger system reduces this to 12.5 kHz. The reduction is done in three stages; an online hardware Level-0 (L0) trigger and two offline software High-Level Triggers (HLT), this is shown in Fig. 3.18.

The L0 trigger reduces the brunch crossing rate of 40 MHz to 1 MHz where it aims to reconstruct high E_T hadrons, electrons and photons from the calorimeters and high P_T muons from the muon chambers. All of these signatures are signs of B meson decays. The events are then processed by the software trigger where fast reconstruction is performed by HLT1 to obtain the primary vertices and tracks with high P_T, this reduces the rate to 110 kHz. The HLT1 selects events through

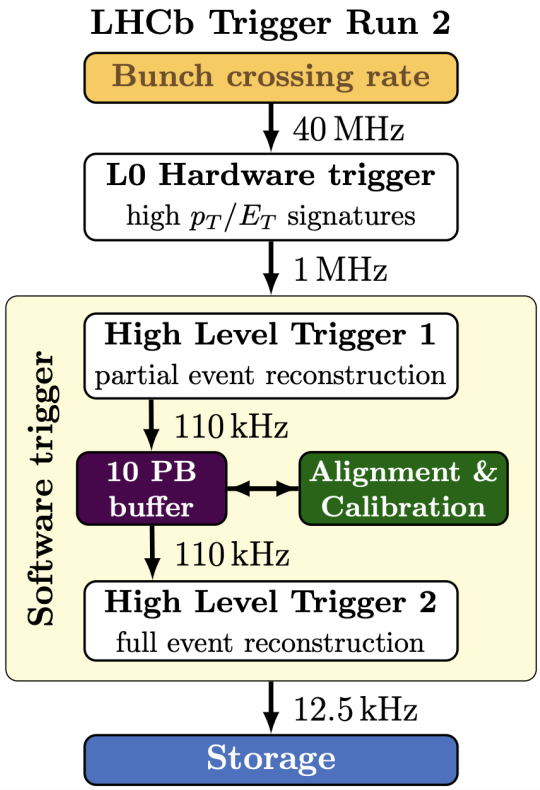

Figure 3.18 Overview of the LHCb trigger system for Run 2 [72].

one or two-track signatures. This information is then passed into HLT2 where full event reconstruction is performed by using the whole detector. This allows for a large number of exclusive and inclusive final states to trigger the event. The remaining events are written to storage for offline analysis.

Chapter 4

RICH Commissioning

After the second long shut down of CERNs accelerators in December 2018 the LHC is increasing the luminosity of the proton-proton collisions. The existing sub-detectors at the LHCb experiment could not cope with the increase, leading to the development of new and improved detectors. The Ring Imaging Cherenkov (RICH) detectors in the LHCb detector have undergone a major upgrade, where many components, including the photon detectors, have been replaced to successfully operate with the larger luminosity. This chapter will describe the work completed on the study of the signal-induced-noise of the RICH1 multi-anode photomultiplier tubes (MaPMTs) in Section 4.4. The work completed for the commissioning of the RICH2 detector, where many tests were performed to ensure full operation of the new hardware, will be explained in Section 4.5.

4.1 LHCb Detector Upgrade

Many important measurements made by the LHCb experiment are currently statistically limited. This includes measurements on CP violation, lepton flavour universality, and hadron spectroscopy. During Run 1 and Run 2 the LHCb experiment operated at a luminosity of $4 \times 10^{32}\,\mathrm{cm}^{-2}\mathrm{s}^{-1}$. To collect a significantly larger data set, the LHCb experiment must be improved such that it can operate at larger luminosities of $2 \times 10^{33}\,\mathrm{cm}^{-2}\mathrm{s}^{-1}$. This corresponds to 50 fb^{-1} of data in Run 3 and 4, compared to 9 fb^{-1} in Run 1 and 2.

The LHCb detector will be read out at the full LHC bunch crossing rate of 40

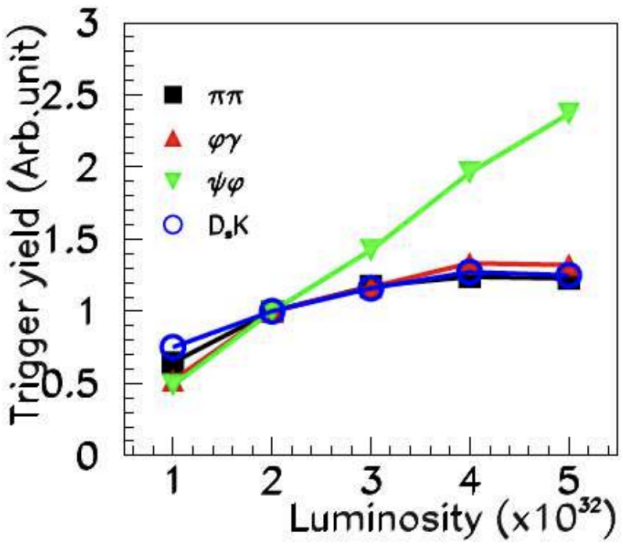

Figure 4.1 The hardware trigger efficiency as a function of luminosity for different b-hadron decays. Luminosity is in units of $\mathrm{cm}^{-2}\mathrm{s}^{-1}$. The low trigger efficiency for fully hadronic decays motivates the removal of L0. Figure from Ref. [73].

MHz. The L0 hardware trigger will be removed, which means that the whole trigger system will now be completely software. The hardware trigger has a high efficiency for dimuon decays, but it is found to remove a large fraction of fully hadronic decays, shown in Fig. 4.1. The removal of the hardware trigger will allow for a boost in efficiency as well as luminosity.

For the upgraded detector the silicon strips in the VELO will be replaced by silicon pixel sensors. The cooling system has also been improved in order to protect the silicon from radiation. The tracking system has been replaced by the upstream tracker (UT) and the scintillating fibre tracker (SciFi). The UT is composed of single sided silicon micro-strips. The SciFi tracker is composed of 2.5m long fibres read out by silicon photo-multipliers (SiPMs). The electronics in the calorimeter system have been replaced to cope with the 40 MHz bunch crossing rate and to provide a larger gain. The first muon station, M1, has been removed. The electronics for stations M2-M5 will be replaced to cope with the new trigger scheme. A schematic of the upgraded LHCb detector is shown in Fig. 4.2.

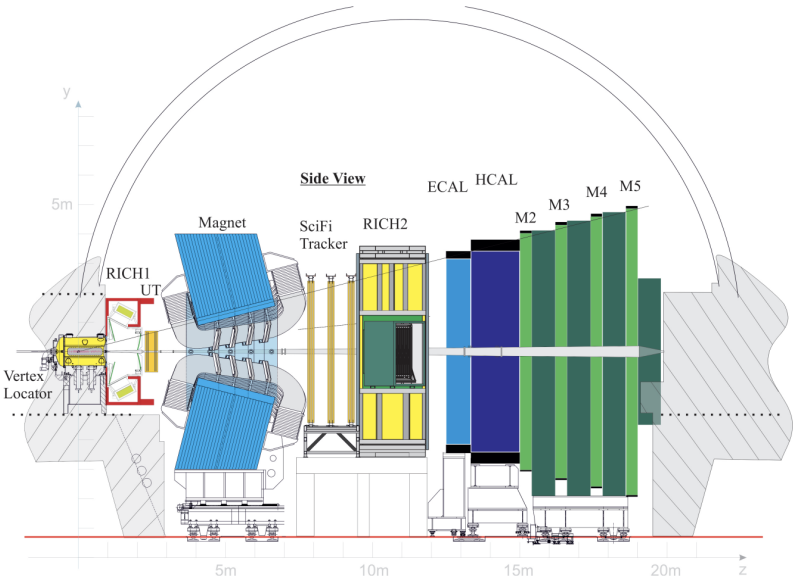

Figure 4.2 Schematic view of the upgraded LHCb detector. To be compared with Fig. 3.2. Figure from Ref. [74].

4.2 RICH Detector Upgrade

The RICH detectors are critical to the flavour-physics measurements performed at LHCb. The information on the PID allows for the discrimination between decay modes with identical topology and for a reduction in the background. The current RICH detectors, described in Section 3.4.1, use HPDs where the readout electronics work at a 1 MHz trigger rate. In order to increase the readout rate to 40 MHz the HPDs have been replaced by multi-anode photomultiplier tubes (MaPMTs) and external front-end (FE) electronics. An MaPMT works through a set of dynodes causing an avalanche of electrons. The schematic for the electrode structure in an MaPMT and the trajectory of electrons is shown in Fig. 4.3, where the incident light causes an avalanche of electrons, shown by the red lines. An avalanche is caused by an incident photon interacting with the photo-cathode, where light is producing electrons through the photo-electric effect. The electrons are then directed towards a dynode, releasing more electrons which are accelerated towards another dynode. This sequence repeats with the number of electrons increasing exponentially. The typical voltage difference between dynodes is around 100 V and the MaPMT can provide a gain larger than 10^6 [75]. The cascade of electrons is then detected by the anode.

The FE electronics provides the shaping, amplification, discrimination, and

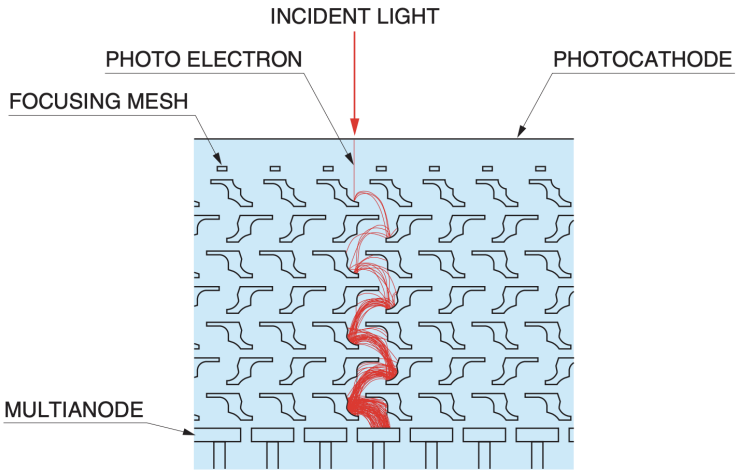

Figure 4.3 Schematic of the electrode structure and the trajectory of electrons. The incident light is indicated by the red arrow, which causes an avalanche of electrons shown by the red lines. Figure from Ref. [76].

digitisation of the MaPMT signals. The MaPMTs are chosen due to the necessity of a position-sensitive photon detector, required to achieve the needed Cherenkov angle resolution. The signal from the MaPMT anodes are read out by an application-specific integrated circuit (ASIC) named CLARO, which is radiation hard and has a low power consumption. In the RICH1 and central regions of the RICH2 detectors the elementary cell (EC) is a unit which is comprised of four 1x1 inch MaPMTs and the FE electronics. On the outside regions of RICH2 an EC is formed from one 2x2 inch MaPMT. These are then connected to a digital board, called the Photon Detector Module Digital Board (PDMDB), which formats the binary output from the CLARO. A Photon Detector Module (PDM) is formed from four ECs and two PDMDBs. A schematic view of an EC is shown in Fig. 4.4.

The RICH detectors are formed of columns of elementary cells, where each column contains 24 ECs, equating to 6 PDMs per column. There are 22 columns in RICH1 and 24 columns in RICH2. Over 1000 EC units are needed to equip RICH1 and RICH2. The elementary cells will need to be subject to a strict testing protocol to ensure their full operation once placed in the LHCb detector. A description of this procedure will be described in the following section. The RICH1 detector has a larger occupancy compared to the RICH2 detector because it is closer to the proton-proton collision point and is placed before the magnet. The occupancy of the RICH1 detector is shown in Fig. 4.5, where the different coloured areas correspond to different levels of occupancy.

Two properties that can define the quality of an MaPMT are its signal-induced

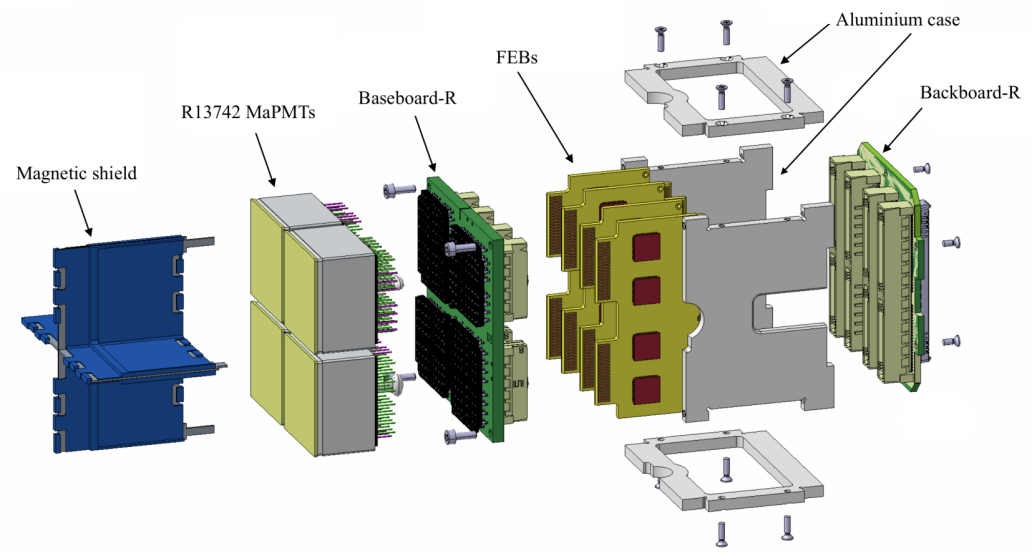

Figure 4.4 Schematic of an elementary cell. The magnetic shield protects the MaPMTs in RICH1 from the residual magnetic field in this region. Figure from Ref. [75].

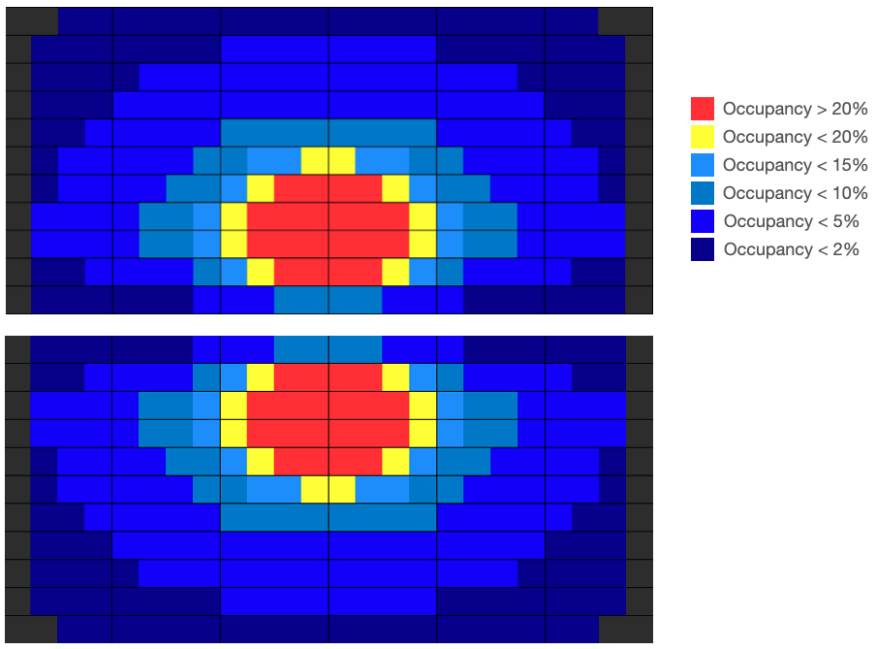

Figure 4.5 A rough indication of occupancy for the RICH1 detector. The different levels are indicated by the legend.

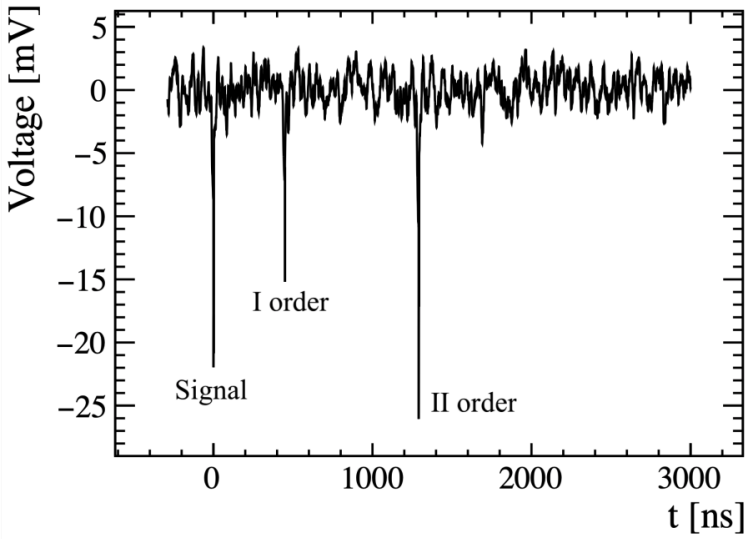

Figure 4.6 An example of signal induced noise. At t=0 ns the MaPMT sees a laser, corresponding to this signal peak. The two pulses at a later time are due to SIN. Figure from Ref. [75].

noise (SIN) and the spread of the gain, where the analysis of these qualities will be presented in the next section. Other important properties include the dark count rate and homogeneity of pixel gains.

4.3 Signal Induced Noise

Signal induced noise is primarily caused by the signal ionising gas in the MaPMT, where the ions travel towards the photo-cathode and cause an avalanche of electrons. An example of a SIN pulse is shown in Fig. 4.6. An example of how the SIN affects the response from a pixel in an MaPMT is shown in Fig. 4.7. The signal region (S) is shown by the teal box, and the background region (B) is indicated by the purple box. The expected number of SIN pulses induced by a single electron response signal is given by:

$$\mu_{\mathrm{SIN}} = \mathrm{B/S}, \tag{4.1}$$

where B is the background and S is the signal. A low μ_{SIN}, where $\mathrm{S} \geq \mathrm{B}$, is desirable for our MaPMTs, especially in the high occupancy regions of the detector. More information can be found in Ref. [75].

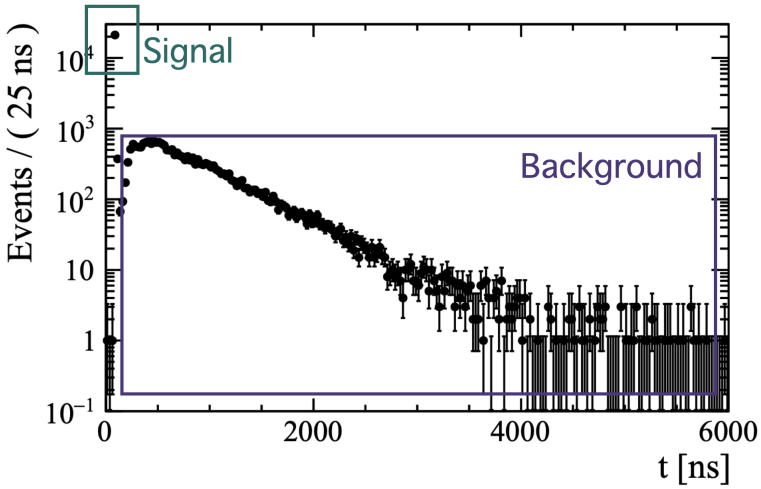

Figure 4.7 Time distribution for selected events using a logarithmic scale for a pixel affected by SIN. The teal box represents the signal (S) and the purple box represents the background (B). Figure from Ref. [75].

4.4 Signal Induced Noise for RICH1

The RICH1 detector has an extremely high-occupancy in its central regions, leading to the necessity of grouping the MaPMTs into elementary cells based on the spread of the gain and SIN. It is then possible to determine their optimal positions within the detector by placing the highest quality MaPMTs in the high occupancy regions. The gain is the ability of the MaPMT to amplify the signal seen from the incident photon. Each pixel within an MaPMT has a gain associated to it and the spread of the gain across the entire MaPMT is an important factor when trying to determine the quality of the MaPMT.

An EC is formed of four 1x1 inch MaPMTs in the RICH1 detector. The layout of an EC is shown in Fig. 4.8, where each MaPMT is comprised of 8x8 (64) pixels. The highest values of μ_{SIN} are found in pixels 0-7 and 56-63, which is indicated in red in Fig. 4.8. The distribution of the SIN and gain of each MaPMT can be analysed in order to group similar MaPMTs together and determine how well they perform. The best performing MaPMTs are required to have an average μ_{SIN} of less than 1 and a spread of the gain across the MaPMT of less than 2, these would ideally be placed in the central regions of the detector. The MaPMTs with an average μ_{SIN} of less than 1 and a spread of the gain of less than 2.5 can be placed just outside of the high-occupancy regions, and the rest will be placed in the outside regions of the detector.

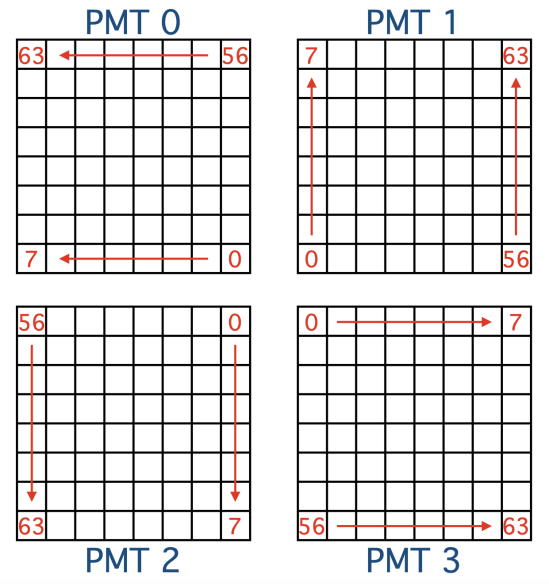

Figure 4.8 Layout of an elementary cell in RICH1, with the labelling convention of the top left MaPMT as 0, the top right as 1, the bottom left as 2 and the bottom right is 3. The highest values of SIN are found in pixels 0-7 and 56-63, labelled in red.

To start off, the strategy is as follows:

1. Find the MaPMTs with an average μ_{SIN} across pixels 0-7 and 56-63 of less than 1.

2. The spread of the gain across the MaPMT must be less than 2.

The elementary cells which have four MaPMTs which satisfy these conditions are not modified. The ECs with three MaPMTs which satisfy the first condition can be matched based on gain with one MaPMT with an averaged $\mu_{\text{SIN}} < 1$. The same procedure can be used for ECs with two MaPMTs satisfying the first condition. An example of a perfect elementary cell is shown in Fig. 4.9, and an example of an EC with three MaPMTs with an average $\mu_{\text{SIN}} < 1$ is shown in Fig. 4.10. The vertical red line indicates where $\mu_{\text{SIN}} = 1$, where μ_{SIN} is expressed as B/S @ 1000 V. The bottom right MaPMT in Fig. 4.10 has an average $\mu_{\text{SIN}} > 1$. This MaPMT can be swapped for one with an average $\mu_{\text{SIN}} < 1$ and a similar spread of the gain to the other MaPMTs within the elementary cell. This procedure produces a perfect elementary cell, defined by the conditions set out previously. The same process has been applied for all MaPMTs in order to maximise the number of highest performing cells to place in the high occupancy regions of the detector. At a slightly lower occupancy will be the ECs with an average $\mu_{\text{SIN}} < 1$

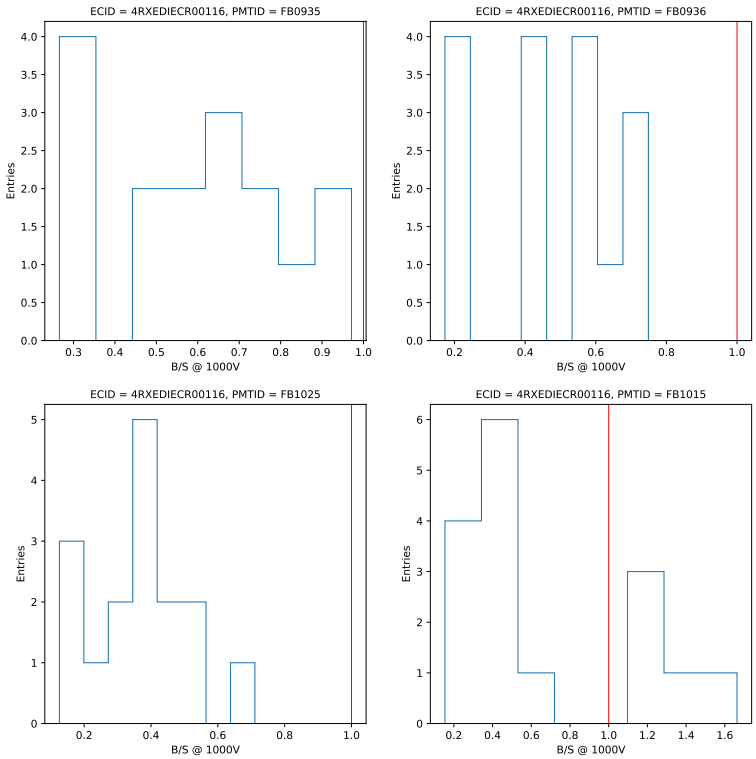

Figure 4.9 Example of a 'perfect' elementary cell, where the average μ_{SIN} across each MaPMT for this EC is less than one and the spread of the gain across the MaPMTs is less than 2. Each subplot is a different MaPMT within the elementary cell. The red vertical line indicates a μ_{SIN} of 1. The μ_{SIN} is given as B/S @ 1000V.

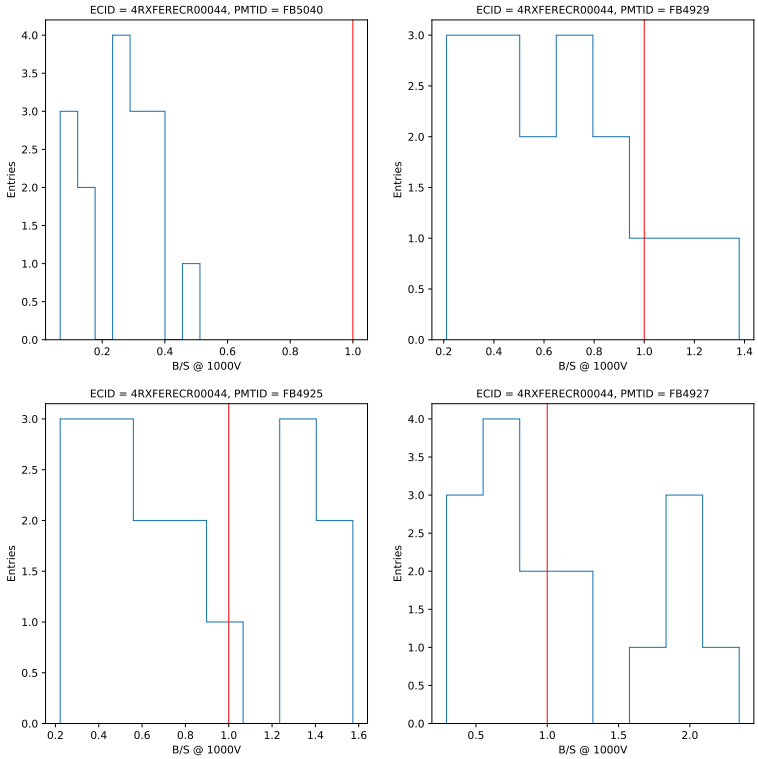

Figure 4.10 Example of an elementary cell containing three MaPMTs with an average $\mu_{\mathrm{SIN}} < 1$ and a spread of the gain of less than 2. The bottom right MaPMT has an average $\mu_{\mathrm{SIN}} > 1$.The vertical red line indicates a μ_{SIN} of 1.

and a spread of the gain < 2.5. Overall, this method produced 77 cells with four MaPMTs with an average $\mu_{\text{SIN}} < 1$ and spread of the gain < 2, and 32 cells with four MaPMTs with an average $\mu_{\text{SIN}} < 1$ and spread of the gain < 2.5. This process produced enough perfect cells to cover the high occupancy regions of the detector and allowed for the definition of the installation scheme.

The MaPMTs have been divided into groups of quality and gain, which is an important ingredient for the re-shuffling campaign of the photon detectors in the ECs. The RICH1 detector has now undergone the full commissioning procedure and the installation into the LHCb cavern completed in March 2022.

4.5 Laboratory work for RICH2

Each column in the RICH2 detector is made up of 24 elementary cells and there are 12 columns on each side of the detector, A-side and C-side. The A-side of RICH2 is shown in Fig. 4.11. The column commissioning starts with the assembly, by installing the MaPMTs, PDMDBs, and their cables. After thorough checks of all cables to ensure they are connected properly, it is installed into a dark box for functionality tests. The dark box, called the small simple box (SSB), contains light which can fire test pulses at the columns and it is closed off from all other sources of light. The columns have a high and low voltage input. First, the cooling pipes are connected and checked through the temperature sensors. The next stage is two startup checks, the first being the low voltage. The low voltage is switched on and if everything is working it should be at a voltage of around 8V and a current of around 6A. Occasionally, this is not the case, and this could indicate a short in one of the PDMDBs. All the fibre optic links that are attached to the ECs should then lock, an issue with locking is usually fixed by cleaning the fibres. The links can then be checked one-by-one for each PDMDB to ensure full operation. Once all these steps have been complete the PDMDBs can be configured. The second check is a set of functional tests, starting with a short run without the test pulse to check in the hit map of the MaPMTs that all channels are off. The next test is to check in the hit map that all channels are on, without any signal present. Next, a short run is taken with a test pulse to check in the hit map that the channels are on. Lastly, a short run is taken with the high-voltage on to ensure that all the channels in the MaPMTs are counting.

The next step is to run a sequence of tests on the columns which have been

Figure 4.11 Photograph of RICH2 A-side columns ready to be installed into the LHCb detector. The 2x2 inch MaPMTs are on the outside regions and the 1x1 inch are on the central regions of the detector.

automated using a standard software tool in LHCb. The sequence of tests is:

1. PDMDBs configuration
2. Functional tests and time alignment
3. DAC scans
4. Threshold scans for working points
5. Test of working points
6. HV training
7. First dark count run
8. Threshold scan
9. Second dark count run
10. SIN measurements.

The PDMDB configuration and functional tests are the same as the startup checks and are added to ensure the PDMDBs and MaPMTs are operating as expected.

DAC Scans

The digital to analogue converter (DAC) scans are used to fully calibrate the CLARO. The CLARO has a binary output which is formatted by the PDMDB. In the DAC scans a known amount of charge is injected from the PDMDBs into each CLARO channel. This is done in 256 steps, corresponding to a charge of $15.6 \times 10^3 e$ and 1000 pulses into each CLARO channel per step. A value of attenuation, offset, and threshold is chosen for each scan. A channel will be off until the amount of charge is above the threshold. Repeating the scans with three different threshold settings provides a conversion from threshold to charge. The DAC scans allow us to determine whether there is a high level of noise in the system, if a CLARO has an awkwardly high threshold setting, and allows for the investigation of the charge calibration for the different channels.

Threshold scans for working points and test

This step allows for the determination of the working points by scanning over a threshold range. The working points are determined at a voltage of 1000V. The threshold is how many channels in the MaPMTs that need to be triggered to read out the data. For the threshold scans the source is the light from a laser. A value of attenuation and offset are chosen and the threshold is scanned from 63 to 0, corresponding to the number of pixels in an MaPMT. This process produces the single photon spectrum, allowing for the determination of the average gain for each pixel in terms of threshold.

HV Training

The high voltage is steadily increased from 0 V to 1050 V for a period of 8 hours. The DAC scans run in the background during this process.

Dark Count Rate

The dark count rate (DCR) is the averaged number of counts the MaPMTs detect in the absence of light. It is caused by a spontaneous emission of a photon from gas in the detector, and is highly suppressed when the detector is cooled due to its predominantly thermal origin. Before installing the column into the SSB the MaPMTs can be exposed to some light. To account for this the column is kept in the dark overnight at a voltage of 1050 V before the DCR tests are performed. The voltage is then decreased to 1000 V and after 15 minutes a run without light is acquired to determine the DCR. The DCR limits set by the manufacturing company define whether an MaPMT passes this test.

Threshold Scans for MaPMT Gain Measurement

The gain of the MaPMTs can be measured by acquiring threshold scans at different high voltage and attenuation values. The threshold scans are obtained through the same procedure described previously. A dedicated fit procedure is applied to determine the value of the gain in terms of the CLARO threshold. This information is then combined with the calibration found from the DAC scans to obtain the average gain.

Signal Induced Noise

The full SIN spectrum is already characterised for each MaPMT. This step is to characterise the SIN in the SSB setup. The SIN is studied at three time slots; one centered around the signal from the test pulse, the second with a 300 ns delay, and the last with a 1 μs delay. This is repeated for 6 values of the high voltage.

In total the sequence of tests should take around 1 day, assuming that no errors arise. However, during commissioning there are many places where a test could fail, meaning that the tests often took longer. The tests that failed were investigated and run again until the column passed. Occasionally MaPMTs had to be replaced for the column to pass commissioning. After running the commissioning procedure on all 24 columns of the RICH2 detector it was installed into the LHCb cavern in February 2021. The commissioning of the RICH2 detector was incredibly useful for insuring full operation once placed into the LHCb cavern. It has saved a significant amount of time from reducing the number of components that needed replacing once testing commenced in the LHCb cavern. The investigation into the signal induced noise and gain of the MaPMTs for the RICH1 detector allowed for the definition of the installation scheme. It has enabled us to place the highest quality MaPMTs into the high occupancy regions of the detector, which will improve the RICH detector performance in the following years.

Chapter 5

Measurement of Ω_b^- decays

This chapter will describe how the Ω_b^- candidates are selected and modelled in $\Omega_b^- \to \Xi_c^+ K^- \pi^-$ decays. The aim is to observe the excited Ω_c^0 resonances in the $\Xi_c^+ K^-$ mass spectrum, where the Ξ_c^+ decays into a proton, a K^- meson and a π^+ meson. This will be the first study of this decay mode and non-prompt production of the Ω_c^0 using LHCb data. The excited Ω_c^0 states have been observed in the prompt production of the Ω_c^0 baryons, where a promptly produced particle is one that is produced at the pp collision point. Chapter 6 will detail how the $\Xi_c^+ K^-$ candidates are selected for the search of the excited Ω_c^0 states, how the invariant mass distribution is modelled, and the investigation of their quantum numbers. The main analysis strategy is set out in the following section and the details of the simulated data sets are described in Sec. 5.2.1. The ratio of relative branching fractions of the $\Omega_b^- \to \Xi_c^+ K^- \pi^-$ decay with respect to the $\Omega_b^- \to \Omega_c^0 \pi^-$ decay is evaluated and described in Sec. 5.10, and a precise measurement of the Ω_b^- mass is also performed, presented in Sec. 5.11.

5.1 Analysis strategy

The aim of this analysis is to search for the excited Ω_c^0 states in the $\Xi_c^+ K^-$ mass spectrum where the $\Omega_b^- \to \Xi_c^+ K^- \pi^-$ decay is used and the Ξ_c^+ is reconstructed using the $pK^-\pi^+$ final state. The decay of $\Omega_b^- \to \Omega_c^0 \pi^-$ where $\Omega_c^0 \to pK^-K^-\pi^+$ is studied as a control mode due to the similar topologies of the final state. In both cases the Ω_b^- baryon is created at the pp collision point, called the primary vertex

(PV), and subsequently decays at the secondary vertex (SV). The non-prompt production of the Ω_c^0 states will provide a significant reduction in background compared to the prompt case. The selection strategy is used in order to reduce background and separate out the signal candidates.

5.2 Data Sets

This analysis makes use of the 2011-2012 (Run 1) and 2015-2018 (Run 2) datasets which were collected at the LHCb detector in pp collisions at $\sqrt{s} = 7,\ 8$ and 13 TeV. The Run 1 and Run 2 data sets correspond to an integrated luminosity of 3 fb^{-1} and 6 fb^{-1} respectively, combining to a total sample of 9 fb^{-1}.

5.2.1 Simulated data sets

For analyses at the LHCb experiment simulated samples are required to model the different decays that are studied. For this analysis simulation is required to model the signal input for our multivariate algorithm, model shapes of mass distributions, and calculate efficiencies. The pp collisions are generated using Pythia [77] in the simulation, using a specific LHCb configuration [78]. The Pythia package is a general purpose generator. The decays of particles are simulated using EvtGen [79]. The Geant4 toolkit [80] is used to model the interactions of the particles with the detector. In this analysis the simulation is generated over the entire phase space.

The simulated samples are listed in Table 5.1 including their sample size and event type. For the analysis of Run 1 data the samples are simulated using the detector conditions at LHCb in 2012, and for Run 2 they are simulated from 2016. It is assumed that the detector conditions do not change significantly between 2011-2012 and 2015-2018. There are samples for both $\Omega_b^- \to \Xi_c^+ K^- \pi^-$ and $\Omega_b^- \to \Omega_c^0 \pi^-$, as well as a second sample of $\Omega_b^- \to \Xi_c^+ K^- \pi^-$ decays with an additional requirement on the mass of the $\Xi_c^+ K^-$, used for investigating the properties of the excited Ω_c^0 states. The samples proceed through the following

Table 5.1 Simulated data used in this analysis.

Event Type	Description	Sample Size
16165037	$\Omega_b^- \to \Xi_c^+ K^- \pi^-$	3.5M (2012 & 2016)
16165038	$\Omega_b^- \to \Omega_c^0 \pi^-$	4M (2012 & 2016)
16165131	$\Omega_b^- \to \Xi_c^+ K^- \pi^-$ $(m(\Xi_c^+ K^-) < 3300\,\text{MeV})$	20M (2012 & 2016)

decay chains:

$$\begin{aligned} \Omega_b^- &\to \Xi_c^+ (\to p K^- \pi^+) K^- \pi^-, \\ \Omega_b^- &\to \Omega_c^0 (\to p K^- K^- \pi^+) \pi^-. \end{aligned} \tag{5.1}$$

Both decays proceed through phase space, meaning that there are no intermediate resonances in the simulated samples. Smearing on the momentum to correct the mass resolution has been applied to all Run 1 simulation. In the generation the lifetime of the Ω_c^0 has been set to $\tau = 250\,\text{fs}$ according to a recent LHCb measurement [81]. It is known that the simulated samples for LHCb do not accurately describe the particle identification variables. A weighting based on PID calibration data is applied to the PID variables in order to account for this. The corrections are generated through the momentum, pseudorapidity and the event multiplicity. Truth matching is applied to all simulated samples, ensuring that all the reconstructed tracks are linked to the correct particle hypothesis.

For all samples with a Ξ_c^+ in the decay process, the Ξ_c^+ Dalitz plot has been weighted in simulation according to the observed distribution. This is to try to increase the efficiency of the multivariate analysis technique which is implemented to reduce background. A higher efficiency allows for a better separation between signal and background. In order to weight the simulated Dalitz plot, 2012 data is used [82] for both 2012 and 2016 simulation samples. The Dalitz plots which are produced in this analysis have $\text{M}^2(K^- p)$ on the x-axis and $\text{M}^2(K^- \pi^+)$ on the y-axis. These variables are found from the square of the $K^- \pi^+$ and $K^- p$ four-momentum. Figure 5.1 shows the resultant Dalitz plots for each stage of the process. Figure 5.1c shows the Dalitz plot of the Ξ_c^+ from 2012 data, which was recently published [82], where it is possible to see the K^* resonance decaying to $K^- \pi^+$ (horizontal band at around 0.8 GeV^2), two Λ resonances which decay to $K^- p$ (two vertical bands in the top left of the Dalitz plot) and one Δ resonance which corresponds to the diagonal band across the top right of the distribution. Figure 5.1f shows the Ξ_c^+ Dalitz plot in the simulated signal sample, as expected

all the events are distributed evenly throughout phase space. Figure 5.1i shows the Ξ_c^+ Dalitz plot in simulation after it has been weighted using 2012 data where the resonances described previously can now be seen. In order to weight the simulated Dalitz plot the weight of each bin in the data Ξ_c^+ Dalitz plot (Fig. 5.1c) is applied to each bin in the simulated Ξ_c^+ Dalitz plot (Fig. 5.1f) and then it is normalized. This provides us with a weighted Dalitz plot shown in Fig. 5.1i.

5.3 Selection Strategy

Huge amounts of data are collected by LHCb in every data taking year. To be able to process the data files a large number of selections must be applied to reduce their size. By exploiting the physics we know about the topological and kinematic characteristics of our decay modes it is possible to remove a large number of background events while keeping the majority of our signal candidates. Selection of the Ω_b^- candidates happens in three stages:

- Stripping and trigger selection requirements.
- Offline selections.
- Multivariate analysis to select Ω_b^- candidates.

These are applied to both $\Omega_b^- \to \Xi_c^+ K^- \pi^-$ and $\Omega_b^- \to \Omega_c^0 \pi^-$ decays as well as their wrong sign (WS) partners. The WS candidates are $\Omega_b^- \to \Xi_c^+ K^- \pi^+$ and $\Omega_b^- \to \Omega_c^0 \pi^+$, which are expected to contain no structures due to the violation of charge conservation.

5.4 Stripping and trigger selection

This analysis uses the full 3 fb^{-1} data set collected during the 2011-2012 data taking period and the full 6 fb^{-1} taken during 2015-2018. All candidates are required to pass a stripping line in order to reduce the size of the event before storing it. The stripping line used for the $\Omega_b^- \to \Xi_c^+ K^- \pi^-$ decay selects Ω_b^- candidates which decay into a Ξ_c^+ baryon, a K^- and a π^- meson, where the Ξ_c^+ baryon decays into a proton, a K^- and a π^+ meson. Similarly for the $\Omega_b^- \to \Omega_c^0 \pi^-$ decay, where the Ω_c^0 baryon decays into a proton, two K^- mesons and a π^+ meson.

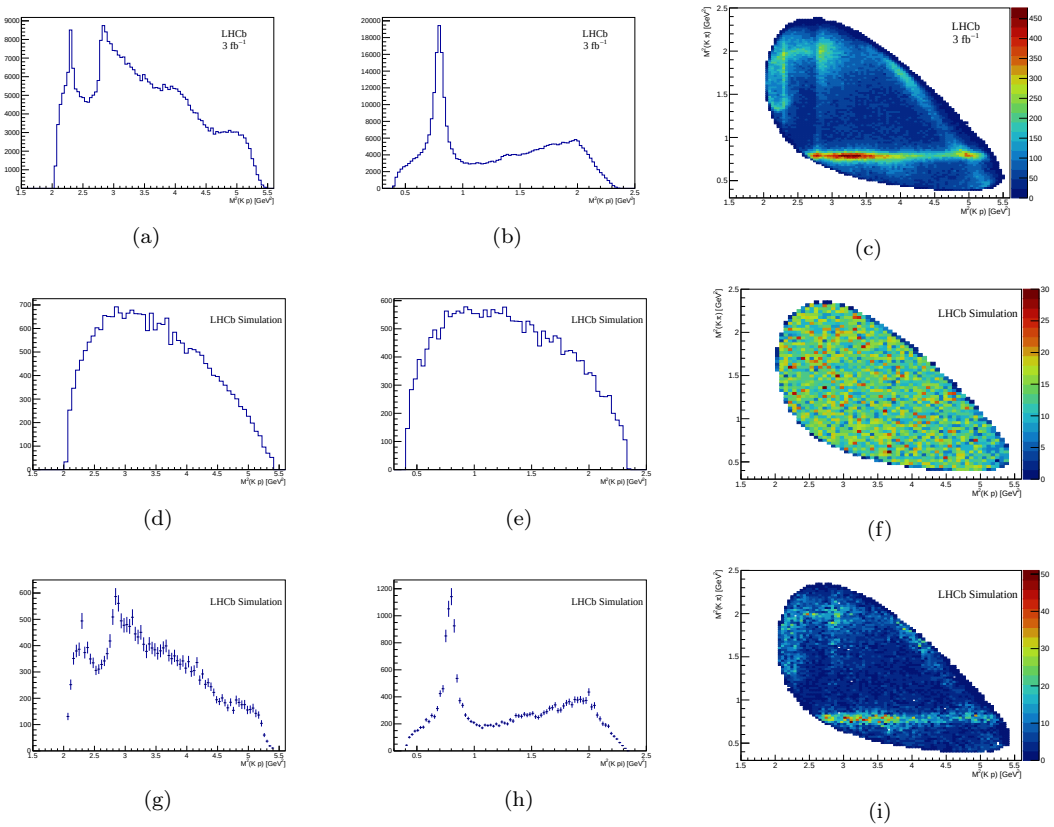

(a) (b) (c)

(d) (e) (f)

(g) (h) (i)

Figure 5.1 The first, second, and the third columns show the K^-p projections, the $K^-\pi^+$ projections, and the Dalitz plot for different samples respectively. Figures (a), (b) and (c) correspond to the Ξ_c^+ decay in the 2012 data. Figures (d), (e) and (f) show the phase space simulation (2012) for the Ξ_c^+ decay sample where all events are distributed evenly throughout phase space. Figures (g), (h) and (i) show the distributions for the re-weighted simulated sample which is used for the multivariate analysis.

This analysis makes use of two stripping lines:

- `StrippingOmegab2XicKpiLine`, and
- `StrippingOmegab2Omegac0Pi0megac02PKKPiBeauty2CharmLine`,

for $\Omega_b^- \to \Xi_c^+ K^- \pi^-$ and $\Omega_b^- \to \Omega_c^0 \pi^-$, respectively. The selection criteria implemented in the stripping lines are summarised in Tables 5.2 and 5.3 for the $\Omega_b^- \to \Xi_c^+ K^- \pi^-$ and $\Omega_b^- \to \Omega_c^0 \pi^-$ decays respectively. The stripping lines had been produced by other members of the LHCb collaboration. They are formed of loose selection requirements based off of topological and kinematic constraints, and information from previous or similar analyses.

Table 5.2 Selection criteria implemented in the stripping line for $\Omega_b^- \to \Xi_c^+ K^- \pi^-$. Where $m_{PDG}(\Xi_c^+)$ is the world average for the mass of the Ξ_c^+ from the PDG [6].

Candidate	Variable	Requirement
Daughters of Ξ_c^+	Pion ProbNNpi	> 0.1
	Kaon ProbNNk	> 0.1
	Proton ProbNNp	> 0.1
Ξ_c^+	Invariant mass	$m_{PDG}(\Xi_c^+) - m(pK^-\pi^+) < 100$ MeV
	Vertex quality	$\chi^2/ndf < 10$
	χ^2 distance from related PV	> 36
	Cosine of the direction angle	> 0
Bachelor K^-	Pion ProbNNpi	> 0.1
Bachelor π^-	Kaon ProbNNk	> 0.1
Ω_b^-	Momentum	> 3500 MeV
	Invariant mass	$[5500, 6700]$ MeV
	χ^2_{IP} from PV	< 25
	Cosine of the direction angle	> 0.999
	Vertex quality	$\chi^2/ndf < 10$
	Decay time	< 0.2 ps

All Ω_b^- candidates are required to originate from the PV by requiring a small χ^2_{IP}, where χ^2_{IP} is defined as the difference in the vertex-fit χ^2 of a given PV reconstructed with and without the candidate under consideration. The variable ProbNNX is the probability that the particle is identified as X, where X = pi, K, p. The vertex quality, χ^2/ndf, is the χ^2 per degree of freedom of the track fit. The direction angle is the angle between the momentum of the particle and the direction vector from its production vertex to its end-vertex. The PID is the identification of the particle. The track quality calls for tracks which have a small χ^2.

Table 5.3 Selection criteria implemented in the stripping line for the $\Omega_b^- \to \Omega_c^0 \pi^-$ decay. Where $m_{PDG}(\Omega_c^0)$ is the world average Ω_c^0 mass from the PDG [6].

Candidate	Variable	Requirement
Daughters of Ω_c^0	Track quality	$\chi^2_{TR}/ndf < 3.0$ (Run 1) or 4 (Run 2)
	Transverse momentum	> 100 MeV
	Momentum	> 1000 MeV
	χ^2_{IP}	> 4
	Kaon PID	$PID_K > -10$ (Run 2)
	Proton PID	$PID_p > -10$ (Run 2)
	Pion PID	$PID_K < 20$ (Run 2)
	p OR K^- OR π^+ Track quality	$\chi^2_{TR}/ndf < 2.5$ (Run 1)
	p OR K^- OR π^+ Transverse momentum	> 500 MeV
	p OR K^- OR π^+ Momentum	> 5000 MeV
Ω_c^0	Invariant mass	$m_{PDG}(\Omega_c^0) - m(pK^-K^-\pi^+) < 100$ MeV
	Vertex quality	$\chi^2/ndf < 10$
	χ^2 distance from related PV	> 36
	Cosine of the direction angle	> 0
Bachelor pion	Track quality	$\chi^2_{TR}/ndf < 3.0$ (Run 1) or 4 (Run 2)
	Transverse momentum	> 500 MeV
	Momentum	> 5000 MeV
	χ^2_{IP}	> 4
	Pion PID	$PID_K < 20$ (Run 2)
Daughters of Ω_b^-	Ω_c^0 OR π^- Transverse momentum	> 1700 MeV
	Ω_c^0 OR π^- Momentum	> 10000 MeV
	Ω_c^0 OR π^- Track quality	$\chi^2_{TR}/ndf < 2.5$ (Run 1) or 4 (Run 2)
	Ω_c^0 OR π^- χ^2_{IP}	> 16
Ω_b^-	Vertex quality	$\chi^2/ndf < 10$
	Decay time	$\tau > 0.2$ ps
	χ^2_{IP} from PV	< 25
	Cosine of the direction angle	> 0.999

Trigger selection

The stripping line of the $\Omega_b^- \to \Omega_c^0 \pi^-$ decay has selection requirements on the trigger which the stripping line for the $\Omega_b^- \to \Xi_c^+ K^- \pi^-$ process does not contain. The candidates must be triggered on signal (TOS) for any HLT2 Topological trigger at the HLT2. Trigger requirements are also needed at L0 and HLT1 in order to determine efficiencies. All trigger selection criteria are summarised in Table 5.4 and the requirements are applied to both $\Omega_b^- \to \Xi_c^+ K^- \pi^-$ and $\Omega_b^- \to \Omega_c^0 \pi^-$ decay modes.

Table 5.4 Set of trigger requirements applied to each decay mode.

Run	L0	HLT1	HLT2
1	Global_TOS OR TIS	TrackAllL0_TOS	Topo[2|3|4]BodyBBDT_TOS
2	Global_TOS OR TIS	TrackMVA_TOS OR TwoTrackMVA_TOS	Topo[2|3|4]Body_TOS

5.5 Offline Selection

The Ω_b^- candidates have been refitted using a kinematic fit to improve mass resolution, constraining the Ω_b^- candidates to originate from its associated PV, defined as the PV to which the impact parameter of the combination of two-track and Ξ_c^+/Ω_c^0 candidates is the smallest, and constraining the mass of the Ω_c^0 and Ξ_c^+ to their known values [6]. Several criteria have been made while processing the data in order to reduce their size. These selections are summarised in Table 5.5, where the variables are the same as described previously. The momenta of the tracks are scaled using a momentum scale calibration tool [83] in order to improve the mass resolution and accuracy.

Mitigating the differences of stripping selections

Currently, the selections made to each decay mode at the stripping line differ. The branching fraction calculation requires each process to possess the same selections in order to ensure the cancellation of some systematic uncertainties. A set of requirements have been applied to each decay mode in order to mitigate the difference in selections made at the stripping line. These are summarised in Table 5.6. Where the $\chi^2_{\rm FD}$ is a requirement on the quality of the flight distance to

Table 5.5 Selection requirements applied to both decay modes after the stripping selection.

Candidate	Variable	Requirement
$\pi^{\pm}$	ProbNNpi	> 0.1
	Pion PID	$PID_K < 20$
K^-	ProbNNp	> 0.1
	Proton PID	$PID_p > -10$
p	ProbNNk	> 0.1
	Kaon PID	$PID_K > -10$
	Transverse momentum	> 250 MeV
	χ^2_{IP}	> 4

the primary vertex of the decay and the other variables are the same as described previously.

Table 5.6 Selection requirements applied after production in order to mitigate the different selections enforced at the stripping line.

Candidate	Variable	Requirement
p OR K^- OR $\pi^{\pm}$	χ^2_{IP}	> 16
	Transverse momentum	> 1700 MeV
	Momentum	> 10000 MeV
	Track quality	$\chi^2_{TR}/ndf < 2.5$ (Run 1) 4 (Run 2)
K^-	ProbNNk	> 0.2
Bachelor pion	Transverse momentum	> 500 MeV
	Momentum	> 5000 MeV
Ω_b^-	χ^2_{DTF}/ndf	$0 < \chi^2/ndf < 5$
	χ^2_{IP}	< 16
	Cosine of the direction angle	> 0.99994
	Transverse momentum	> 3500 MeV
	χ^2_{FD}	> 64

Many of the selection requirements which are applied at this stage have been taken from the previous analysis of the $\Omega_b^- \to \Omega_c^0 \pi^-$ decay [65], including χ^2_{IP}, χ^2_{FD}, and ProbNNk. Loose requirements are applied to the ProbNN variables of each final state particle in order to reduce background.

5.6 Selection of $\Omega_b^- \to \Xi_c^+ K^- \pi^-$ candidates

The Ξ_c^+ candidates are created by the combination of three tracks which are detached from the primary pp interaction vertex in each event. Next, the Ω_b^- candidates are formed by combining the selected Ξ_c^+ candidate with a kaon and

a pion. The selection requirements applied to this decay mode are described in Sec. 5.3. The requirement on the Ω_b^- decay time (given in Table 5.2) makes the overlap with the prompt sample, analysed in Ref. [5], negligible. An additional selection is imposed on the mass of the Ξ_c^+ baryon: $2458 < m(pK^-\pi^+) < 2478$ MeV, which corresponds to $\pm 2\sigma$ of the expected Ξ_c^+ mass ($m(\Xi_c^+) = 2467.94$ MeV). This requirement is validated through the simulation samples.

Resolution of Ξ_c^+

The simulated samples can be used to cross check the selection requirements made on the Ξ_c^+ mass by measuring its resolution. All offline selection requirements are applied to the $\Omega_b^- \to \Xi_c^+ K^- \pi^-$ simulated samples, omitting the Ξ_c^+ mass requirement. An unbinned maximum likelihood fit is then used to model the $\delta M_{\Xi_c^+}$ mass distribution, where:

$$\delta M_{\Xi_c^+} = m_{\rm Kin}(\Xi_c^+) - m_{\rm TRUE}(\Xi_c^+), \tag{5.2}$$

where $m_{\rm Kin}$ is the invariant mass calculated with a kinematic fit applied to improve mass resolution, where the Ξ_c^+ candidate is constrained to originate from its associated PV. The $m_{\rm TRUE}$ variable is calculated with the Ξ_c^+ mass used as an input in the simulation. The `TRUE` information ensures that all the reconstructed tracks are linked to the correct particle hypothesis. After testing many models, the combination of two Gaussian functions with a shared mean is found to describe the distribution accurately. The resolution can then be determined using the following formula:

$$\sigma = \sqrt{f_1 \sigma_1^2 + (1 - f_1)\sigma_2^2} \tag{5.3}$$

where $\sigma_{1,2}$ are the resolutions of the first and second Gaussian function and f_1 is:

$$f_1 = \frac{N_1}{N_{total}}, \tag{5.4}$$

where N_1 is the number of candidates under the first Gaussian distribution and N_{total} is the total number of candidates. The results of the fit are shown in Fig. 5.2 and the fit parameters are listed in Table 5.7. The resolution is found to be

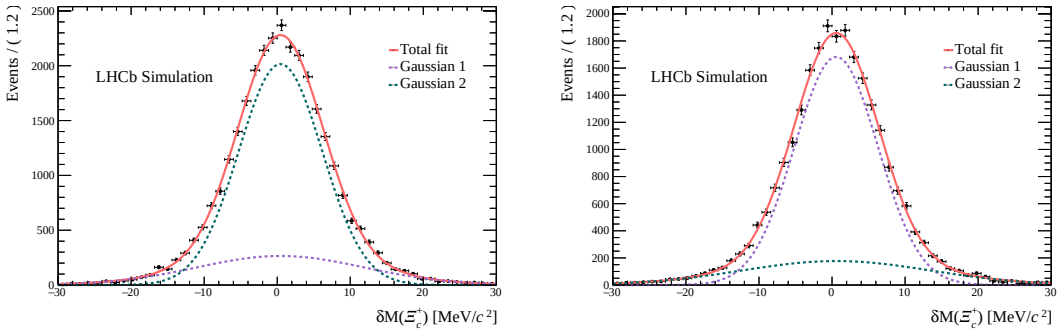

(a) (b)

Figure 5.2 Unbinned maximum likelihood fit to the Ξ_c^+ invariant mass spectrum for 2012 (a) and 2016 (b) simulation. The shape is modelled by the combination of two Gaussian functions.

Table 5.7 Resolution of the Ξ_c^+ baryon in simulation determined by the model shown in Fig. 5.2.

	Year	$\delta M_{\Xi_c^+}$ [MeV]	σ_1 [MeV]	σ_2 [MeV]	σ [MeV]	f_1
Ξ_c^+	2012	0.45 ± 0.04	11.47 ± 0.27	5.71 ± 0.07	7.31 ± 0.09	0.21
Ξ_c^+	2016	0.58 ± 0.04	12.90 ± 0.31	5.72 ± 0.07	7.62 ± 0.09	0.19

$\sigma = 7.31 \pm 0.09$ and $\sigma = 7.62 \pm 0.09$ for 2012 and 2016 simulation, respectively. Indicating that our selection is around $\pm 1.5\sigma$ of the expected Ξ_c^+ mass.

5.6.1 Multivariate selection

A multivariate analysis (MVA) is performed using the TMVA toolkit [84] to further reduce the number of background candidates. The signal input is from the simulated samples, where the PID variables of the final state particles have been corrected using PID calibration data prior to the training. One PID variable per track has been used as an input in the multivariate analysis. The 2012 and 2016 simulation are used for training of the Run 1 and Run 2 MVA, respectively. The background sample is found from the higher mass sidebands of the data sample, where the candidates are chosen to lie in the range $6200 < m(\Xi_c^+ K^- \pi^-) < 6300$ MeV. The lower mass sideband is not used due to expected partially reconstructed contributions. Both boosted decision tree (BDT) and gradient boosted decision tree (BDTG) classifiers have been trained, and the highest performing algorithm will be chosen. The discriminating variables used as inputs for the MVA are listed

Table 5.8 List of discriminating variables used for the multivariate analysis.

Variable	Candidate	Definition
$1-\sqrt{1-ProbNN}$	p, K^-, and $\pi^\pm$	Probability that the daughters are correctly identified
$\log(P_T)$	p, K^-, $\pi^\pm$, and Ξ_c^+	Transverse momentum
$\log(\chi^2_{IP})$	Ω_b^- and Ξ_c^+	Impact parameter χ^2 w.r.t the PV
$\arccos(DIRA)$	Ω_b^- and Ξ_c^+	Cosine of the direction angle
$\log(\chi^2_{FD})$	Ω_b^-	Flight distance χ^2 w.r.t the PV
$\log(\min(P_T))$	p, K^- and π^+	Minimum transverse momentum of the Ξ_c^+ daughters
$\log(\min(\chi^2_{IP}))$	p, K^-, and π^+	Minimum impact parameter χ^2 of the Ξ_c^+ daughters
$\log(\chi^2_{DTF}/ndf)$	Ω_b^-	χ^2 of the DTF vertex fit per degree of freedom
$\log(\chi^2_{vertex})$	Ω_b^- and Ξ_c^+	χ^2 from the vertex fit

in Table 5.8.

The normalised distributions of signal and background for each input variable described are shown in Fig. 5.3. Some variables show good separation between signal and background, namely the PID and χ^2_{IP} distributions. Variables with a more discernible difference between signal and background increase the efficiency of the MVA, leading to an improved signal to background ratio in the data samples.

The receiver-operator curve (ROC) is the signal efficiency vs. the background rejection, shown in Fig. 5.4a, for the BDT (green) and BDTG (purple) algorithms. The performance of both BDT and BDTG classifiers are similar, leading to an inconclusive decision on which algorithm to use in the analysis. The BDT classifier has been chosen to align with the previous analysis of the $\Omega_b^- \to \Omega_c^0\pi^-$ decay. The over-training check of the BDT output is shown in Fig. 5.4b, where a good separation between signal (purple) and background (green) candidates can be seen. The over-training check is performed using a Kolmogorov–Smirnov (KS) test, quantifying the distance between the testing and training samples. The KS test is used to ensure a realistic BDT classification performance.

The optimal selection requirement on the BDT response is found from maximising the Punzi figure of merit [85], given by:

$$FoM = \frac{\epsilon}{a/2 + \sqrt{B}}, \tag{5.5}$$

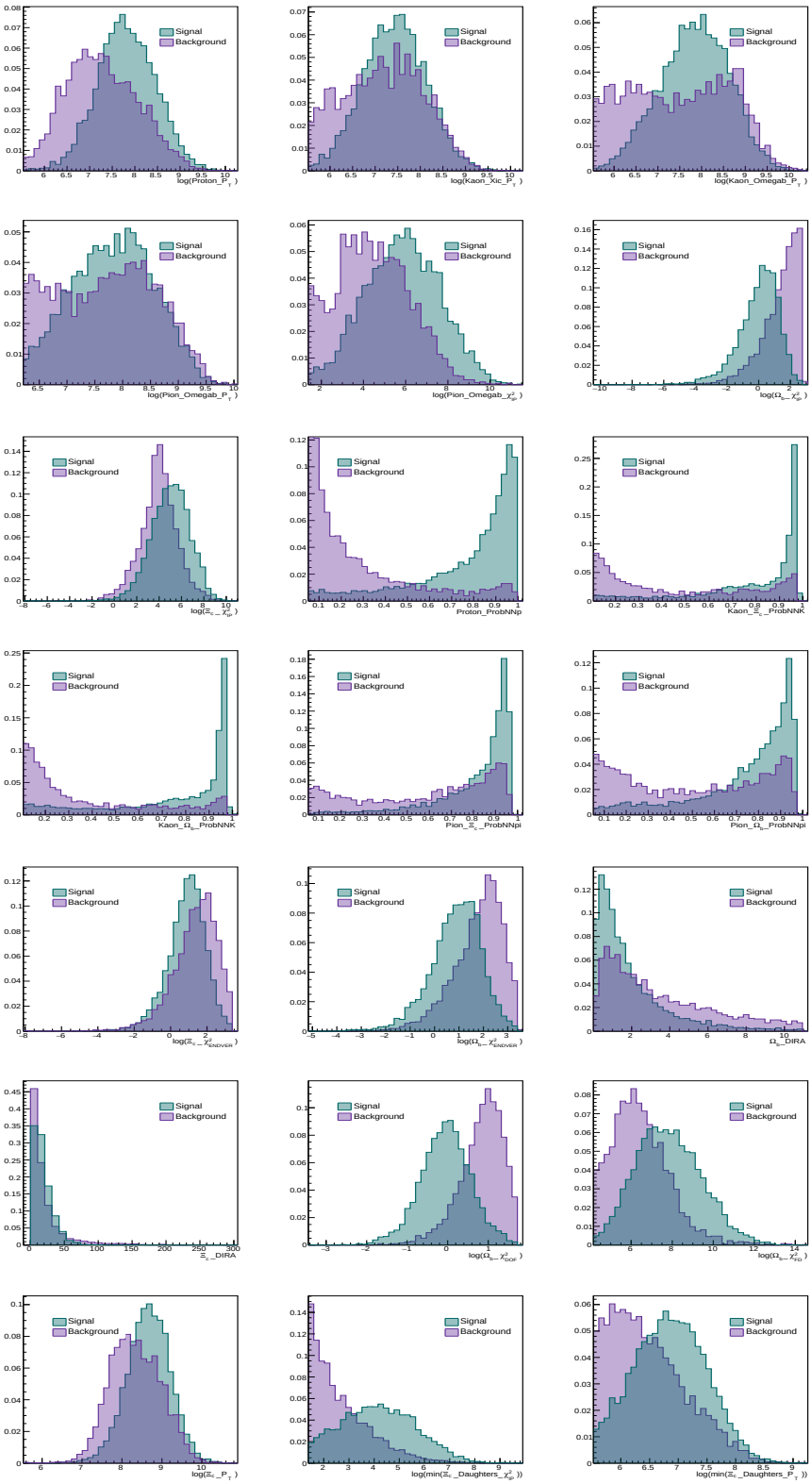

Figure 5.3 Variable distributions between signal (green) and background (purple) for Run 2 in the $\Omega_b^- \to \Xi_c^+ K^- \pi^-$ decay.

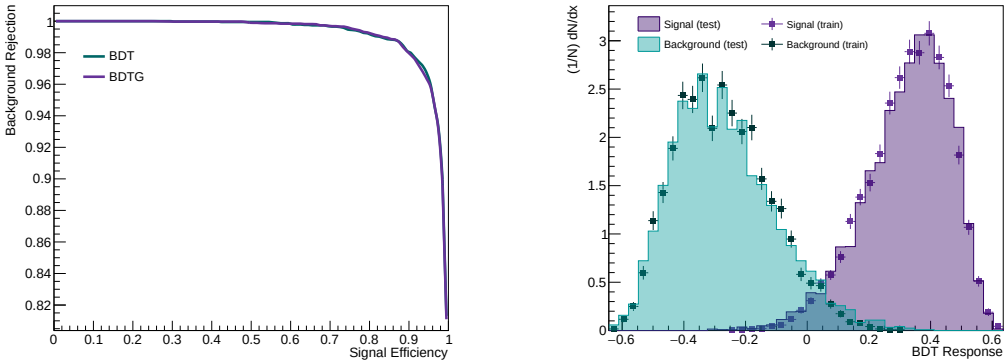

(a) Receiver-operator curve. (b) Over-training check of the BDT classifier

Figure 5.4 On the left is the receiver-operator curve for BDT and BDTG response (a) and on the right is the over-training check (b).

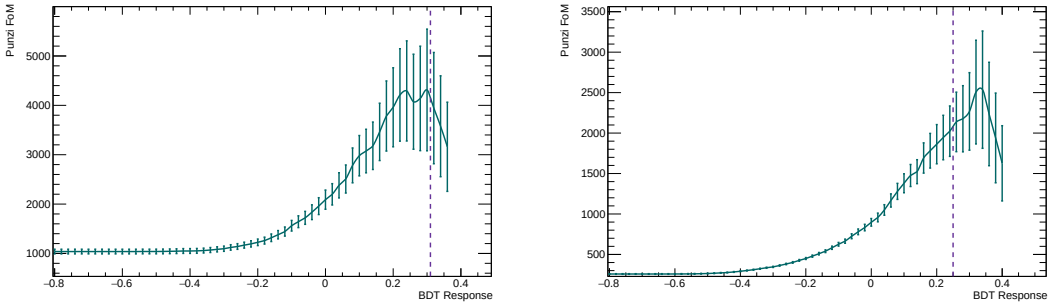

(a) Optimal BDT requirement for Run 1. (b) Optimal BDT requirement for Run 2.

Figure 5.5 The BDT response vs. the Punzi significance for the $\Omega_b^- \to \Xi_c^+ K^- \pi^-$ decay. Figure (a) is for Run 1 and gives an optimal BDT requirement of BDT > 0.31. Figure (b) is for Run 2 and gives an optimal BDT requirement of BDT > 0.25.

where ϵ is the signal efficiency in simulation, B is the number of background events in the mass region $6200 < m(\Xi_c^+ K^- \pi^-) < 6256$ MeV, roughly corresponding to the number of background candidates in the Ω_b^- mass window ($\pm 2\sigma$). The parameter a is the number of standard deviations for a desired significance, which has been set to 5, corresponding to a discovery. The figure of merit as a function of BDT response is shown in Fig. 5.5, where the purple dashed line indicates the optimal requirements at BDT > 0.31 and BDT > 0.25 for Run 1 and Run 2 respectively.

Fluctuations are seen towards the high end of the BDT response. This is caused by the low number of background candidates remaining in this region, leading to large uncertainties. The significance is only calculated until the number of background candidates reaches zero. To mitigate the effects of the fluctuations

the optimal choice for the BDT response is chosen ensuring that the normalised Run 1 and Run 2 signal mass distributions are of a similar size. Around 4% of all selected events contain multiple candidates, these have been removed from our sample.

5.7 Fit model for $\Xi_c^+ K^- \pi^-$ mass spectrum

The $\Xi_c^+ K^- \pi^-$ mass distribution for the selected candidates is shown in Fig. 5.8. The resultant $\Xi_c^+ K^- \pi^-$ mass spectrum is modelled by performing an extended unbinned maximum likelihood fit. The combinatorial background shape is described by an exponential function where the yield is allowed to vary in the fit and the parameter fixed according to the wrong-sign sample, $\Omega_b^- \to \Xi_c^+ K^- \pi^+$, which is processed in the same way as the right-sign combinations. No signal is expected in the wrong-sign sample due to the violation of charge conservation. The main sources of background are due to the partially reconstructed decays $\Omega_b^- \to \Xi_c^+ K^- \rho^- (\to \pi^- \pi^0)$ and $\Omega_b^- \to \Xi_c^{\prime +} (\to \Xi_c^+ \gamma) K^- \pi^-$, where the π^0 and γ are not reconstructed. The shape of these contributions are taken from simulated samples, where the yield is allowed to vary in the fit. The shape of misidentified decays $\Omega_b^- \to \Xi_c^+ K^- K^-$ is also based off simulated samples, where the yield is fixed. The yield ratio is given by:

$$\frac{N_{\Xi_c^+ K^- K^-}}{N_{\Xi_c^+ K^- \pi^-}} = 2.8\%, \tag{5.6}$$

based on the parameters of the Cabibbo-Kobayashi-Maskawa (CKM) matrix, $|\mathrm{V}_{us}|^2/|\mathrm{V}_{ud}|^2 \approx 5\%$ corrected by the difference in reconstruction efficiency and the phase space. The signal shape is modelled by the combination of two Gaussian functions with a shared mean, which is verified by testing different shape hypotheses on the simulated samples.

5.7.1 Partially reconstructed decays

Samples for six possible feed-down components have been considered, where a feed-down is a partially reconstructed decay which appears in the mass spectrum of the signal decay. The first two components listed in Table 5.9, $\Omega_b^- \to \Xi_c^{\prime +} (\to \Xi_c^+ \gamma) K^- \pi^-$ and $\Omega_b^- \to \Omega_c^{**0} (\to \Omega_c^0 \gamma) \pi^-$, have a photon missing

Table 5.9 Feed-down components which may appear in the mass distribution of the two decay modes.

Description	Sample Size	Details
$\Omega_b^- \to \Xi_c'^+(\to \Xi_c^+\gamma)K^-\pi^-$	500000 (2016)	γ invisible
$\Omega_b^- \to \Omega_c^{*0}(\to \Omega_c^0\gamma)\pi^-$	600000 (2016)	γ invisible
$\Omega_b^- \to \Xi_c^+K^-\rho^-(\to \pi^-\pi^0)$	5M (2016)	π^0 invisible
$\Omega_b^- \to \Omega_c^0\rho^-(\to \pi^-\pi^0)$	250000 (2016)	π^0 invisible
$\Omega_b^- \to \Xi_c^+K^-K^-$	1M (2016)	Misidentified π^-
$\Omega_b^- \to \Omega_c^0K^-$	1M (2016)	Misidentified π^-

from the reconstruction which accounts for the shift downwards in the Ω_b^- mass distribution. In the $\Omega_b^- \to \Xi_c^+K^-\rho^-$ and $\Omega_b^- \to \Omega_c^0\rho^-$ decays there is a missing π^0 in the reconstruction from $\rho^- \to \pi^-\pi^0$. The selection criteria have been applied to all simulated samples. In the partially reconstructed decays containing a ρ^- a small number of events remained after selections, leading to an uneven mass distribution. To improve the distribution the decay has also been produced through RapidSim, an application for fast simulation of heavy-quark hadron decays, which provides a smoother shape [86]. The mass distribution of the RapidSim sample is given in Fig. 5.6 (in purple) with the mass distribution from simulation after all selection requirements have been applied (in green) superimposed, a good agreement between the two samples is seen. As the simulated and RapidSim samples are similar, the latter is used in the fit to avoid statistical fluctuations. The feed-down component from $\Omega_b^- \to \Omega_c^0\rho^-$ is extremely broad, differing from the shape found in the previous analysis [65]. However, the $\Omega_c^0\rho^-$ shape had previously been modelled using an ARGUS function. The final component is from the K^- being misidentified as a π^-. This decay is colour suppressed and therefore should have a yield of around 5% of the total signal yield. This is corrected by the reconstruction efficiency, as shown in Eq. 5.6.

Modelling Ω_b^- in simulation

The Ω_b^- mass distribution is first investigated in simulation in order to determine the appropriate model to use when performing a fit to the data. After all selection requirements have been applied the $\Xi_c^+K^-\pi^-$ mass distribution is studied by performing a fit to $\delta M_{\Xi_c^+K^-\pi^-}$, which is defined as:

$$\delta M_{\Xi_c^+K^-\pi^-} = \mathrm{m_{Kin}}(\Omega_b^-) - \mathrm{m_{TRUE}}(\Omega_b^-), \tag{5.7}$$

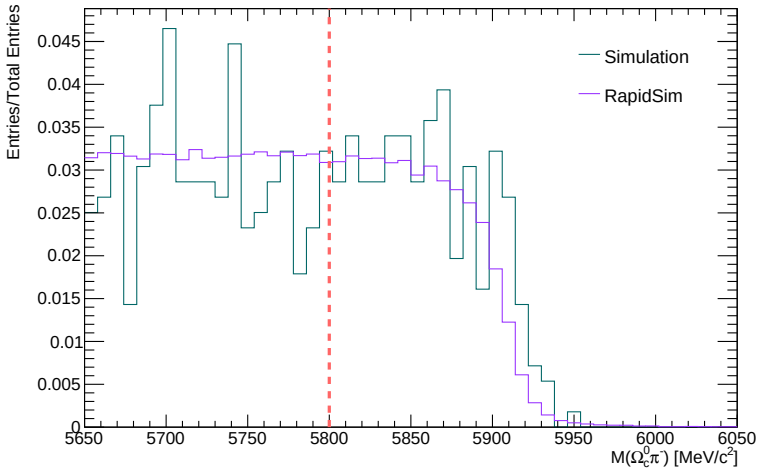

Figure 5.6 Mass distribution of $\Omega_c^0\pi^-$ for the RapidSim sample in purple and the simulated sample in green. The red line indicates the start of the region which is used for the Ω_b^- mass fit.

Table 5.10 Parameters determined from the double Gaussian fit performed to the simulated Ω_b^- invariant mass distribution, shown in Fig. 5.7.

Year	$\delta M_{\Xi_c^+K^-\pi^-}$ [MeV]	σ_1 [MeV]	σ_2 [MeV]	$\frac{\sigma_1}{\sigma_2}$	σ [MeV]	f_1
2012	1.0 ± 0.1	32.9 ± 1.4	13.7 ± 0.2	2.4 ± 0.1	16.9 ± 0.3	0.11
2016	1.5 ± 0.1	34.3 ± 1.6	13.7 ± 0.2	2.5 ± 0.1	17.8 ± 0.3	0.13

where m_{Kin} is the invariant mass with a kinematic fit applied to improve mass resolution, where the Ξ_c^+ candidate mass is constrained to its known value, and the Ω_b^- candidate is constrained to originate from its associated PV. The m_{TRUE} variable is the mass when the Ω_b^- mass is used as an input in the simulation. A number of models are tested, including one, two and three Gaussian functions, and a Crystal Ball (CB) function. The $\Xi_c^+K^-\pi^-$ invariant mass is described well by the combination of two Gaussian functions with a shared mean, shown in Fig. 5.7. The purple and green dashed lines indicate the two Gaussian functions, and the red solid line is the combination. The parameters of both Gaussian functions are shown in Table 5.10, along with the ratio and f_1, which is defined as the ratio of candidates under the first Gaussian function compared to the total number of candidates. The parameters which will be fixed when performing the fit to data are σ_1/σ_2 and f_1.

The total fit function is described by the following equation:

$$F(m(\Xi_c^+K^-\pi^-)) = N\left(e^{-\frac{(m-\mu)^2}{2\sigma_1^2}} + f_1 e^{-\frac{(m-\mu)^2}{2\sigma_2^2}} + f_b e^{\lambda m}\right), \tag{5.8}$$

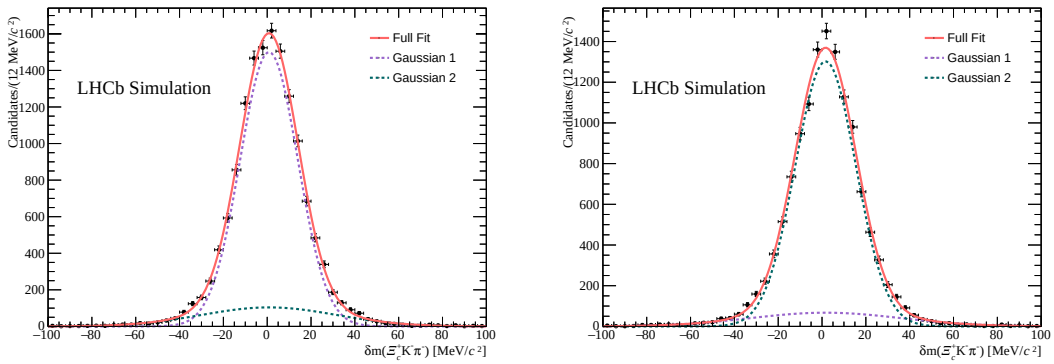

(a) (b)

Figure 5.7 Distribution of $\delta M_{\Xi_c^+ K^- \pi^-}$ for simulated $\Omega_b^- \to \Xi_c^+ K^- \pi^-$ decays. The mass shape is described well by the combination of two Gaussian functions with a shared mean, where (a) is 2012 and (b) is 2016 simulation.

where μ is the mean, σ_1 and σ_2 are the resolutions, and N and f_b are yield parameters, all of which are allowed to vary in the fit. The total resolution, σ, is calculated using Eq. 5.3.

The parameters f_1 and the ratio between σ_1 and σ_2 are fixed according to the simulation. The $\Xi_c^+ K^- \pi^-$ mass spectrum is shown in Fig. 5.8 where the extended unbinned maximum likelihood fit has been performed.

The selection requirements for the BDT response are 0.31 and 0.25 for Run 1 and Run 2 respectively. The fit model has been performed to Run 1 and Run 2 data separately to ensure a correct scaling of luminosity. The resulting parameters for the three fits are given in Table. 5.11. All uncertainties are statistical, the systematic uncertainties will be described and calculated in a later section. The yields between Run 1 and Run 2 scale correctly according to luminosity.

5.8 Selection of $\Omega_b^- \to \Omega_c^0 \pi^-$ candidates

The $\Omega_b^- \to \Omega_c^0 \pi^-$ decay is used as a control mode as its been studied previously, and to determine the ratio of branching fractions between the two decay modes. The Ω_c^0 candidates are formed by the combination of four tracks which are detached

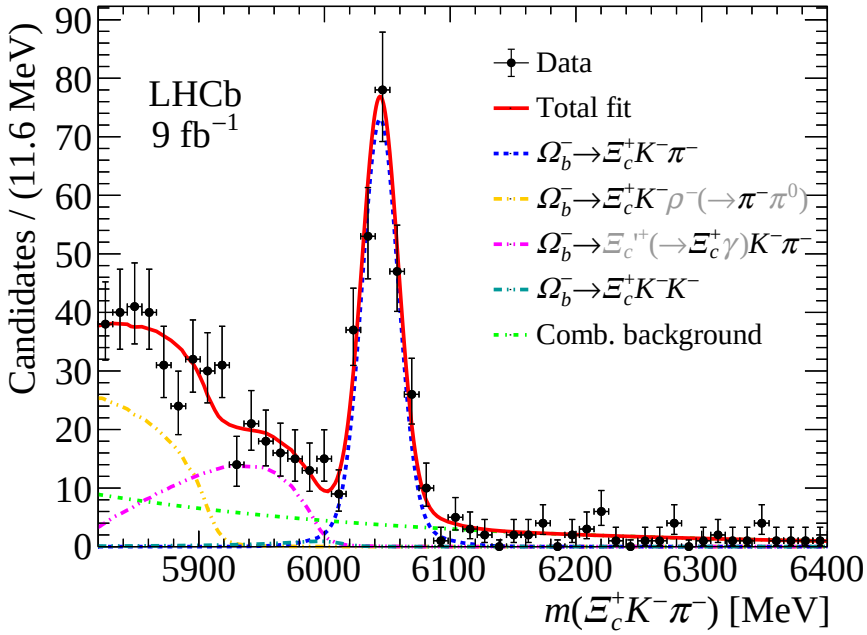

Figure 5.8 The extended unbinned maximum likelihood fit to the $\Xi_c^+ K^- \pi^-$ mass spectrum. The total fit is shown in red, the signal component is formed of two Gaussian functions and is shown by the blue dashed line, the combinatorial background shape is shown by the green dashed line, and the partially reconstructed decays are displayed by the dashed yellow, pink and teal distributions.

Table 5.11 Parameters found from the unbinned maximum likelihood fit performed on the $\Xi_c^+ K^- \pi^-$ mass distribution, shown in Fig. 5.8. The fit function is given by Eq. 5.8.

Parameter	Run 1 & 2	Run 1	Run 2
σ_1 [MeV/c^2]	14.2 ± 1.0	16.8 ± 4.1	14.2 ± 1.1
σ_2 [MeV/c^2]	33.8 ± 2.8	40.3 ± 10.2	35.3 ± 3.1
σ [MeV/c^2]	17.9 ± 1.3	21.4 ± 5.3	17.8 ± 1.4
$M(\Omega_b^-)$ [MeV/c^2]	6044.3 ± 1.1	6041.0 ± 3.7	6044.6 ± 1.3
$N_{\Xi_c^+ K^- \pi^-}$	240.4 ± 17.3	43.9 ± 5.4	199.2 ± 12.6
$N_{\Xi_c^+ K^- \rho^-}$	149.9 ± 19.1	27.2 ± 3.3	123.5 ± 7.8
$N_{\Xi_c'^+ K^- \pi^-}$	154.3 ± 22.2	28.1 ± 3.5	127.5 ± 8.1
$N_{\Xi_c^+ K^- K^-}$	6.7 ± 0.5	1.1 ± 0.2	5.6 ± 0.4
N_{BKG}	177.8 ± 26.0	13.5 ± 8.1	159.4 ± 23.0

Table 5.12 Resolution of the Ω_c^0 baryon in simulation determined by the fit model shown in Fig. 5.9.

	Year	$\delta M_{\Omega_c^0}$ [MeV]	σ_1 [MeV]	σ_2 [MeV]	σ [MeV]	f_1
Ω_c^0	2012	0.36 ± 0.04	9.79 ± 0.29	4.75 ± 0.07	5.85 ± 0.09	0.16
Ω_c^0	2016	0.42 ± 0.03	10.52 ± 0.19	4.79 ± 0.05	6.29 ± 0.07	0.19

from the primary pp interaction vertex for each event. Then the Ω_b^- candidates are formed by combining the reconstructed Ω_c^0 candidate with a pion. The selection requirements applied to this decay mode are described in Sec. 5.3. The $\Omega_c^0 \to pK^-K^-\pi^+$ decay produces two identical kaons, which are indistinguishable from each other to our analysis software. The magnitude of their transverse momentum can be used to identify one from the other, for each candidate there will be a high and low P_T kaon. All features of the kaon with the highest transverse momentum will be transferred into a set of variables called *KHigh*, and the lowest will be put into another set called *KLow*. The variables that are propagated across are the P_T, total momentum (P), momentum in the x, y, and z direction (P_X, P_Y, P_Z), the energy and the probability that the kaon is a correctly identified (ProbNNk). An additional selection requirement is imposed on the mass of the Ω_c^0: $2685 < m(pK^-K^-\pi^+) < 2705\,\text{MeV}$, which is $\pm 2\sigma$ of the expected Ω_c^0 mass. This selection is validated through simulated samples.

Resolution of Ω_c^0

As described in Sec. 5.6, a crosscheck of the selection requirements for the Ω_c^0 mass is performed by measuring the resolution in simulation. As previously, all offline selection requirements are applied to the $\Omega_b^- \to \Omega_c^0\pi^-$ simulated samples, omitting the Ω_c^0 mass requirement. An unbinned maximum likelihood fit is used to model the $\delta M_{\Omega_c^0}$ distribution, where:

$$\delta M_{\Omega_c^0} = m_{\text{Kin}}(\Omega_c^0) - m_{\text{TRUE}}(\Omega_c^0). \tag{5.9}$$

The combination of two Gaussian functions with a shared mean is found to accurately describe the simulated mass distribution. The model applied to the sample is shown in Fig. 5.9 and the fit parameters are listed in Table 5.12.

The total resolution is calculated to be $\sigma = 5.85 \pm 0.09\,\text{MeV}$ and $\sigma = 6.29 \pm 0.07\,\text{MeV}$ for 2012 and 2016 simulation respectively. Indicating that our selection is around

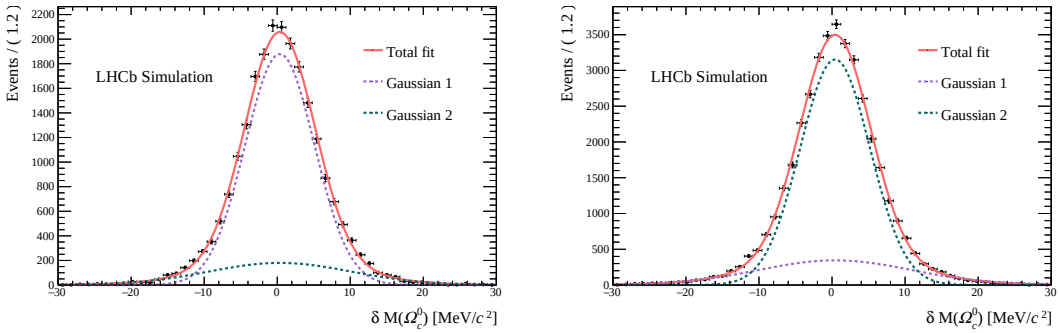

(a) (b)

Figure 5.9 Unbinned maximum likelihood fit to simulated Ω_c^0 candidates for 2012 (a) and 2016 (b). The red curve is modelled by the combination of two Gaussian functions.

$\pm 1.7\sigma$ of the expected Ω_c^0 mass.

Multivariate selection

The BDT classifier which is trained on the $\Omega_b^- \to \Xi_c^+ K^- \pi^-$ decay in Section 5.6.1 is used to reduce combinatorial background in the $\Omega_b^- \to \Omega_c^0 \pi^-$ decay mode, using the same BDT response requirements. This is allowed due to their similar topologies, and allows for a simpler computation of the branching ratio. There is a slight reduction in the efficiency of the BDT response on this decay mode as it is not specifically trained on the $\Omega_b^- \to \Omega_c^0 \pi^-$ decay.

5.9 Fit model for $\Omega_c^0 \pi^-$ mass spectrum

The resultant $\Omega_c^0 \pi^-$ mass spectrum is modelled by performing an extended unbinned maximum likelihood fit. The combinatorial background shape is modelled by an exponential function, $e^{\lambda m}$, where the parameter λ is fixed using a study of the Ω_c^0 side-bands. The Ω_c^0 side-bands are defined as:

$$|M(pK^-K^-\pi^+) - M(\Omega_c^0)| < 25\,\text{MeV} \text{ and } M(\Omega_b^-) > 6150\,\text{MeV},$$

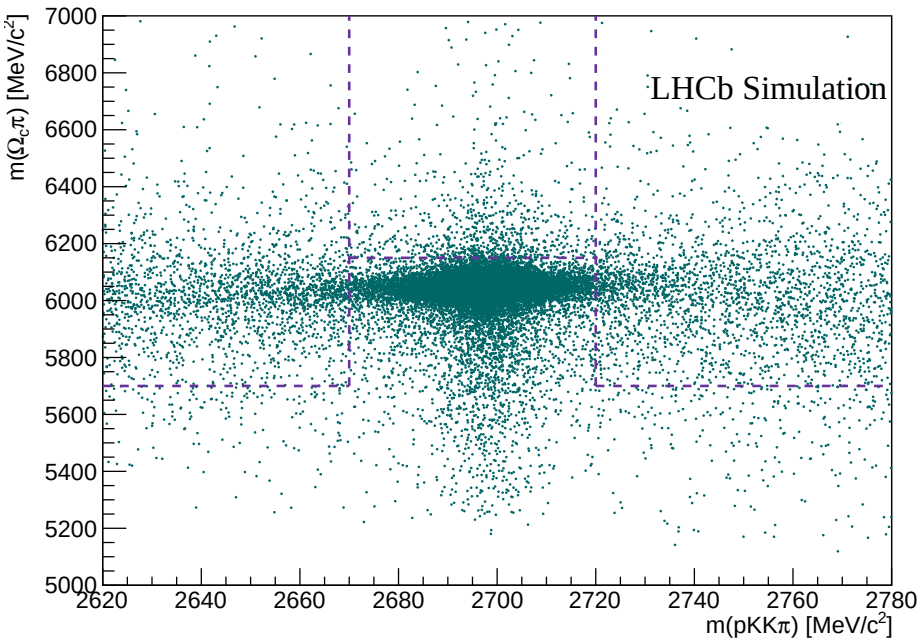

Figure 5.10 The distribution of Ω_b^- candidates in the $\Omega_b^- \to \Omega_c^0\pi^-$ simulated sample. The purple dashed lines indicate the areas that are used for our side-band sample.

Run	λ [MeV^{-1}]
1	$(-9.53 \pm 4.36) \times 10^{-3}$
2	$(-2.66 \pm 0.38) \times 10^{-3}$
1 & 2	$(-2.77 \pm 0.38) \times 10^{-3}$

Table 5.13 Results for the modelling of the Ω_c^0 sidebands, used to parameterise the combinatorial background shape in $\Omega_b^- \to \Omega_c^0\pi^-$ decays.

or

$$|M(pK^-K^-\pi^+) - M(\Omega_c^0)| > 25\,\text{MeV and } M(\Omega_b^-) > 5700\,\text{MeV}.$$

This is the same technique used in the previous analysis of this decay mode, described in Ref. [65]. Figure. 5.10 shows the 2D distribution of m($\Omega_c^0\pi^-$) versus m($pK^-K^-\pi^+$) in simulation, the side-band regions are indicated by the purple dashed lines.

The resultant fit model to the Ω_c^0 sidebands is shown in Fig. 5.11, which has been performed separately for Run 1, Run 2, and the combination of the two. The results are given in Table. 5.13. Due to the limited size of the Run 1 data sample the combined value of λ has been used when modelling to the full data sample.

The other sources of background are due to three partially reconstructed decays:

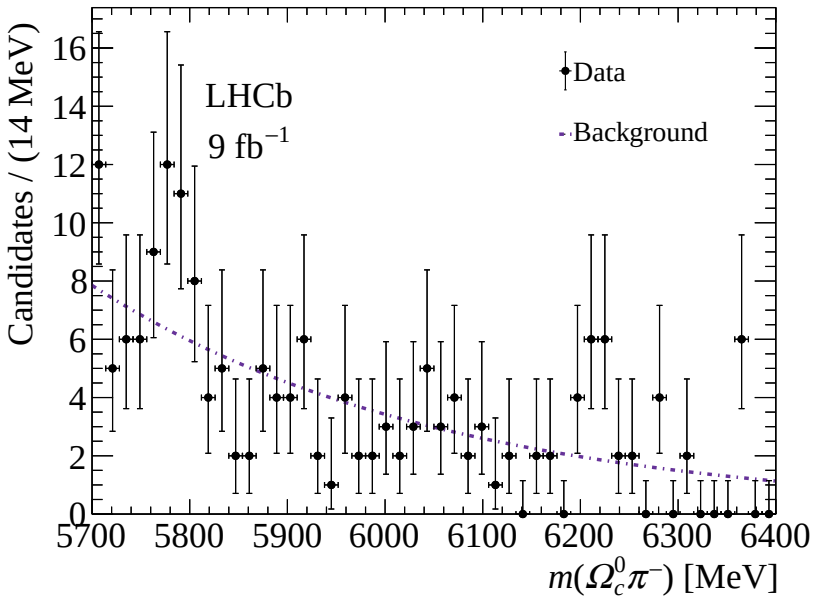

Figure 5.11 An unbinned maximum likelihood fit to the $\Omega_c^0\pi^-$ invariant mass spectrum in the Ω_c^0 sidebands. The combinatorial background can be fitted with an exponential function, indicated by the purple dashed line. The exponential function is commonly used to describe combinatorial background.

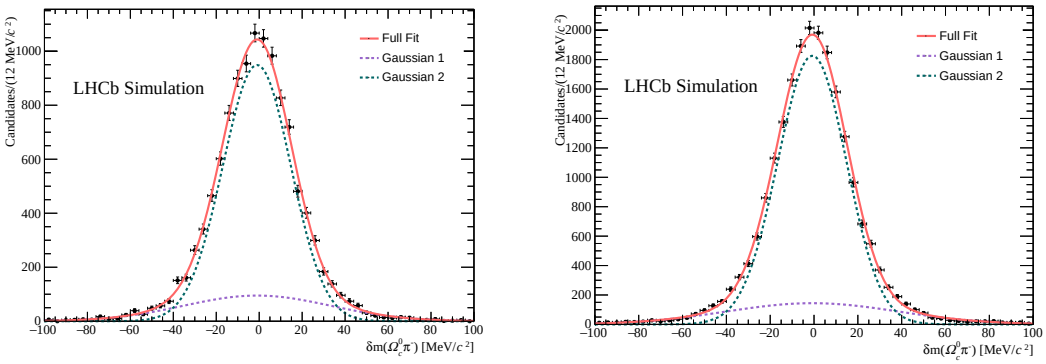

(a) (b)

Figure 5.12 Unbinned maximum likelihood fit to $\delta M_{\Omega_c^0\pi^-}$ for the $\Omega_b^- \to \Omega_c^0\pi^-$ simulated sample. The data is described well by the combination of two Gaussian functions with a shared mean, where (a) is 2012 and (b) is 2016 simulation.

$\Omega_b^- \to \Omega_c^0\rho^-$ where $\rho^- \to \pi^-\pi^0$, and $\Omega_b^- \to \Omega_c^{*0}\pi^-$ where $\Omega_c^{*0} \to \Omega_c^0\gamma$, where the π^0 and γ are not reconstructed. The shape of these contributions are taken from simulated samples, where the yield is allowed to vary in the fit. The shape of the misidentified decays $\Omega_b^- \to \Omega_c^0 K^-$ is also based off of simulated samples, where the yield is fixed according to the ratio found in Section. 5.7. The signal shape is modelled by the combination of two Gaussian functions with a shared mean, as before this is verified by testing different shape hypotheses in the simulated samples.

Modelling Ω_b^- in simulation

The Ω_b^- mass distribution in $\Omega_b^- \to \Omega_c^0\pi^-$ decays is investigated in simulation to determine the appropriate model to use when performing the fit to data. As previously, all selection requirements are applied to the $\Omega_c^0\pi^-$ candidates, and a fit to $\delta M_{\Omega_c^0\pi^-}$ is performed. A single, double and triple Gaussian function, as well as a CB function are tested. As with the $\Omega_b^- \to \Xi_c^+ K^-\pi^-$ decay, the $\Omega_c^0\pi^-$ mass distribution is described well by the combination of two Gaussian functions with a shared mean, shown in Fig. 5.12.

The total fit is shown in red, and the purple and green dashed lines indicate the first and second Gaussian function respectively. The parameters determined from

Table 5.14 Parameters determined from the double Gaussian fit performed to the simulated Ω_b^- invariant mass distribution, shown in Fig. 5.12.

Year	$\delta M_{\Omega_c^0\pi^-}$ [MeV]	σ_1 [MeV]	σ_2 [MeV]	$\frac{\sigma_1}{\sigma_2}$	σ [MeV]	f_1
2012	-1.1 ± 0.2	35.2 ± 1.6	16.0 ± 0.3	2.2 ± 0.1	20.6 ± 0.4	0.17
2016	-1.0 ± 0.1	39.3 ± 1.8	15.7 ± 0.2	2.5 ± 0.1	21.6 ± 0.3	0.17

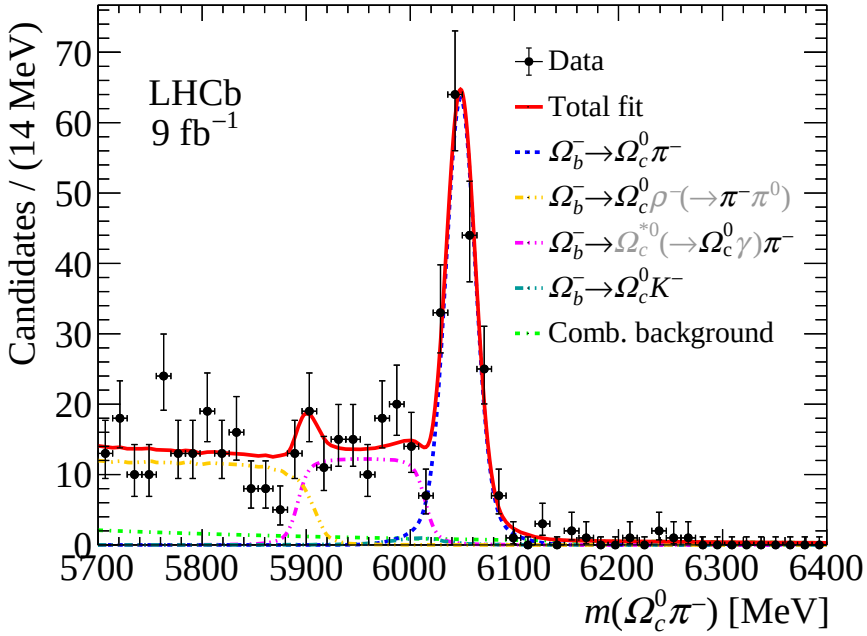

Figure 5.13 The extended unbinned maximum likelihood fit to the $\Omega_c^0\pi^-$ mass spectrum. The total fit is shown in red, the signal component is formed of two Gaussian functions and is shown by the blue dashed line. The combinatorial background shape is indicated by the green dashed line and the partially reconstructed decays are given by the dashed yellow, pink and teal shapes.

the fit are shown in Table 5.14, along with the ratio between the two resolutions and the value of f_1. The parameters which are fixed when performing a fit to the data are σ_1/σ_2 and f_1.

The total fit function is described by Equation. 5.8, where the mean, resolutions and yields are allowed to vary in the fit. The $\Omega_c^0\pi^-$ invariant mass distribution for Run 1 and 2 are shown in Fig. 5.13 where an extended unbinned maximum likelihood fit has been performed. The selection requirements on the BDT response are 0.31 and 0.25 for Run 1 and Run 2 respectively. The fit model has been performed to Run 1 and Run 2 separately. The parameters found from the three fits are given in Table. 5.15. All uncertainties are statistical, the systematic uncertainties will be described and calculated in a later section. The yields between Run 1 and Run 2 scale correctly according to the luminosity.

Table 5.15 Parameters determined from the unbinned maximum likelihood fit performed on the $\Omega_c^0\pi^-$ mass distribution, shown in Fig. 5.13.

Parameter	Run 1 & Run 2	Run 1	Run 2
σ_1 [MeV/c^2]	13.8 ± 1.1	10.2 ± 3.0	14.4 ± 1.2
σ_2 [MeV/c^2]	32.4 ± 2.9	22.4 ± 6.7	36.0 ± 3.3
σ [MeV/c^2]	18.4 ± 1.5	13.1 ± 3.9	19.8 ± 1.7
$M(\Omega_b^-)$ [MeV/c^2]	6048.4 ± 1.3	6048.7 ± 3.5	6048.6 ± 1.4
$N_{\Omega_c^0\pi^-}$	174.3 ± 13.9	20.0 ± 3.7	155.2 ± 8.8
$N_{\Omega_c^{*0}\pi^-}$	107.8 ± 12.3	12.4 ± 2.3	96.2 ± 5.5
$N_{\Omega_c^0\rho^-}$	194.2 ± 18.2	22.2 ± 4.1	172.3 ± 9.8
$N_{\Omega_c^0K^-}$	4.8 ± 0.4	0.6 ± 0.1	4.3 ± 0.2
$N_{\rm BKG}$	50.9 ± 17.3	13.0 ± 7.9	35.9 ± 14.3

5.10 Measurement of the branching fraction

The ratio of branching fractions between the two decay modes, $\Omega_b^- \to \Xi_c^+K^-\pi^-$ and $\Omega_b^- \to \Omega_c^0\pi^-$ is calculated using the number of signal candidates found for each mode, corrected by the efficiency. The efficiency is found from the full phase-space simulated samples. First, the efficiency corrected yields are obtained for each run separately:

$$N^{corr}_{\Xi_c^+K^-\pi^-} = \sum_{e=1}^{N^{rec}_{\Xi_c^+K^-\pi^-}} 1/\epsilon^e_{\Xi_c^+K^-\pi^-} = N^{rec}_{\Xi_c^+K^-\pi^-}\frac{1}{\overline{\epsilon_{\Xi_c^+K^-\pi^-}}}, \tag{5.10}$$

and

$$N^{corr}_{\Omega_c^0\pi^-} = N^{rec}_{\Omega_c^0\pi^-}/\epsilon_{\Omega_c^0\pi^-}, \tag{5.11}$$

where N_X^{corr} is the number of X candidates corrected by efficiency, N_X^{rec} is the number of reconstructed X candidates, where X = $\Xi_c^+K^-\pi^-$ or $\Omega_c^0\pi^-$. The parameter $\epsilon^e_{\Xi_c^+K^-\pi^-}$ is the value of efficiency determined for every event in the selected $\Omega_b^- \to \Xi_c^+K^-\pi^-$ simulated sample, and $\epsilon_{\Omega_c^0\pi^-}$ is the averaged efficiency for the $\Omega_b^- \to \Omega_c^0\pi^-$ sample. The difference in calculation of the efficiencies is due to the kinematics of the two decay modes. In the $\Omega_b^- \to \Omega_c^0\pi^-$ decay the energies of the Ω_c^0 and π^- are fixed for the two-body decay. For the $\Omega_b^- \to \Xi_c^+K^-\pi^-$ decay the variation in efficiency across the $\Xi_c^+K^-\pi^-$ Dalitz plot must be taken into account. The event based efficiencies $\epsilon^e_{\Xi_c^+K^-\pi^-}$ are determined using the full phase-space simulated samples which have passed all requirements including the BDT response selection.

The local values of efficiency for each candidate in the data sample is determined by comparing the density of the reconstructed and generated simulation events in the vicinity of the data point:

$$\epsilon^{e}_{\Xi_c^+ K^-\pi^-} = \sum_{i=1}^{d^{rec}<R_e} w_i / \sum_{i=1}^{d^{gen}<R_e} w_i, \tag{5.12}$$

where the distance, d, is calculated in the $m(\Xi_c^+\pi^-) \times m(K^-\pi^-)$ variables and R_e is the vicinity radius which is determined individually for every data point and ranges from 0.15 GeV to 0.3 GeV. The values are found by the requirement that the vicinity in consideration, $d < R$ contains from 100 to 200 candidates. Using a range of 300-500 candidates provides a consistent result on the averaged efficiency. The weights, w_i, are found from the Ξ_c^+ Dalitz plot distributions shown in Fig. 5.1, which is assigned to each reconstructed event. The weighting has a negligible impact to the efficiency, indicating that the relative efficiency on the Ξ_c^+ decay variables does not change significantly with the Ξ_c^+ momentum.

The averaged efficiency for the $\Omega_c^0\pi^-$ sample is found as the ratio of reconstructed to generated events in simulation:

$$\epsilon_{\Omega_c^0\pi^-} = N^{rec}_{\Omega_c^0\pi^-}/N^{gen}_{\Omega_c^0\pi^-}. \tag{5.13}$$

The $\Omega_c^0 \to pK^-K^-\pi^+$ decay cannot be parameterised simply, therefore the simulated sample is not weighted and we neglect the impact to the efficiency. The efficiency at different stages of the analysis is shown in Table. 5.16, this includes:

1. The stripping efficiency, ϵ_{strip}, which is determined from the number of candidates remaining after the requirements in the stripping line have been applied.

2. The selection efficiency, ϵ_{sel}, which is the found from the number of candidates remaining after the selection requirements have been applied.

3. The efficiency after the BDT requirement has been applied, ϵ_{BDT}.

4. The event based efficiency defined in Eq. 5.10.

The stripping efficiency for the $\Omega_b^- \to \Xi_c^+K^-\pi^-$ decay is larger due to the $\Omega_b^- \to \Omega_c^0\pi^-$ stripping line containing the trigger requirements. These selections

Table 5.16 Reduction in efficiencies over different stages of the analysis. The averaged value of the efficiency for the event-based procedure is given by $\bar{\epsilon}$.

Decay Mode	Run 1				Run 2			
	ϵ_{strip}	ϵ_{sel}	ϵ_{BDT}	$\bar{\epsilon}$	ϵ_{strip}	ϵ_{sel}	ϵ_{BDT}	$\bar{\epsilon}$
$\Omega_b^- \to \Xi_c^+ K^- \pi^-$	4.2%	0.9%	0.55%	0.55%	5.5%	1.8%	1.3%	1.2%
$\Omega_b^- \to \Omega_c^0 \pi^-$	1.6%	0.9%	0.54%	–	2.7%	1.6%	1.1%	–

are then applied to the $\Omega_b^- \to \Xi_c^+ K^- \pi^-$ decay offline, causing the drop in efficiency. The ratio of branching fractions is calculated from the following equation:

$$\frac{\mathcal{B}(\Omega_b^- \to \Xi_c^+ K^- \pi^-)\mathcal{B}(\Xi_c^+ \to pK^- \pi^+)}{\mathcal{B}(\Omega_b^- \to \Omega_c^0 \pi^-)\mathcal{B}(\Omega_c^0 \to pK^- K^- \pi^+)} = \frac{N^{rec}_{\Xi_c^+ K^- \pi^-}}{\overline{\epsilon_{\Xi_c^+ K^- \pi^-}}} \Big/ \frac{N^{rec}_{\Omega_c^0 \pi^-}}{\epsilon_{\Omega_c^0 \pi^-}}$$
$$= 1.35 \pm 0.11(\text{stat}) \quad (5.14)$$

5.11 Precise measurement of the Ω_b^- mass

The precise measurement of the Ω_b^- mass can be calculated by two different procedures: by doing the weighted averages of the two Ω_b^- masses measured in this analysis, or by taking the Ω_b^- mass from the $\Omega_b^- \to \Xi_c^+ K^- \pi^-$ decay and averaging with the previous LHCb measurements. To average the measurements it is assumed that the momentum scale systematic uncertainty (described in Sec. 6.7) is completely correlated. The weighted average is calculated by the following formula:

$$\bar{x} = \frac{\sum_i w_i x_i}{\sum_i w_i}, \quad (5.15)$$

where x_i corresponds to each value of the mass and the weight, w_i, is equal to the inverse of the uncertainty squared:

$$w_i = 1/(\delta x_i)^2. \quad (5.16)$$

For the first method the values used in the average are $m(\Omega_c^0 \pi^-) = 6048.4 \pm 1.3 \pm 2.0\,\text{MeV}$ and $m(\Xi_c^+ K^- \pi^-) = 6044.3 \pm 1.2 \pm 1.2\,\text{MeV}$. The weighted average is

found to be:

$$\overline{m}(\Omega_b^-) = 6045.4 \pm 1.4\,\text{MeV}.$$

In the second method the previous measurements of the Ω_b^- mass from the LHCb experiment are used, these are: $m(\Omega_c^0\pi^-) = 6045.1 \pm 3.2 \pm 0.8\,\text{MeV}$ [65] and $m(J/\psi\Omega) = 6046.0 \pm 2.2 \pm 0.5\,\text{MeV}$ [87], along with the measurement from this analysis $m(\Xi_c^+K^-\pi^-) = 6044.3 \pm 1.2 \pm 1.2\,\text{MeV}$. This gives a weighted average of

$$\overline{m}(\Omega_b^-) = 6044.8 \pm 1.3\,\text{MeV}.$$

The uncorrelated uncertainties are found through the inverse of the sum of the weights, this is then added in quadrature with the uncertainty due to the correlated systematic [88]. Both values of the weighted average are consistent to within 2σ of the PDG value and has a statistical uncertainty which is competitive with the current value of $m(\Omega_b^-) = 6046.1 \pm 1.7\,\text{MeV}$ [6]. The second method is taken as our final result for the averaged mass as the previous LHCb analysis on the $\Omega_b^- \to \Omega_c^0\pi^-$ decay measured the Ω_b^- mass with a higher precision than our measurement. This is due to a lower systematic uncertainty from measuring a mass difference. The averaged mass determined in this analysis compared to the previous measurements are shown in Fig. 5.14.

5.12 Summary

In this section the analysis strategy was set out, including information on the data and simulated samples used as well as a description of the partially reconstructed decays that have been considered. The selection strategy was described for each stage; stripping and trigger, offline selections and the multivariate analysis technique. The BDT response was optimised using the Punzi figure of merit to find the optimal requirement on the variable. The selections removed a large amount of background from the data sample, allowing for a clean signal peak of the Ω_b^- to be observed in both decay modes. The fit model used for both decays include three partially reconstructed decay modes, a combinatorial background component and the signal peak which is modelled by the combination of two Gaussian functions. The resolution, mass and number of signal candidates of the Ω_b^- was determined from the fits to each decay mode. For the $\Omega_b^- \to \Xi_c^+K^-\pi^-$ decay the mass is $m(\Xi_c^+K^-\pi^-) = 6044.3 \pm 1.2$ MeV and the yield is $N_{\Xi_c^+K^-\pi^-} = 240.4 \pm 17.3$, where

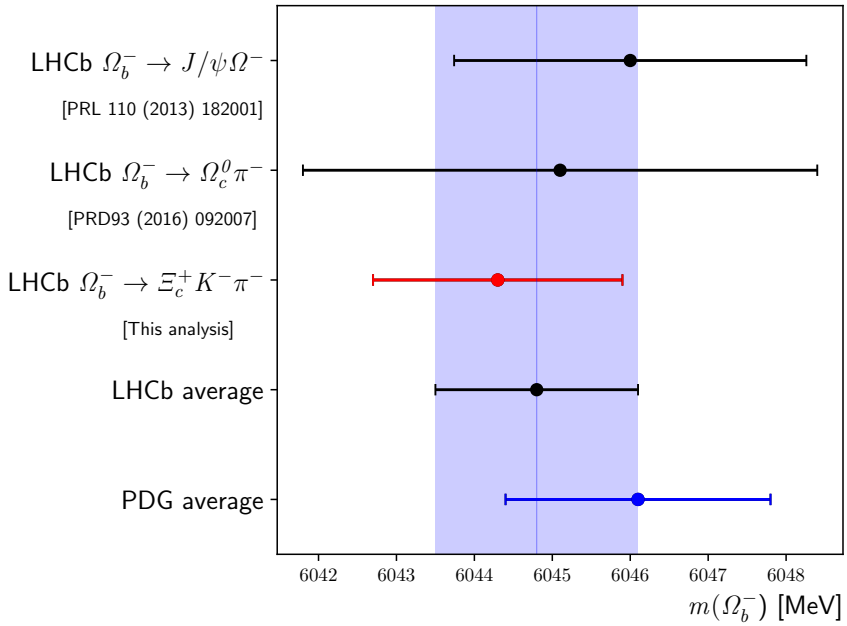

Figure 5.14 Measurements of the Ω_b^- mass from the LHCb experiment, the LHCb average and the PDG average, which includes to the two previous LHCb measurements and one measurement from the CDF collaboration [6].

the uncertainty is statistical. In the $\Omega_b^- \to \Omega_c^0\pi^-$ decay the mass is determined to be $m(\Omega_c^0\pi^-) = 6048.4 \pm 1.3$ and the yield is $N_{\Omega_c^0\pi^-} = 174.3 \pm 13.9$. The relative branching fraction between the two decay modes can be calculated using the number of signal candidates corrected by the efficiency of the simulated samples. The ratio of branching fractions is given by Eq. 5.14 and gives a value of 1.35 ± 0.11 (stat). Finally, a precise measurement of the Ω_b^- mass can be calculated by taking the weighted average of the mass found from the $\Omega_b^- \to \Xi_c^+K^-\pi^-$ decay with the previous LHCb measurements. This gives a value of $\bar{m}(\Omega_b^-) = 6044.8 \pm 1.3$ MeV, which is competitive with the current PDG value [6].

Chapter 6

Observation of excited $\Omega_c^{**0} \to \Xi_c^+ K^-$ decays in exclusive decays of the Ω_b^- baryon

This section will cover the search of the excited Ω_c^0 baryons in the $\Xi_c^+ K^-$ mass spectrum using $\Omega_b^- \to \Xi_c^+ K^- \pi^-$ candidates. Measurements of their mass and width, and an investigation of their quantum numbers will be presented.

6.1 Selection of excited Ω_c^0 states

In the prompt production of the Ω_c^0 baryon five Ω_c^{**0} states were observed. The states were produced with an unknown polarisation and therefore the quantum numbers could not be determined. It is possible to produce the states with a known polarisation through the decay of a baryon containing a b quark. The $\Omega_c^{**0} \to \Xi_c^+ K^-$ decays can be studied in $\Omega_b^- \to \Xi_c^+ K^- \pi^-$ decays, allowing for the study of the quantum numbers.

The previous chapter discussed the selection process and observation of the $\Omega_b^- \to \Xi_c^+ K^- \pi^-$ decays. The final result is shown in Fig. 5.8 and this data sample is used for the following results. The excited Ω_c^0 states are expected to be gathered in one corner of the Dalitz plot, this is tested by taking candidates which are within $\pm 2\sigma$ of the Ω_b^- mass peak shown in Fig. 5.8. The Dalitz plot distribution of the candidates is shown in Fig. 6.1, with the square of the four-momentum

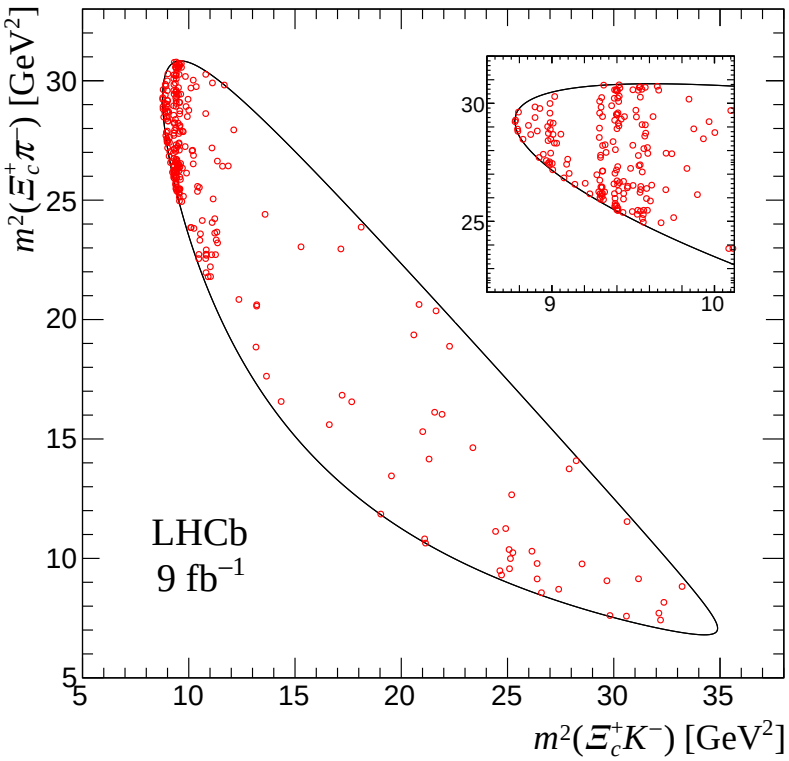

Figure 6.1 Dalitz plot distribution of $\Omega_b^- \to \Xi_c^+ K^- \pi^-$ candidates in the signal region, with the square of the four-momentum of the $\Xi_c^+ K^-$ vs. the $\Xi_c^+ \pi^-$. The inset shows an expanded view of the upper left corner, where the vertical bands correspond to excited Ω_c^0 baryons.

of the $\Xi_c^+ K^-$ vs. the $\Xi_c^+ \pi^-$. Excited Ω_c^0 states are clearly visible in the $\Xi_c^+ K^-$ projection, shown by the vertical bands in the top left corner. No excited Ξ_c^0 states are visible in the $\Xi_c^+ \pi^-$ system. The inset shows an expanded view of the upper left corner. In order to increase the selection efficiency of the Ω_c^{**0} states, an additional BDT classifier is utilised for the study of the $\Xi_c^+ K^-$ spectrum. All selections made to the data and simulated samples are identical to those described in Section. 5.3. A simulated sample of $\Omega_b^- \to \Xi_c^+ K^- \pi^-$ decays, with an additional requirement of $m(\Xi_c^+ K^-) < 3.3\,\text{GeV}$, is used as the signal input. For the background sample candidates are in the $6200 - 6300\,\text{MeV}$ range of the $\Xi_c^+ K^- \pi^-$ mass distribution. The input variables for the MVA are the same as listed in Table 5.8. As previously, 2012 and 2016 simulation are used for training of the Run 1 and Run 2 MVA classifiers. The ROC and over-training test are shown in Fig. 6.2, the performance of both BDT and BDTG classifiers are similar. To be consistent, the BDT classifier is used to reduce the background candidates in our sample. The over-training check in Fig. 6.2b gives a realistic BDT algorithm

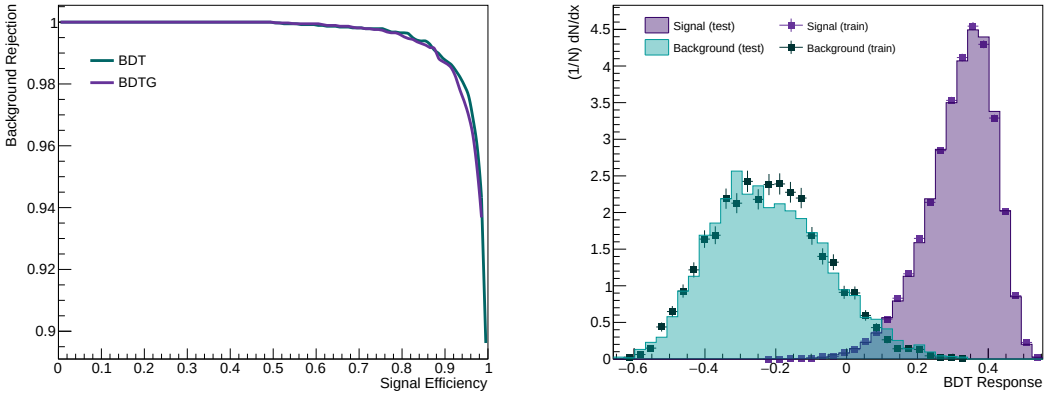

(a) Receiver-operator curve. (b) Over-training check of the BDT output

Figure 6.2 Left is the receiver-operator curve for the BDT and BDTG classifiers (a) and on the right is the over-training check of the BDT output (b).

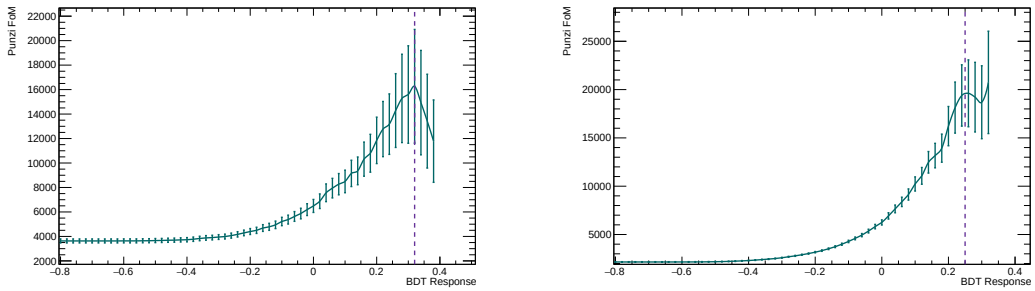

(a) Run 1 (b) Run 2

Figure 6.3 The variation in the figure of merit with BDT response, for the BDT classifier which is trained using an additional selection on the mass of the $\Xi_c^+ K^-$. Run 1 (a) gives an optimal selection on the BDT response of 0.32 and Run 2 (b) gives 0.25. The significance is calculated while the number of background candidates is above 0.

performance and a good separation between signal and background candidates.

The selection on the requirement of the BDT response is optimised using the Punzi figure of merit, where the BDT response against figure of merit is shown in Fig. 6.3. The selection on the BDT response is indicated by the vertical purple dashed line, and is 0.32 and 0.25 for Run 1 and Run 2, respectively. The fluctuations in Fig. 6.3 are due to a low number of background candidates in that region. The resultant $\Xi_c^+ K^- \pi^-$ mass distribution is shown in Fig. 6.4 with the parameters measured by means of an unbinned likelihood fit listed in Table 6.1. The Ω_b^- signal peak is modelled with two Gaussian functions and the feed-down components are modelled using simulated data, as described in Sec. 5.7.

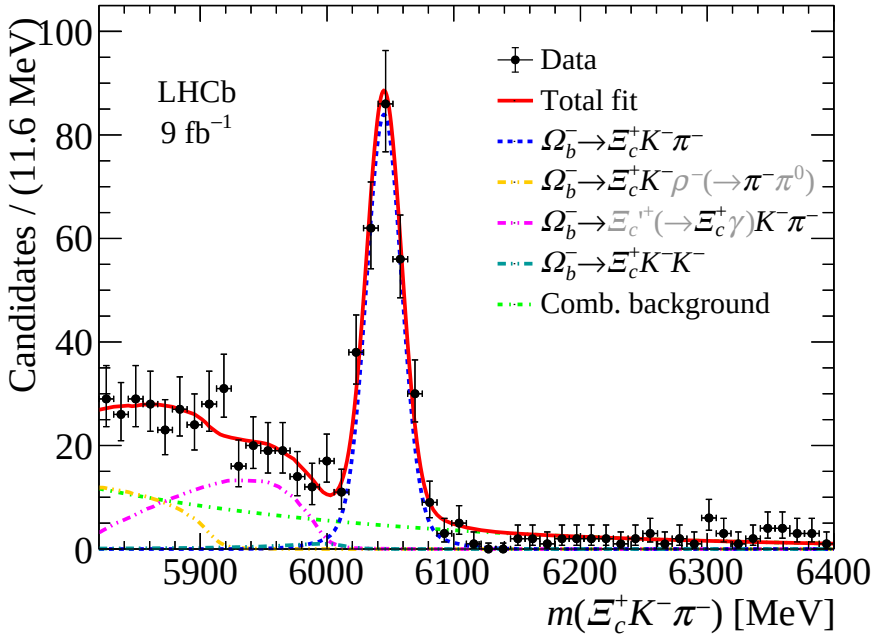

Figure 6.4 Invariant mass distribution of the $\Xi_c^+ K^- \pi^-$ candidates, selected with $m(\Xi_c^+ K^-) < 3.3\,\text{GeV}$. The projections from an unbinned maximum likelihood fit are overlaid, where the total fit is shown in red. The signal component is modelled by the combination of two Gaussian functions indicated by the blue dashed line.

Table 6.1 Parameters determined from the unbinned maximum likelihood fit performed on the $\Xi_c^+ K^- \pi^-$ mass distribution, shown in Fig. 6.4.

Parameter	Run 1 & 2	Run 1	Run 2
σ_1 [MeV]	13.7 ± 0.9	13.1 ± 2.2	13.8 ± 1.0
σ_2 [MeV]	33.4 ± 2.2	31.4 ± 5.3	34.5 ± 2.5
σ [MeV]	17.3 ± 1.1	16.7 ± 2.8	17.4 ± 1.3
$M(\Omega_b^-)$ [MeV]	6045.1 ± 1.1	6043.3 ± 2.5	6045.4 ± 1.2
$N_{\Xi_c^+ K^- \pi^-}$	267.0 ± 18.2	46.5 ± 7.0	220.9 ± 15.0
$N_{\Xi_c^+ K^- \rho^-}$	70.1 ± 17.4	12.1 ± 1.8	57.4 ± 3.9
$N_{\Xi_c'^+ K^- \pi^-}$	148.8 ± 22.9	26.0 ± 3.9	123.7 ± 8.4
$N_{\Xi_c^+ K^- K^-}$	7.5 ± 0.5	1.3 ± 0.2	6.2 ± 0.4
N_{BKG}	219.7 ± 29.0	31.1 ± 10.6	188.0 ± 23.6

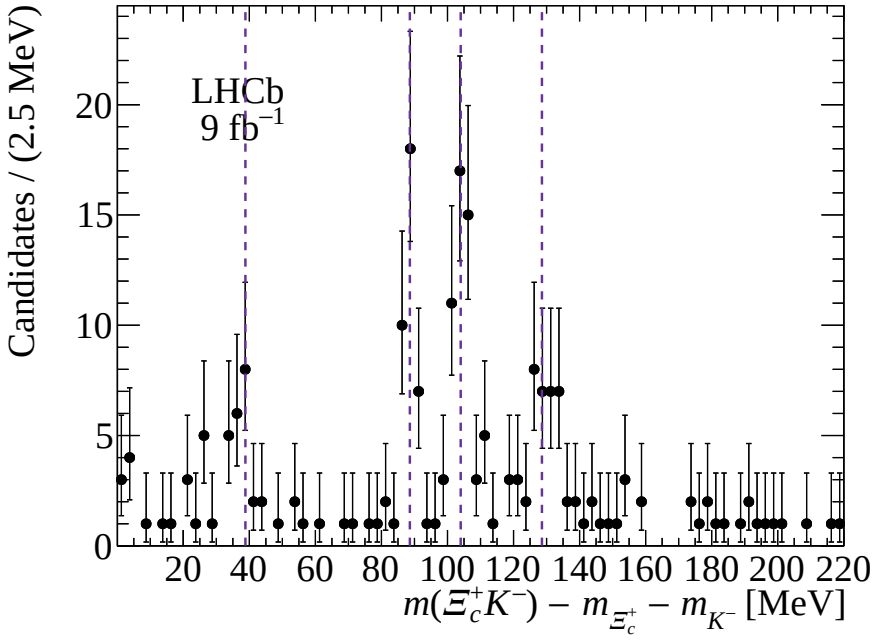

Figure 6.5 Invariant mass distribution of $\Xi_c^+K^-$ candidates after taking a mass region of $\pm 2\sigma$ around the Ω_b^- mass. The vertical lines indicate the masses of the excited Ω_c^0 baryons in the prompt analysis [5].

Note that a higher yield of $\Omega_b^- \to \Xi_c^+K^-\pi^-$ candidates is observed through this selection process compared to the previous process given in Sec. 5.3. In this case the BDT classifier has been trained with the signal sample containing an additional selection on the mass of the $\Xi_c^+K^-$. This increase is most likely due to the majority of the Ω_b^- decays occurring through the excited Ω_c^0 states, making this BDT output more optimised. In addition to the BDT response requirements, an additional selection on the $\Xi_c^+K^-\pi^-$ candidates of $\pm 2\sigma$ around the Ω_b^- mass is used. The projection of the Ω_c^0 states in the $\Xi_c^+K^-$ system is shown in Fig. 6.5, where four peaking structures are observed in proximity of the four states observed in the prompt analysis [5]. The fifth state, $\Omega_c(3119)^0$, has not been observed in the $\Xi_c^+K^-$ mass spectrum.

6.2 Fit model

6.2.1 Signal model

Each of the four resonances in the $\Xi_c^+K^-$ mass spectrum is modelled using a relativistic Breit-Wigner (RBW) function to describe their amplitude, convoluted

with a Gaussian function for the detector resolution. An additional RBW function is used at the threshold region. The RBW function is given by:

$$\mathrm{BW}(s|m_i\Gamma_i) = \frac{\sqrt{m_i\Gamma_i}}{m_i^2 - s - ig_i^2 p^{2l+1}(s)B_l'^2((pR)^2)/\sqrt{s}}, \tag{6.1}$$

where i ranges from 1 to 4 for each of the resonances and g^2 can be expressed in terms of the width parameter Γ_i:

$$g_i^2 = \Gamma_i \frac{m_i}{p^{2l+1}(m_i^2)B_l'((p(m_i^2)R)^2)}, \tag{6.2}$$

and

$$p(s) = \frac{\lambda^{1/2}(s, m^2_{\Xi_c^+}, m^2_{K^-})}{2\sqrt{s}}. \tag{6.3}$$

The standard Blatt-Weisskopf factors for B_l' are used:

$$B_0'(z) = 1, \quad B_1'(z) = 1/(1+z^2), \quad B_2'(z) = 1/(9+3z^2+z^4), \tag{6.4}$$

where z is pR in Eq. 6.1. The invariant mass squared of the $\Xi_c^+ K^-$ system is s, where $s \equiv m^2_{\Xi_c^+ K^-}$, and $\lambda(x,y,z) = x^2+y^2+z^2-2xy-2yz-2zx$ is the Källén function. For the default fit the angular momentum, l, is set to 0. Other values are tested in the systematic studies. The peak of the threshold structure could be below zero, to account for this possibility the coupling, g, is used as a fit parameter instead of the width, Γ. The amplitude from the RBW function is squared and multiplied by the three-body phase-space factors $p(s)q(s)/\sqrt{s}$. This is given by:

$$S_i(s|m,\Gamma) = p(s)q(s)|BW(s|m_i,\Gamma_i)|^2, \tag{6.5}$$

where the q factor is a break-up momentum in a system of $\Xi_c^+ K^-$ candidates with the mass $\sqrt{s}$ and a π^- spectator, given by:

$$q(s) = \frac{\lambda^{1/2}(m^2_{\Omega_b^-}, m^2_{\pi^-}, s)}{2m_{\Omega_b^-}} \tag{6.6}$$

The line-shape functions (given by Eq. 6.5) are convoluted with a Gaussian function to describe the experimental resolution:

$$S_i^{conv}(s) = Gauss(s|\sigma_i) \otimes S_i(s|m_i, \Gamma_i). \tag{6.7}$$

The resolution of each Gaussian function is fixed through a study of the simulation, described in the following section. A model with an energy-dependent resolution function gives the same result.

Resolution of the Ω_c^{**0} resonances

To determine the mass resolution as a function of the $\Xi_c^+ K^-$ mass, the simulated sample of $\Omega_b^- \to \Xi_c^+ K^- \pi^-$ candidates is used. The $\Xi_c^+ K^-$ mass range is divided up into six segments, for each segment the mass resolution is calculated by modelling the difference between the generated and reconstructed $\Xi_c^+ K^-$ mass. This difference is defined as:

$$\delta m(\Xi_c^+ K^-) = m_{\mathrm{Kin}}(\Xi_c^+ K^-) - m_{\mathrm{TRUE}}(\Xi_c^+ K^-), \tag{6.8}$$

where $m_{\mathrm{Kin}}(\Xi_c^+ K^-)$ is the invariant mass with a kinematic fit applied to improve mass resolution, where a constraint requiring the Ξ_c^+ and K^- candidates to originate from their associated primary vertex (PV) is applied and m_{TRUE} is the value of the invariant mass when the Ξ_c^+ and K^- masses are used as an input in the simulation. Each peak is modelled by two Gaussian functions with a shared mean, shown in Fig. 6.6. The mass given for each of the sub-figures are the central values in a range of $\pm 0.8\,\mathrm{MeV}/c^2$. Table 6.2 lists the parameters of the fit, including the width and the mean.

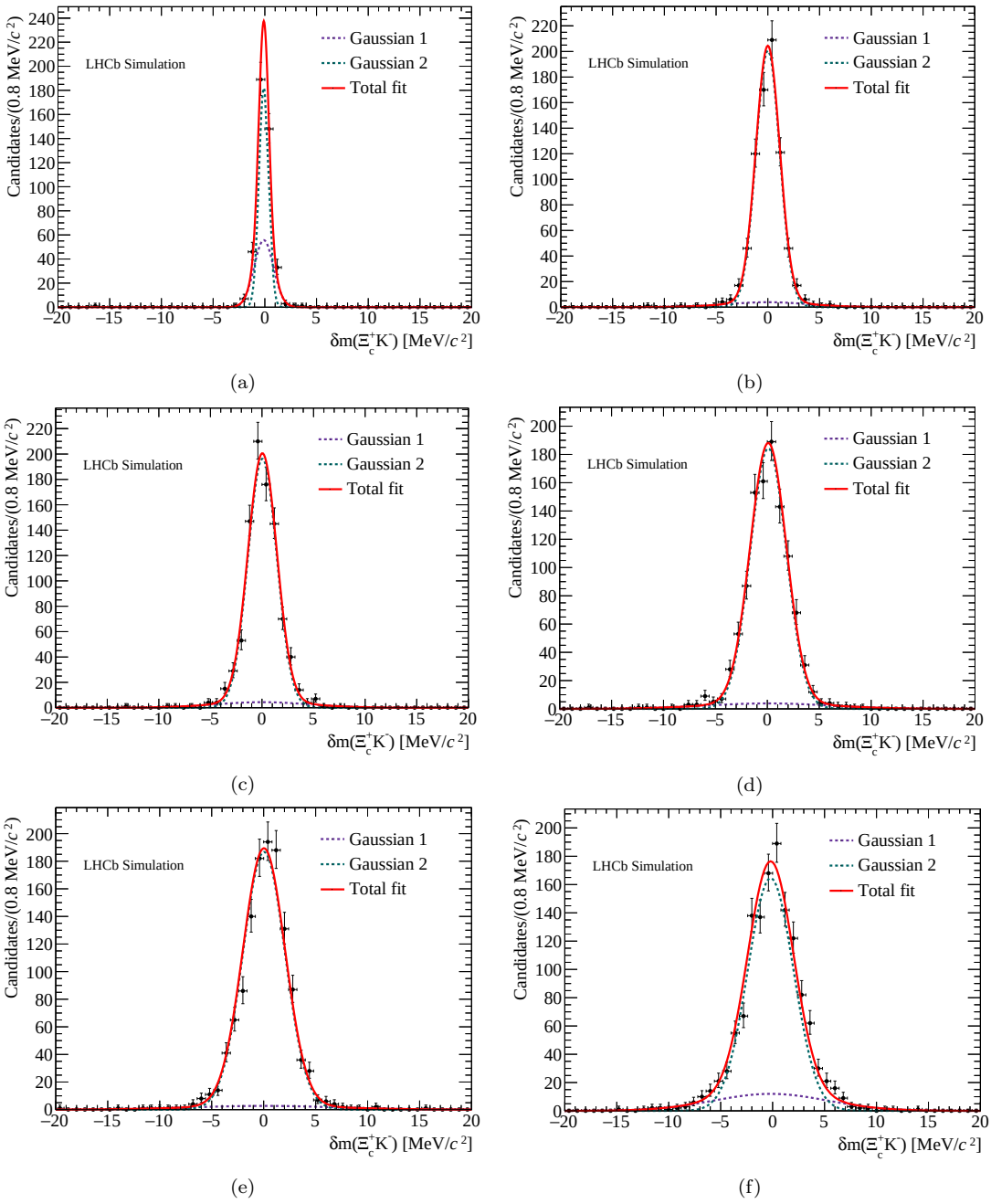

Figure 6.6 Mass distributions for different simulated $\Xi_c^+ K^-$ masses using the combined sample of 2012 and 2016 MC: (a) corresponds to $m(\Xi_c^+ K^-) = 2985$ MeV/c^2, (b) is $m(\Xi_c^+ K^-) = 3040$ MeV/c^2, (c) is $m(\Xi_c^+ K^-) = 3080$ MeV/c^2, (d) is $m(\Xi_c^+ K^-) = 3120$ MeV/c^2, (e) is $m(\Xi_c^+ K^-) = 3160$ MeV/c^2, and (f) corresponds to $m(\Xi_c^+ K^-) = 3210$ MeV/c^2.

Table 6.2 Mean and resolutions of each double Gaussian function shown in Fig. 6.6. The resolution, σ, is the combined resolution of the two Gaussian functions.

Mass [MeV/c^2]	Mean ($\delta M_{\Omega_c^{**}}$)	σ_1 [MeV]	σ_2 [MeV]	σ [MeV]	f_1
2985	-0.10 ± 0.03	0.93 ± 0.12	0.47 ± 0.06	0.67 ± 0.07	0.36
3040	0.00 ± 0.05	3.96 ± 0.49	1.15 ± 0.05	1.64 ± 0.12	0.10
3080	0.04 ± 0.05	4.60 ± 0.52	1.40 ± 0.06	1.99 ± 0.13	0.10
3120	0.09 ± 0.06	6.08 ± 0.74	1.74 ± 0.05	2.36 ± 0.15	0.07
3160	0.03 ± 0.07	7.07 ± 0.86	2.03 ± 0.07	2.90 ± 0.20	0.09
3210	-0.19 ± 0.07	5.46 ± 0.43	2.20 ± 0.09	3.11 ± 0.15	0.19

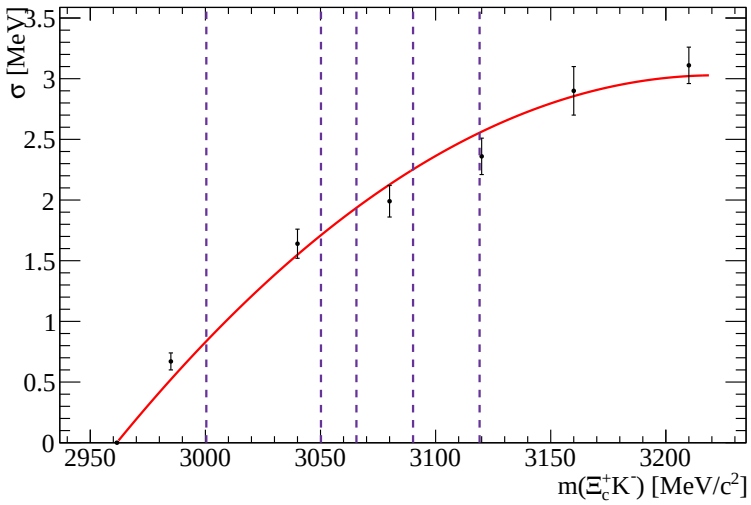

Figure 6.7 Polynomial fit to the resolution as a function of the $\Xi_c^+ K^-$ invariant mass, shown in red. The purple dashed vertical lines correspond to the masses of the resonances found in the prompt analysis [5].

The resolution as a function of mass can be seen in Fig. 6.7, where the distribution is modelled by a second order polynomial given by:

$$\sigma(m) = p_1 m + p_2 m^2, \tag{6.9}$$

where p_1 and p_2 are determined to be $p_1 = 23.2$ and $p_2 = -44.6$.

The resolution is constrained to go through zero at the value at the $\Xi_c^+ K^-$ kinematic threshold, $m_{thr} = m(\Xi_c^+) + m(K^-) = 2961.6$ MeV/c^2. Using the second order polynomial fit to the distribution shown in Fig. 6.7 it is possible to determine the resolution of each Ω_c^{**0} resonance in simulation, the values used in the default fit model are listed in Table 6.3.

Table 6.3 Resolution of each Ω_c^{**0} resonance, obtained from the polynomial fit to Fig. 6.7.

Resolution	$\Omega_c(3000)^0$	$\Omega_c(3050)^0$	$\Omega_c(3065)^0$	$\Omega_c(3090)^0$	$\Omega_c(3119)^0$
σ	0.8 MeV	1.7 MeV	1.95 MeV	2.25 MeV	2.36 MeV

Table 6.4 Parameters for the two sources of background in our sample modelled according to Equation 6.10.

Source	α	β [MeV^{-1}]
Non-resonant	0.492 ± 0.013	$(0.30 \pm 0.15) \times 10^{-3}$
Combinatorial	0.469 ± 0.133	$(2.91 \pm 1.67) \times 10^{-3}$

6.2.2 Background shape

The two major background sources in the selected sample of $\Xi_c^+ K^-$ candidates are combinatorial and non-resonant $\Xi_c^+ K^-$ contributions. The second component is needed in order to correctly describe possible non-resonant and broad resonant states of $\Xi_c^+ K^-$. Both of these can be parameterised by the following function:

$$f(\Delta M) = (\Delta M)^{\alpha} \times e^{-\beta \Delta M}, \tag{6.10}$$

where

$$\Delta M = m(\Xi_c^+ K^-) - m_{\Xi_c^+} - m_{K^-}. \tag{6.11}$$

In the above equations, $m(\Xi_c^+ K^-)$ is the invariant mass of the $\Xi_c^+ K^-$ system, and α and β are parameters which are determined by two fits. The shape of the combinatorial background is modelled using the $\Xi_c^+ K^-$ mass distribution in the Ω_b^- side-band, shown in Fig. 6.8 with the fit parameters listed in Table 6.4.

For the non-resonant background the phase space distribution is used. Possible efficiency effects on the background shape are taken into account by modelling the simulated phase space sample. This is shown in Fig. 6.9 with the fit parameters listed in Table 6.4.

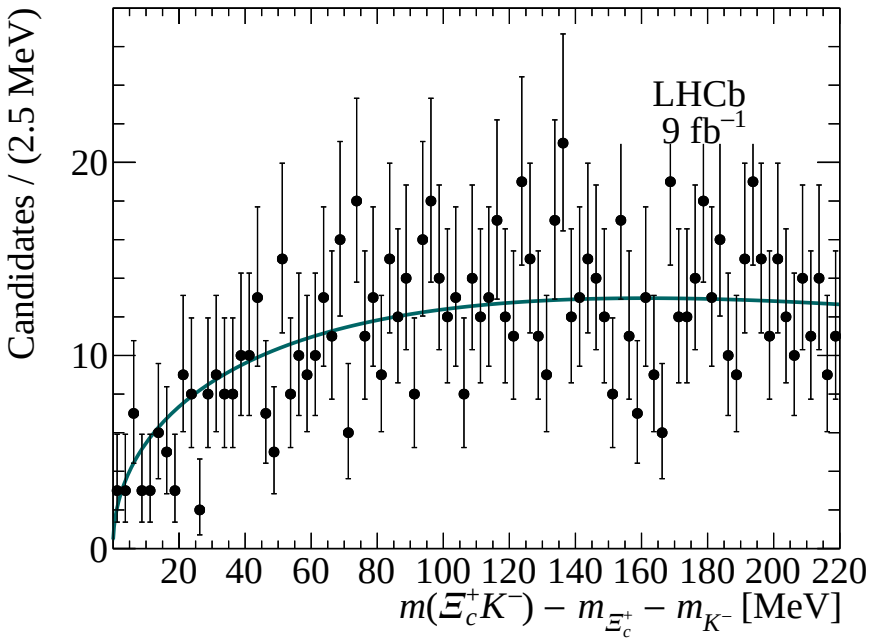

Figure 6.8 The $\Xi_c^+ K^-$ invariant mass spectrum in the Ω_b^- side-band in the range $6100 - 6400$ MeV. The mass is expressed in terms of ΔM, defined in Eq. 6.11.

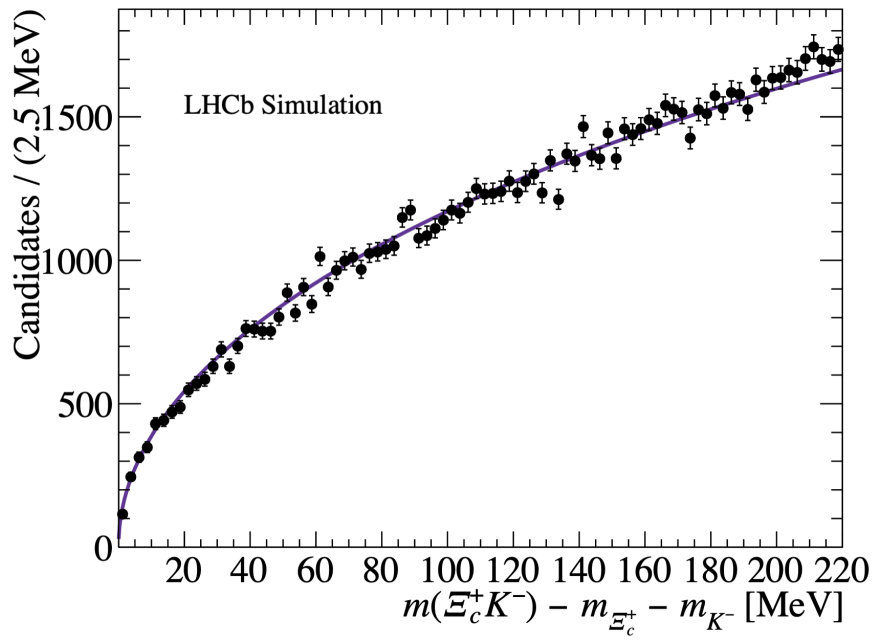

Figure 6.9 The $\Xi_c^+ K^-$ invariant mass spectrum in simulation. The mass is expressed in terms of ΔM, defined in Eq. 6.11.

Table 6.5 Parameters determined from the fit performed to the $\Xi_c^+ K^-$ mass distribution in Fig. 6.10. The results from the prompt analysis are shown in the second and third column [5].

	Prompt analysis		Default model		
Resonance	Mass [MeV]	Γ [MeV]	Mass [MeV]	Γ [MeV]	Yield
$\Omega_c(3000)^0$	3000.4 ± 0.2	4.5 ± 0.6	2999.2 ± 0.9	4.8 ± 2.1	23.8 ± 7.2
$\Omega_c(3050)^0$	3050.2 ± 0.1	0.8 ± 0.2	3050.1 ± 0.3	< 1.0 CL 90%	33.1 ± 6.0
$\Omega_c(3065)^0$	3065.6 ± 0.1	3.5 ± 0.4	3065.9 ± 0.4	1.7 ± 1.0	50.8 ± 8.3
$\Omega_c(3090)^0$	3090.2 ± 0.3	8.7 ± 1.0	3091.0 ± 1.1	7.4 ± 3.1	41.4 ± 9.1

6.2.3 Default $\Xi_c^+ K^-$ mass fit

Combining all the previously described components gives the complete fit function, which is given by:

$$W(s) = \sum_{i=0}^{4} c_i S_i^{conv}(s) + c_5 f_{comb} + c_6 f_{phsp}, \tag{6.12}$$

where c_i is the normalisation parameters for $i = 1, ..., 4$, f_{comb} is the combinatorial background and f_{phsp} is the non-resonant background (phase-space). The component with $i = 0$ is the RBW function which describes the excess of candidates in the threshold region. Three separate fits have been performed to the $\Xi_c^+ K^-$ mass distribution:

1. Mass, width and yield of each RBW function are allowed to vary in the fit.
2. Mass and yield allowed to vary in the fit, the widths are Gaussian constrained.
3. Yield is allowed to vary in the fit, the decay widths are Gaussian constrained and the mass is fixed according to the results found in the prompt analysis.

Figure. 6.10 shows the maximum likelihood fit to the $\Xi_c^+ K^-$ mass distribution with the mass, width and yield of each RBW function is allowed to vary in the fit. The parameters determined from the fit are listed in Table 6.5, along with the results from the prompt analysis [5] to allow for an easy comparison. The results on the masses and widths of each resonance are consistent to within 3σ of the promptly produced Ω_c^{**0} candidates.

Previously, a fifth state of the Ω_c^{**0} baryon at a mass of 3119 MeV ($\Omega_c(3119)^0$) was seen, this is missing in the $\Xi_c^+ K^-$ mass distribution. This is consistent with the preliminary result from an inclusive sample of semi-leptonic Ω_b^- decays. This could

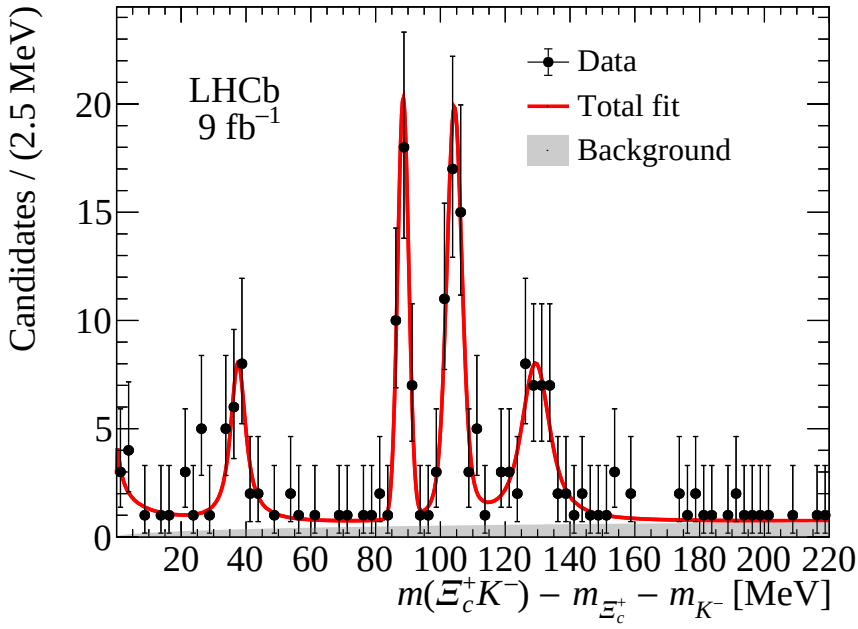

Figure 6.10 Extended unbinned maximum likelihood fit to the $\Xi_c^+K^-$ mass distribution where each resonance is modelled by a Gaussian function convoluted with a relativistic Breit-Wigner. The background is modelled by the simulated phase-space and the Ω_b^- background. The mass, width and yield of each resonance is allowed to float.

be due to a low number of events or a suppression in the production of Ω_b^- decays due to large differences in angular momentum. The width of the second peak is consistent with zero and therefore cannot be determined from the fit. An upper limit is set based on the likelihood profile [89]. The confidence limit of 90%(95%) obtained from the change in the likelihood equal to $\Delta\text{NLL} = 1.352(1.921)$ is shown in Fig. 6.11. To determine the change in likelihood corresponding to a confidence level of 90%(95%) a threshold is established on the null hypothesis such that the integral from 0 to the threshold is 0.9(0.95). The null hypothesis is that the decay width, Γ, is zero. This gives an upper limit of:

$$\Gamma_2 < 1.0 \text{ MeV } (1.3 \text{ MeV}) \text{ CL } 90\%(95\%) \tag{6.13}$$

6.2.4 Fits with constraints

Constrained fits are needed in order to perform an analysis of the spin of the Ω_c^{**0} states and the estimation of the signal significance. The first fit is performed with a Gaussian constraint on the widths of each state, where a Gaussian constraint is

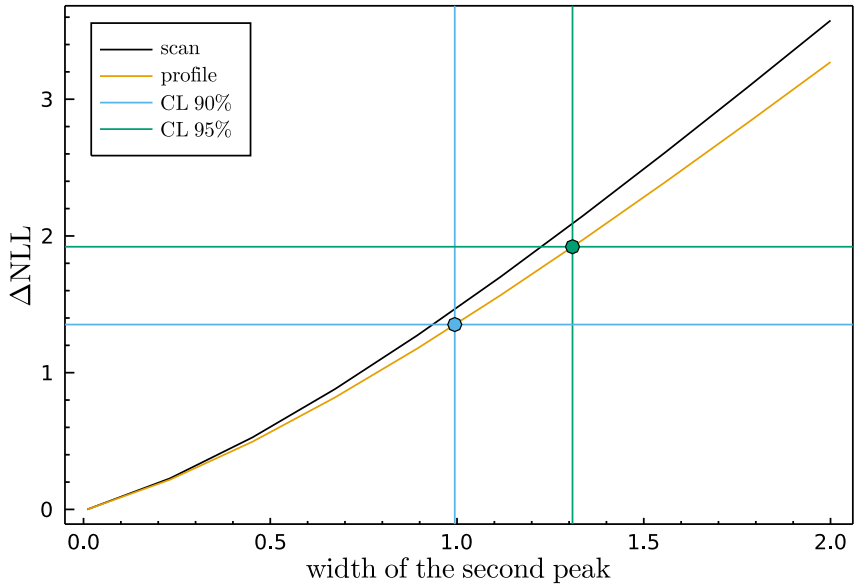

Figure 6.11 Likelihood profile for the width of the second resonance, Γ_2. The horizontal lines indicate the change in the likelihood that correspond to a 90% and 95% confidence level.

Table 6.6 Parameters found from the extended maximum likelihood fits in Fig. 6.12.

	Width constrained			Mass fixed	
Resonance	Mass [MeV]	Γ [MeV]	Yield	Γ [MeV]	Yield
$\Omega_c(3000)^0$	2999.2 ± 0.9	4.5 ± 0.6	24.0 ± 6.3	4.5 ± 0.6	23.2 ± 6.1
$\Omega_c(3050)^0$	3050.1 ± 0.4	0.7 ± 0.2	34.7 ± 6.3	0.7 ± 0.2	34.5 ± 6.3
$\Omega_c(3065)^0$	3066.0 ± 0.5	3.3 ± 0.4	54.0 ± 8.2	3.3 ± 0.4	53.3 ± 8.1
$\Omega_c(3090)^0$	3091.2 ± 1.1	8.5 ± 1.0	41.9 ± 8.1	8.6 ± 1.0	42.1 ± 8.1

one which has a central value with an uncertainty that it can vary through. The second has the Gaussian constrained widths and the masses fixed to the previous results (shown in Table 6.5). The result of the unbinned maximum likelihood fit is shown in Fig. 6.12, with the parameters listed in Table 6.6.

6.3 Significance of the Ω_c^{**0} states

The significance of each Ω_c^{**0} state is calculated through the difference in negative log likelihoods between the default fit and a fit with one of the components removed. Only one component is removed at a time in order to determine the significance of that peak. The masses and widths are fixed to those found in the default model, while the yields are allowed to vary. The alternative models with

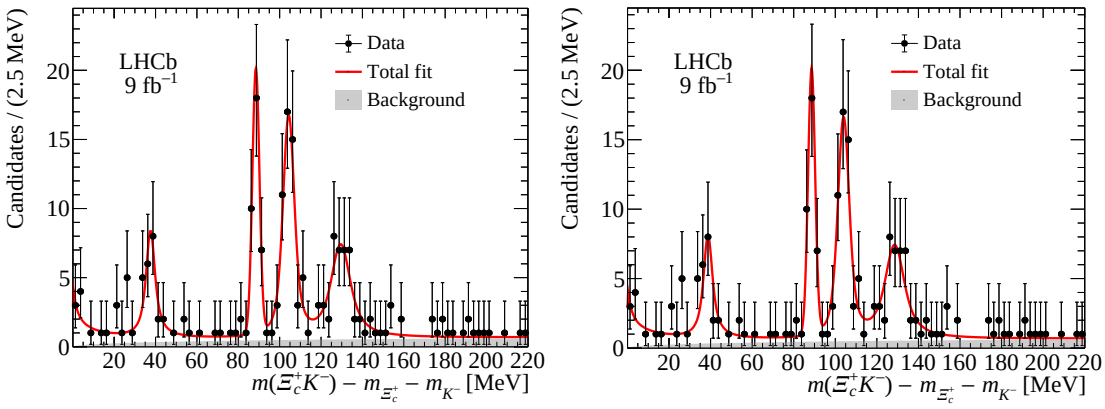

(a) (b)

Figure 6.12 Extended unbinned maximum likelihood fit to the $\Xi_c^+ K^-$ mass distribution. The widths are Gaussian constrained to the values found in the prompt analysis in (a) and (b), and the masses are fixed in (b).

Table 6.7 Significance of each component, determined by the difference in log likelihood values in the fit.

	Threshold	$\Omega_c(3000)^0$	$\Omega_c(3050)^0$	$\Omega_c(3065)^0$	$\Omega_c(3090)^0$	$\Omega_c(3119)^0$
ΔNLL	17.9	20.9	61.0	75.5	31.9	0.03
Significance	6.0σ	6.5σ	11.0σ	12.3σ	8.0σ	—

one signal removed are shown in Fig. 6.13, with the values of the significance listed in Table 6.7.

The statistical significance of all of the four main peaks is found to be over 6σ. A more detailed and accurate study of the threshold enhancement and fifth peak are discussed in the following section.

6.4 Additional structures

Here, two modifications to the default fit model are considered:

1. Testing different fit hypotheses for the threshold enhancement and evaluate the significance.

2. Adding a fifth peaking structure.

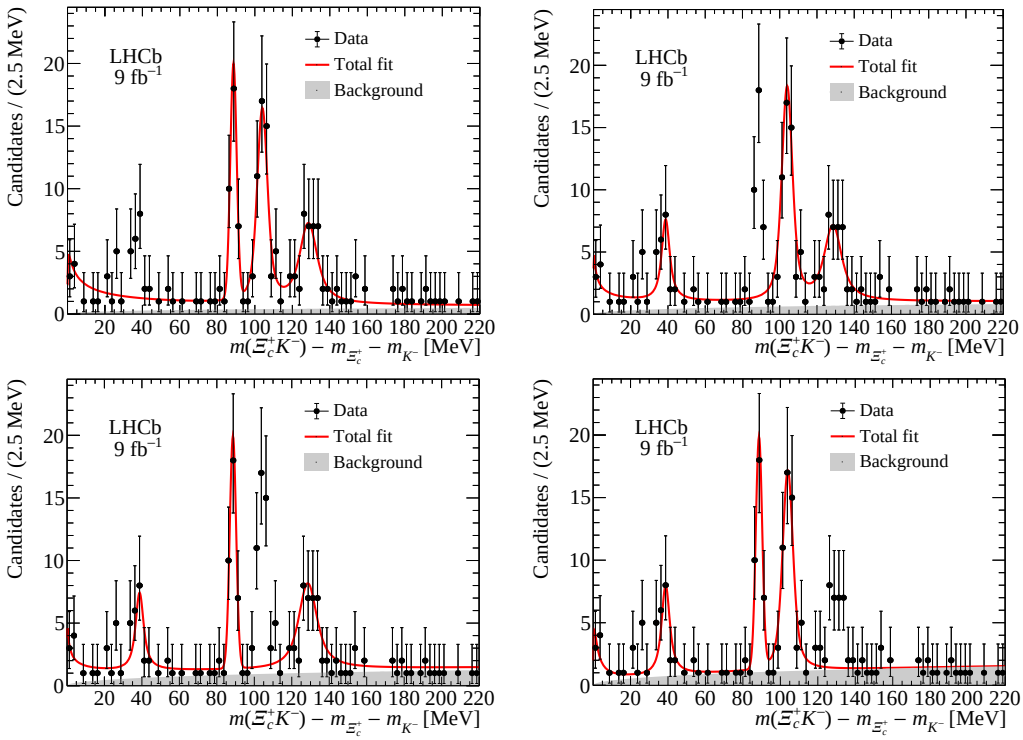

Figure 6.13 For the estimation of significance. Each figure has one component removed to determine the difference in log likelihood compared to the default model.

6.4.1 Threshold peak

In the threshold region of the $\Xi_c^+K^-$ invariant mass distribution, shown in Fig. 6.10, there is a large deviation where we would expect the background to tend to zero. In the prompt analysis an enhancement was seen at the threshold region, but it was interpreted as a partially reconstructed decay. This explanation has been ruled out in this analysis due to the selection made on the Ω_b^- mass. There are also additional concerns about the large yield of the partially reconstructed decay in the prompt analysis [5]. The decay of $\Omega_c(3065)^0 \to \Xi_c^{\prime+}K^-$ was considered as the mass of the $\Omega_c(3065)^0$ is slightly below the $\Xi_c^{\prime+}K^-$ threshold:

$$m(\Xi_c^{\prime+}) - m(\Xi_c^+) = 110 \pm 0.4 \text{ MeV}, \tag{6.14}$$

where the $\Omega_c(3065)^0$ is at a mass of:

$$m(\Omega_c(3065)^0) - m(\Xi_c^+) - m(K^-) = 104.1 \pm 0.1 \pm 0.3 \text{ MeV}. \tag{6.15}$$

The decay width of the $\Omega_c(3065)^0$ state from the prompt analysis is:

$$\Gamma(\Omega_c(3065)^0) = 3.5 \pm 0.4 \pm 0.2 \text{ MeV}, \tag{6.16}$$

indicating that the mass of the $\Omega_c(3065)^0$ resonance is two decay widths, $\Gamma(\Omega_c(3065)^0)$, away from the $\Xi_c^{\prime +} K^-$ threshold. It can leak into our mass spectrum, however, it should be heavily suppressed by the phase-space factors. Despite this, its fraction found from the fit to the prompt $\Xi_c^+ K^-$ mass distribution is around half of the $\Omega_c(3065)^0$ component,

$$\frac{N_{fd}(\Omega_c(3065)^0)}{N(\Omega_c(3065)^0)} = \frac{700 \pm 40 \pm 140}{1740 \pm 100 \pm 50} = 0.402 \pm 0.085, \tag{6.17}$$

which would demand the $\Omega_c(3065)^0$ state being coupled to the $\Xi_c^{\prime +}$ an order of magnitude stronger than to the Ξ_c^+ baryon, making this seem unlikely. Three models are tested on the threshold enhancement:

1. The relativistic Breit-Wigner function in the form given by Eq. 6.1
2. Using the scattering-length approximation (SLA):

$$S_0(s) = \frac{p(s)q(s)}{|-a_0 - i\rho(s)|^2} \tag{6.18}$$

   where a_0 is a dimensionless parameter proportional to the scattering length [6]. In the model, the pole which corresponds to the threshold state is located below the threshold. A real value of a_0 implies a bound state, while an imaginary one indicates a virtual one.

3. Simple-pole model (RBW with constant width).

The experimental resolution effects are neglected. For convenience the fit range is restricted to $0 < m(\Xi_c^+ K^-) < 80$ MeV, this includes the region with the peak at $\Omega_c(3000)^0$ and the background up to the $\Omega_c(3050)^0$ state. The results of the three models are shown in Fig. 6.14.

The significance of the background rejection is estimated using the RBW model shown in Fig. 6.14a. The difference of the negative log likelihoods for the fit with the threshold structure (s+b) and without (b), is used as the test statistic. The

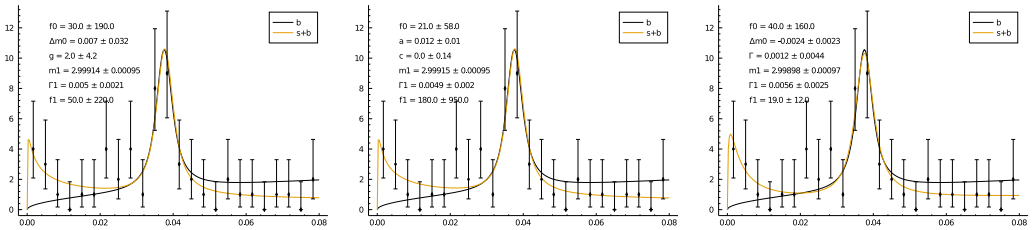

(a) BW model (b) SLA model (c) A simple pole model

Figure 6.14 Three models to the $\Xi_c^+ K^-$ mass distribution with the threshold component. The RBW model, scattering-length approximation model and a simple pole model are used for the left, middle and right figures, respectively.

p-value is calculated using:

$$p = \int_{NLL}^{\infty} \chi^2(x,k)dx, \tag{6.19}$$

where $\chi^2(x,k)$ is the standard χ^2 distribution with k being the difference in the number of parameters between the two fits, background (b) and signal plus background (s+b). For $k = 3$ a significance of $n_\sigma = 5.3\sigma$ for the full range and $n_\sigma = 4.6\sigma$ for the smaller range are found. A set a pseudo-experiments is run to validate the selected value of k. Event samples are generated according to the default model from the signal plus background model shown in Fig. 6.14a, where the yield of the threshold component is set to zero. Then it is described by the s+b model (6 parameters) and the background model (3 parameters). Due to the s+b model searching for narrow structures close to the threshold, the mass and couplings are in a limited range:

$$-5 < \Delta m < 10 \text{ MeV},$$
$$0.5 < g < 2 \text{ MeV}.$$

Examples of different line-shapes with parameters in the restricted range given above are shown in Fig. 6.15a. The distribution of the negative log likelihood is shown in Fig. 6.15b. Modelling the tail of the distribution gives the effective number of degrees of freedom, equal to $N_{eff} = 2.61 \pm 0.24$. The value used is $k = 3$ which seems to be a reasonable conservative estimation.

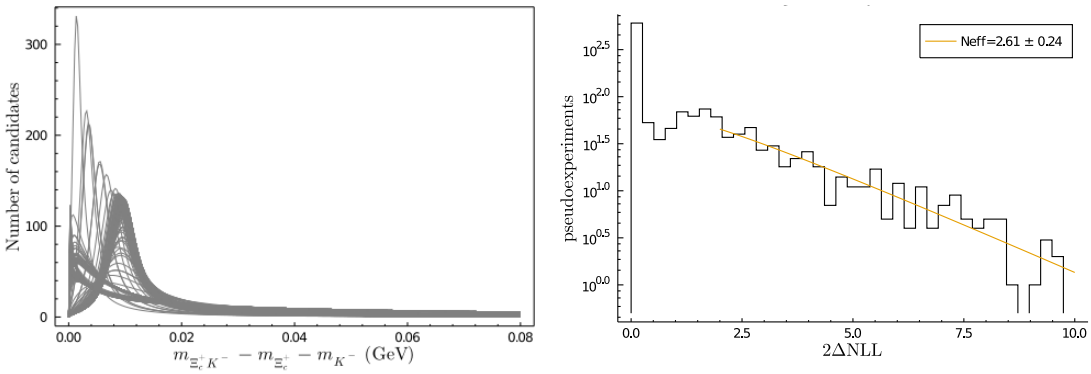

(a) (b)

Figure 6.15 (a): Examples of the line shape of the threshold structure. The parameters Δm_0 and g are randomly sampled in the fit range. (b): Distribution of the negative log-likelihood with 2400 pseudo-experiments. The generated data is sampled from the background-only distribution and fit by $s+b$ and b models. The orange line shows the result of the likelihood fit by the $\chi^2(x, N_{\text{eff}})$ distribution with N_{eff} degrees of freedom.

6.4.2 Fifth peak

Five Ω_c^{**0} resonances were observed in the $\Xi_c^+ K^-$ mass distribution in the prompt analysis. The fifth peak, named $\Omega_c(3119)^0$, cannot be seen in the non-prompt production of the Ω_c^0 baryon. This could be due to a suppression from a possible large difference in angular momentum between the Ω_b^- baryon and the $\Omega_c(3119)^0$ state. A relativistic Breit-Wigner component with the mass and width fixed to the parameters of the $\Omega_c(3119)^0$ state from the prompt analysis is added to our default fit model. This is shown in Fig. 6.16a, alongside the profile likelihood in Fig. 6.16b. The yield is found to be $N_{\Omega_c(3119)^0} = 0.5 \pm 2.5$ candidates, and the improvement to the likelihood value is negligible, $\Delta\text{NLL} = 0.03$. The upper limit is set by exploring the profile likelihood:

$$N_{\Omega_c(3119)^0} < 4.9(6.1), \text{ at } 90\%(95\%) \text{ CL.} \tag{6.20}$$

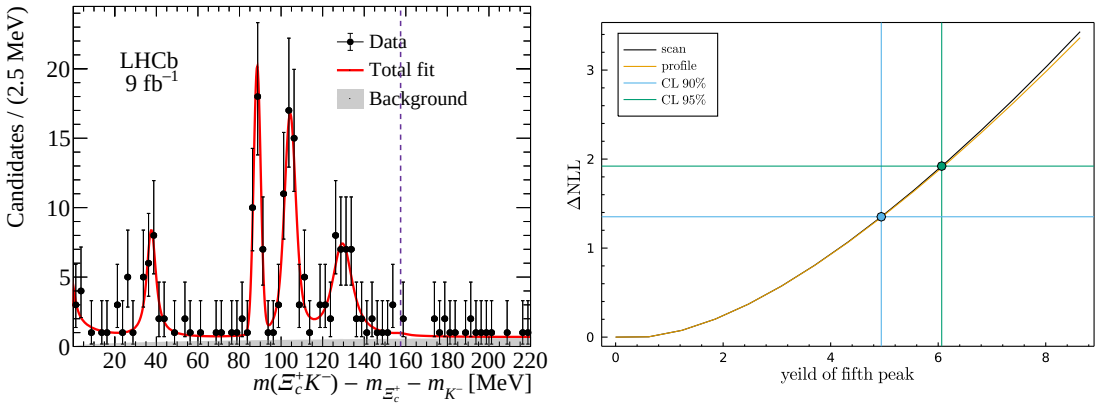

(a) (b)

Figure 6.16 (a): Fit to the $\Xi_c^+K^-$ mass distribution including the 5$^{\text{th}}$ peak $\Omega_c(3119)^0$, where the parameters are fixed according to the prompt analysis. (b): Shows the likelihood profile for the yield of the fifth state, $N_{\Omega_c(3119)^0}$. The horizontal lines indicate the change in likelihood that corresponds to 90% and 95% CL.

6.5 Fraction of excited Ω_c^0 baryons in $\Omega_b^- \to \Omega_c^{**0}\pi^-$

The fraction of Ω_c^{**0} states found in $\Omega_b^- \to \Xi_c^+K^-\pi^-$ decays is denoted as B_i/B_0 throughout this section, where $i = 1, ..., 4$ for the four observed peaking structures. The ratio gives the product of the production and the decay amplitudes, and is determined as follows:

$$\frac{B_i}{B_0} = \frac{\mathcal{B}(\Omega_b^- \to \Omega_c^{**0}\pi^-)\mathcal{B}(\Omega_c^{**0} \to \Xi_c^+K^-)}{\mathcal{B}(\Omega_b^- \to \Xi_c^+K^-\pi^-)} = N^{corr}_{\Omega_c^{**0}\pi^-}/N^{corr}_{\Xi_c^+K^-\pi^-}, \tag{6.21}$$

where $N^{corr}_{\Omega_c^{**0}\pi^-}$ and $N^{corr}_{\Xi_c^+K^-\pi^-}$ are the efficiency corrected yields. The corrections to the $\Xi_c^+K^-\pi^-$ sample are computed using Eq. (5.10), using the simulated sample which covers the entire phase-space. For the $\Omega_c^{**0}\pi^-$ candidates a more refined efficiency map is available, constructed using a large sample of simulated events at the corner of the phase-space, where $m(\Xi_c^+K^-) < 3.3\,\text{GeV}$.

$$N^{corr}_{\Omega_c^{**0}\pi^-} = N^{rec}_{\Omega_c^{**0}\pi^-} \underbrace{\frac{\int I_{\Omega_c^{**0}}(\tau)/\epsilon(\tau)d\tau}{\int I_{\Omega_c^{**0}}(\tau)d\tau} \cdot \frac{\int_\Delta \epsilon(\tau)d\tau}{\int_\Delta d\tau}}_{X_{\Omega_c^{**0}}} \cdot \underbrace{\frac{\int_\Delta d\tau}{\int_\Delta \epsilon'(\tau)d\tau}}_{1/Y}, \tag{6.22}$$

Table 6.8 Calculation for production fraction of Ω_c^{**0} states in Ω_b^- decays. See Eq. (6.22) for definitions of the observables. The value of N_0 is $N_0 = N(\Omega_b^- \to \Xi_c^+ K^- \pi^-) = 217.4 \pm 15.8$. The uncertainty on N_i/N_0 are calculated using the binomial approximation.

Resonance	N_i	$X^{\Omega_c^{**0}}_{Run1}$	$X^{\Omega_c^{**0}}_{Run2}$	N/N_0	B/B_0
$\Omega_c(3000)^0$	23.8 ± 7.2	0.97	1.00	0.11 ± 0.02	0.11 ± 0.02
$\Omega_c(3050)^0$	33.1 ± 6.0	0.97	1.00	0.15 ± 0.02	0.15 ± 0.02
$\Omega_c(3065)^0$	50.8 ± 8.3	0.98	1.01	0.23 ± 0.02	0.23 ± 0.02
$\Omega_c(3090)^0$	41.4 ± 9.1	0.98	1.01	0.19 ± 0.02	0.19 ± 0.02
$\Omega_c(3119)^0$	$< 4.9(6.1)$	–	–	$< 0.02(0.03)$	$< 0.02(0.03)$

where $d\tau$ is the integral on the $\Xi_c^+ K^- \pi^-$ Dalitz plot, and $I_{\Omega_c^{**0}}(\tau)$ is the intensity distribution of Ω_c^{**0} candidates used to weight the simulation. The continuous efficiency map, $\epsilon(\tau)$, does not have an absolute normalisation, so it is scaled according to the efficiency of the Dalitz plot corner obtained from the full simulated sample (factor Y in Eq. (6.22)). The values of Y are determined by the ratio of reconstructed and generated candidates at the corner of the full Dalitz simulation. These can be compared with the averaged efficiencies found in Table. 5.16:

$$\begin{aligned} Y_{\text{Run 1}} &= 0.69\,\%, & Y_{\text{Run 2}} &= 1.37\,\%, \\ \bar{\epsilon}_{\text{Run 1}} &= 0.69\,\%, & \bar{\epsilon}_{\text{Run 2}} &= 1.37\,\%, \end{aligned}$$

The ratio is split between Run 1 and Run 2, in order to incorporate both runs into the calculation a fraction of $f_1 = 1/6$ is used for the number of Run 1 candidates compared to Run 2, found from comparing Run 1 and Run 2 Ω_c^{**0} candidates. The complete expression is given by:

$$\frac{B_i}{B_0} = \frac{N_i}{N_0} \frac{f_1 X^i_{\text{Run 1}}/Y_{\text{Run 1}} + (1-f_1) X^i_{\text{Run 2}}/Y_{\text{Run 2}}}{f_1/\bar{\epsilon}_{\text{Run 1}} + (1-f_1)/\bar{\epsilon}_{\text{Run 2}}}. \tag{6.23}$$

The results are summarised in Table 6.8, the efficiency factor is found to equal one.

6.6 Determination of the Ω_c^{**0} spin

The intensity along the Ω_c^{**0} resonance bands in the $\Omega_b^- \to \Xi_c^+ K^- \pi^-$ Dalitz plot are sensitive to the Ω_c^{**0} spin. This is convenient to express as the helicity angle in the Ω_c^{**0} rest frame. The expression for the angle is [90]:

$$\cos\theta = \frac{2s_3(s_2 - \mathrm{m}^2_{\Xi_c^+} - \mathrm{m}^2_{\pi^-}) - (s_3 + \mathrm{m}^2_{\Xi_c^+} - \mathrm{m}^2_{K^-})(\mathrm{m}^2_{\Omega_b^-} - s_3 - \mathrm{m}^2_{\pi^-})}{\lambda^{1/2}(s_3, \mathrm{m}^2_{\Xi_c^+}, \mathrm{m}^2_{K^-})\lambda^{1/2}(\mathrm{m}^2_{\Omega_b^-}, s_3, \mathrm{m}^2_{\pi^-})} \quad (6.24)$$

where $s_3 = m^2_{\Xi_c^+ K^-}$ and $s_2 = m^2_{\Xi_c^+ \pi^-}$. Determining the spin of each state is done by comparing the likelihood difference of various different hypotheses. The default model of the angular distributions has three components: signal, and the combinatorial and non-resonant Ω_c^{**0} backgrounds. A summary of the spin analysis steps is given below.

1. Fit $\Xi_c^+ K^- \pi^-$ invariant mass spectrum,
   (a) Take candidates that are within $\pm 2\sigma$ around the signal peak,
   (b) Estimate combinatorial background.
2. Model distributions for the combinatorial background,
   (a) Fit the $\Xi_c^+ K^-$ invariant mass spectrum,
   (b) Fit the $\cos\theta$ distribution.
3. Fit the $\Xi_c^+ K^-$ mass distribution for the signal sample,
   (a) Determine the signal ranges for the Ω_c^{**0} resonances,
   (b) Estimate the background fractions.
4. Estimate the efficiency on the Dalitz plot using simulated samples,
   (a) Calculate the averaged efficiency for the Ω_c^{**0}.
5. Test the spin hypotheses for each peak,
   (a) Perform pseudoexperiments to evaluate the significance of the spin hypothesis.

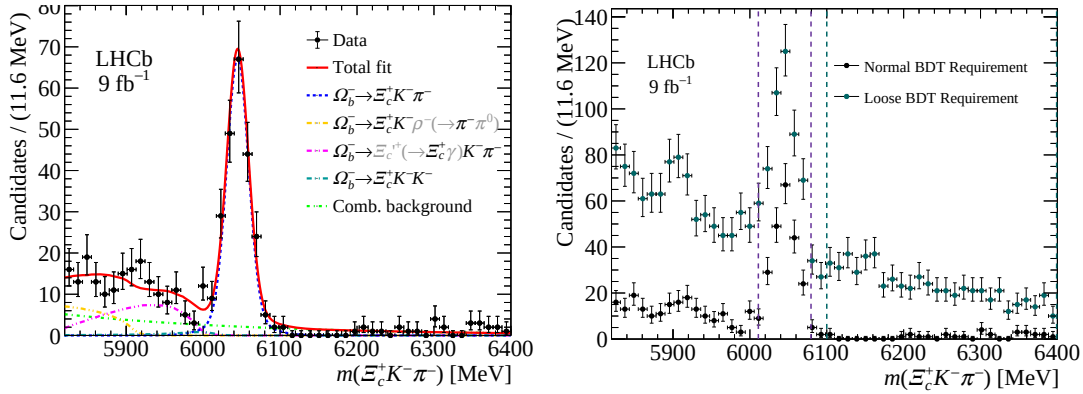

Figure 6.17 Model to the $m_{\Xi_c^+ K^- \pi^-}$ distribution for the selected sample with the default BDT output requirements (purple data points) and extended BDT output requirement (blue data points). The signal and the background ranges are shown between purple and blue dashed lines, respectively.

6.6.1 Fitting the mass distributions

The data set is selected by applying the BDT response requirements, 0.32 for Run 1 and 0.25 for Run 2, and choosing ranges of the $m_{\Xi_c^+ K^- \pi^-}$ and $m_{\Xi_c^+ K^-}$ masses. The range for the $\Xi_c^+ K^- \pi^-$ distribution is $5.82 < m_{\Xi_c^+ K^- \pi^-} < 6.4$ GeV, which is chosen in order to leave enough candidates with higher masses to constrain the background. For the $\Xi_c^+ K^-$ distribution the range $m_{\Xi_c^+ K^-} - m_{\Xi_c^+} - m_{K^-} < 0.22$ GeV is used. The total data set contains 470 candidates, 74 for Run 1 and 396 for Run 2. The fit performed on the $\Xi_c^+ K^- \pi^-$ mass distribution is shown in Fig. 6.17, which is similar to that of the one described in Sec. 5.7. Some of the shape parameters of the components are fixed, these include: the fraction of the $\Xi_c^+ K^- K^-$ background at 2.8% of the signal component, the slope of the combinatorial background determined from the wrong-sign sample, and the Ω_b^- signal is described by the combination of two Gaussian functions with σ_1/σ_2 and the fraction of yields fixed, described in Sec. 5.7.

The signal range is defined as $\pm 2\sigma$ around the Ω_b^- mass found from Fig. 6.17 (left). This range is shown between the purple dashed lines in Fig. 6.17 (right). The number of candidates found in this region is 229 including the combinatorial background which is estimated to be 17.4 ± 2.8. To parameterise the combinatorial background the right side-band of the Ω_b^- mass is used, shown between the blue dashed lines in Fig. 6.17 (right). Due to a low number of candidates the requirement on the BDT response is relaxed to BDT > 0 for the background sample. The $\Xi_c^+ K^-$ mass distribution is modelled by a first-order polynomial

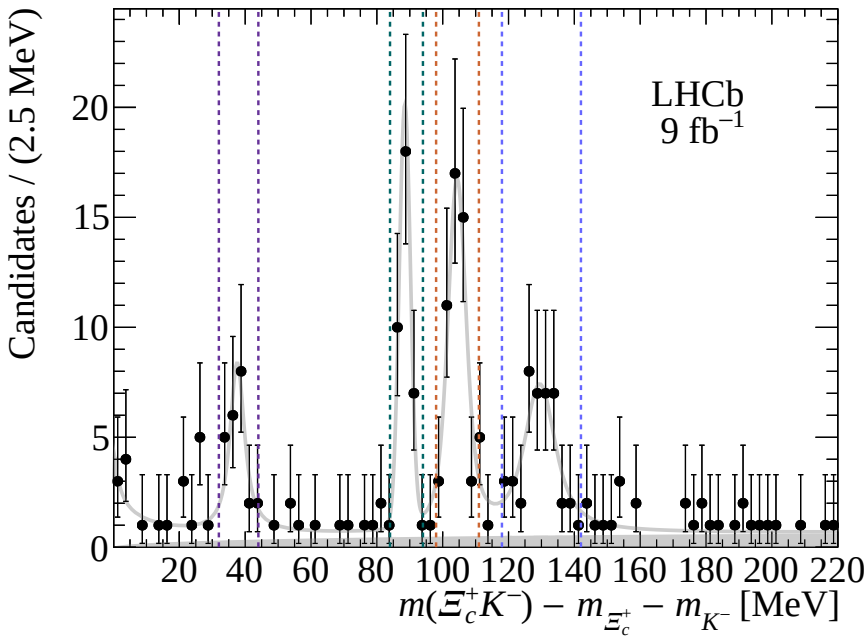

Figure 6.18 Fit to the $\Xi_c^+K^-$ mass distribution, where the intervals used for the Ω_c^{**0} angular analysis are shown by the coloured dashed lines around each peak.

phase-space function, and the angular distribution is described by a third-order polynomial.

The models of the $\Xi_c^+K^-$ mass distribution are shown in Sec. 6.2.1. The model with the Gaussian constrained widths, shown in Fig. 6.12, is used for the spin analysis. This model is used to find the intervals for the Ω_c^{**0} angular analysis and constrain the fraction of the backgrounds, shown in Fig. 6.18. The relativistic BW functions convoluted with the Gaussian function for resolution are added incoherently to the two-component background, where the shape and fraction of the combinatorial background are fixed. For the non-resonant Ω_c^{**0} background the phase-space distribution is used allowing the yield to vary in the fit. Parameters from this fit are listed in Table 6.6. Candidates used for the angular analysis are shown between the coloured dashed lines in Fig. 6.18.

6.6.2 Efficiency estimation

To determine the $\Omega_b^- \to \Xi_c^+K^-\pi^-$ decay properties the efficiency as a function of kinematic variables needs to be understood. The variables used to describe the decay kinematics are shown in Fig. 6.19. The Ω_b^-, Ξ_c^+, K^-, and π^- particles are numbered 0, 1, 2, and 3 respectively. The invariant masses of the particle

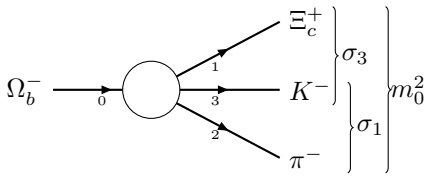

Figure 6.19 Notations for the $\Omega_b^- \to \Xi_c^+ K^- \pi^-$. The variable σ corresponds to s throughout this chapter and denotes the invariant mass squared of the two-particle subsystems. The small numbers of the particle lines indicate the numbering convention used throughout this section.

Table 6.9 Summary of the processed simulation files. Generated is the number of candidates generated in the simulation, pre-selected is the number of candidates after stripping and trigger. Selected is the candidates remaining after offline selections, and BDT is after the requirement on the BDT output is applied.

Configuration	Generated	Pre-selected	Selected	BDT
Magnet Up Run 1	5000505	170082	39616	25805
Magnet Down Run 1	5068746	172963	41064	27092
Magnet Up Run 2	1566372	1440354	234271	181087
Magnet Down Run 2	1511401	1392488	234055	181375

pairs are labeled by s_k using the spectator notations for the index, given by; $s_1 = m^2(K^-\pi^-)$, $s_2 = m^2(\Xi_c^+\pi^-)$, and $s_3 = m^2(\Xi_c^+ K^-)$. To estimate the efficiency four large simulated samples are used which are distributed according to phase space, given in Table 6.9. The efficiency is parameterised in the region:

$$m^2(\Xi_c K^-) < (3.3\,\mathrm{GeV})^2, \tag{6.25}$$

$$m^2(\Xi_c \pi^-) > 22\,\mathrm{GeV}^2. \tag{6.26}$$

The main variation of efficiency is observed along the $m(\Xi_c^+\pi^-)$ dimension. A drop in efficiency is observed towards the kinematic limit, $m_{max}(\Xi_c^+ K^-) = (m_{\Omega_b^-} - m_{\pi^-})^2$. Therefore, the mapping is performed for the $m(\Xi_c^+ K^-) \times m(\Xi_c^+\pi^-)$ representation of the phase space to the domain $\hat{x} \times \hat{y} \in [-1,1] \times [-1,1]$, and a series of Legendre polynomials is used to approximate it. The mapping variables, $\hat{x}(m,z)$ and $\hat{y}(m,z)$ are functions of $m(\Xi_c^+ K^-)$ and the cosine of the helicity angle, $\cos\theta$. An efficiency map is found and used to determine the averaged efficiency, $\bar{\epsilon}$, for every Ω_c^{**0} peak.

6.6.3 Tests of spin hypothesis

The angular distribution is modelled by the density function

$$D_j(\cos\theta) = f_s S_J(\cos\theta)\bar{\epsilon}(\cos\theta) + f_{B1}B_1(\cos\theta) + (1 - f_s - f_{B1})B_2(\cos\theta)\bar{\epsilon}(\cos\theta), \tag{6.27}$$

where the angular distribution $S_J(\cos\theta)$ corresponds to a decay of a spin-J particle, and B_1 and B_2 are the density functions for the combinatorial and non-resonant background components, respectively. The functions B_1 and B_2 are fixed by the side-band of the signal sample and the simulated phase space distribution respectively. Both B_2 and S are are multiplied by the averaged efficiency function, $\bar{\epsilon}(\cos\theta)$. The parameters f_s and f_{B1} are the fractions of signal and combinatorial background obtained in the fit. The tails of the signal components have a small contribution in each signal region, this is put into the non-resonant Ω_c^{**0} component. Since this distribution is partly unknown, the full fraction is calculated by $(1 - f_s - f_{B1})$. The tested spin hypotheses are $J = 1/2$, $J = 3/2$, and $J = 5/2$, which are shown in Fig. 6.20. The asymmetry and the decrease in yield at $\cos\theta = 1$ is due to a drop in efficiency.

To discriminate between the different spin hypotheses two test statistic observables are introduced:

$$\mathrm{TS}_{1|3}^{(N)} = \frac{1}{N}\sum_{e=1}^{N}\mathrm{TS}_{1|3}(\cos\theta_e), \quad \mathrm{TS}_{1|3}(\cos\theta) = \log D_{1/2}(\cos\theta) - \log D_{3/2}(\cos\theta), \tag{6.28}$$

$$\mathrm{TS}_{3|5}^{(N)} = \frac{1}{N}\sum_{e=1}^{N}\mathrm{TS}_{3|5}(\cos\theta_e), \quad \mathrm{TS}_{3|5}(\cos\theta) = \log D_{3/2}(\cos\theta) - \log D_{5/2}(\cos\theta),$$

the indices 1|3 and 3|5 indicate comparing hypotheses 1/2 against 3/2 and 3/2 against 5/2, respectively. The value of the test statistic, $\mathrm{TS}_{2J|2J'}$, is calculated using the data sample and gives different values if the data is distributed according to different spin hypotheses. Generally, $\mathrm{TS}_{2J|2J'} > 0$ favours J hypothesis and $\mathrm{TS}_{2J|2J'} < 0$ prefers the J' hypothesis. Distributions of the observables are found using multiple pseudoexperiments. The ellipses corresponding to 1σ and 2σ double-tailed intervals are found in the two-dimensional distribution of $\mathrm{TS}_{1|3} \times \mathrm{TS}_{3|5}$, shown in Fig. 6.21. To get the rejection significance of each hypothesis, the deviations of the measured test-statistic from the expected values are found

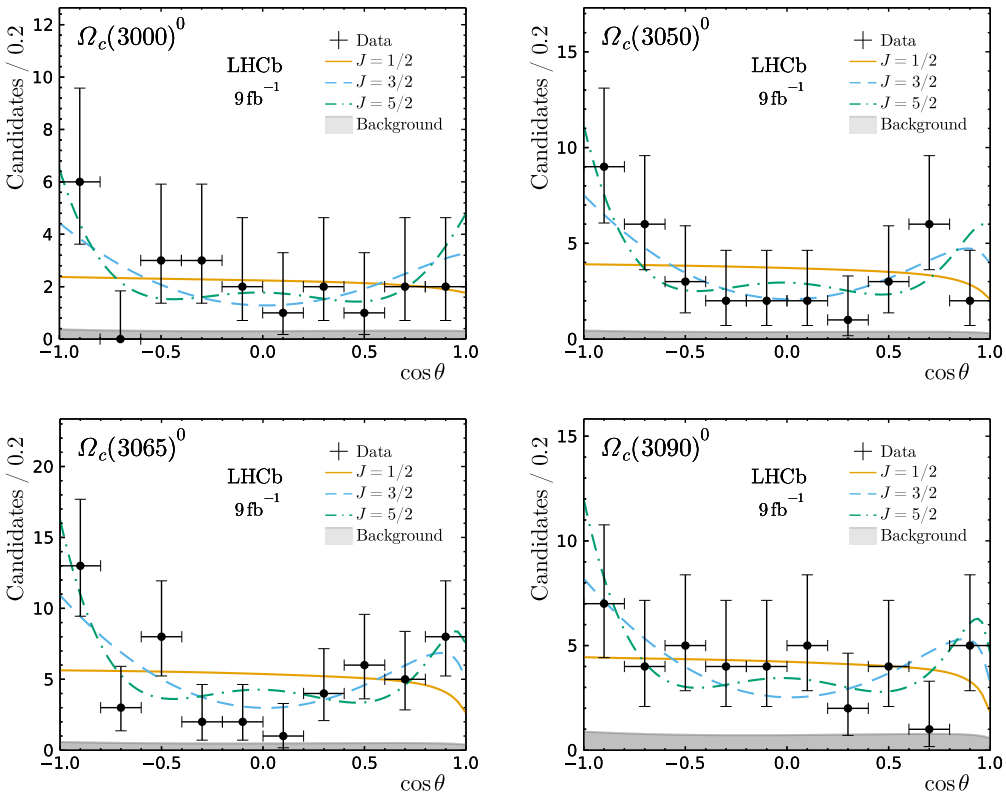

Figure 6.20 Distributions of signal candidates of $\cos\theta$ for each of the four Ω_c^{**0} peaks. The solid lines show the different spin hypotheses. The level of background is shown by the gray shaded area.

by the calculation of the p-value. The p-value is found for both observables separately, and the combination, referred to as the two-dimensional test statistic. The one-dimensional p-value is calculated using the two-tailored z-test:

$$p = \text{erfc}(z/\sqrt{2}), \qquad \text{where} \qquad z = \frac{|t - \mu_{TS}|}{\sigma_{TS,N}}, \tag{6.29}$$

where t stands for one of the test statistic observables. The rejection significance is shown as the number of Gaussian standard deviations using:

$$n_\sigma = \sqrt{2} erfcinv(p), \tag{6.30}$$

where erfcinv is the inverse complementary error function. For the two-dimensional p-value the expectation density is integrated in the two-dimensional space of the test statistic. It is computed as:

$$p = exp(-(\Delta x_\sigma^2 + \Delta y_\sigma^2)/2), \tag{6.31}$$

where Δx and Δy is the distance between the mean and the measured point in the orthonormal coordinates, determined by the covariance matrix. The expectation regions and the measured values are shown in Fig. 6.21. The legend shows the rejection significance of each hypothesis.

Due to a low number of candidates in the signal sample the measurements are limited. However, some rejection significance's to note are seen in the second and third peak for the hypothesis of $J = 1/2$. A test of the combined hypothesis where the quantum numbers for all peaks are assigned is also done. The combined p-value is found as a product of the four individual values. The H_0 hypothesis often preferred in literature, where the states are assigned to $1P$ in the sequence, $H_0 : 1/2^-,\ 1/2^-,\ 3/2^-,\ 3/2^-,\ 5/2^-$, is tested. Using the product of the two dimensional p-values the H_0 is rejected with a significance of 3.6σ. Mostly originating from the second peak, $\Omega_c(3050)^0$, clearly being incompatible with the $J = 1/2$ hypothesis, which can be seen in Fig. 6.20. The measurements are summarised in Table 6.10.

A validation of this method was performed using the $\Xi_b^- \to \Sigma_c^0\ (\to \Lambda_c^+\pi^-)K^-$ decay due to the similar topology compared with the $\Omega_b^- \to \Xi_c^+ K^-\pi^-$ decay. It has the same spin-party combination as the $\Omega_b^- \to \Xi_c^+ K^-\pi^-$ decay and the same final state tracks. This decay mode has a larger number of candidates and the two states, $\Sigma_c(2455)^0$ and $\Sigma_c(2520)^0$, have well identified spin assignments, allowing

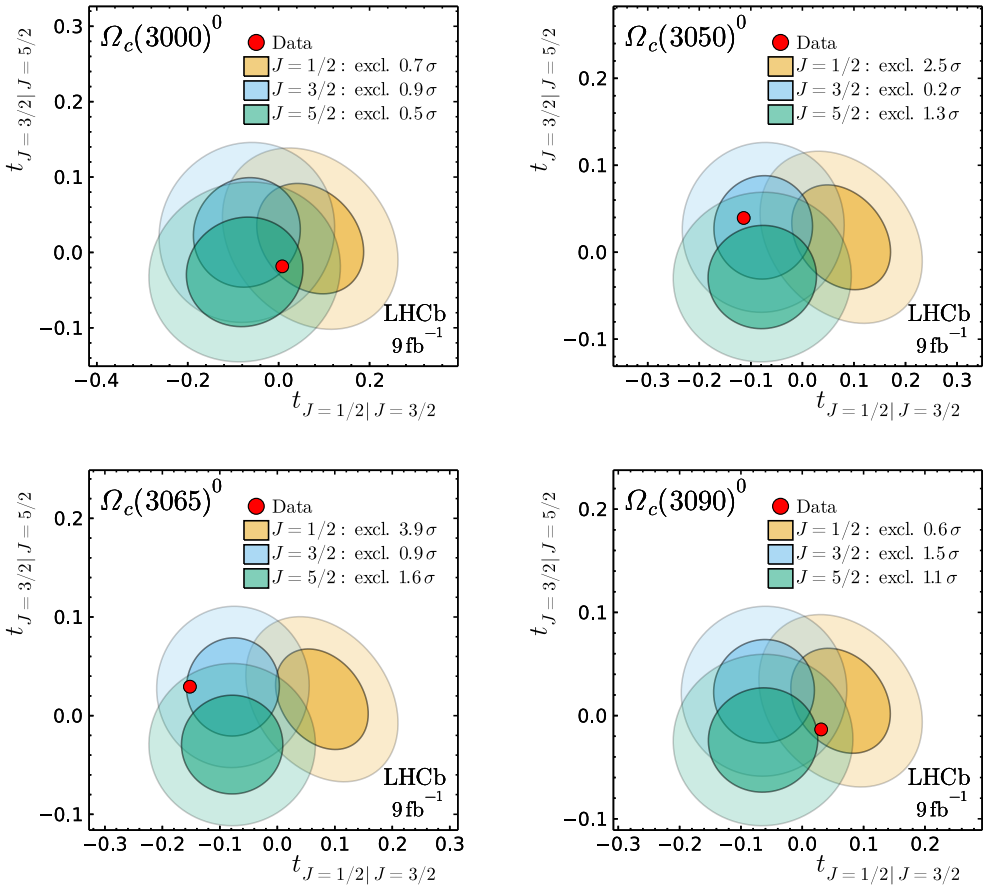

Figure 6.21 Value of the observables $\text{TS}_{1|3}$ and $\text{TS}_{3|5}$ under different spin hypothesis $s \in \{1/2, 3/2, 5/2\}$ calculated for the four Ω_c^{**0} states.

Table 6.10 Rejection significance calculated using 2 dimensional p-values.

the state	$J=1/2$	$J=3/2$	$J=5/2$	H_0
$\Omega_c(3000)^0$	0.7σ	0.9σ	0.5σ	0.7σ
$\Omega_c(3050)^0$	2.5σ	0.2σ	1.3σ	2.5σ
$\Omega_c(3065)^0$	3.9σ	0.9σ	1.7σ	0.9σ
$\Omega_c(3090)^0$	0.6σ	1.5σ	1.1σ	1.5σ
combined	–	–	–	3.6σ

a comparison with previous measurements. It is concluded that the excited Σ_c^0 states match the expected angular assignments, and it also reveals an important role of the background in the calculation of the significance, accounted for in the systematic uncertainties.

6.7 Systematic studies

The systematic uncertainty on each value needs to be determined. Many sources are considered and detailed in this section, including variations in fit models and weighting of simulated samples to match data samples. The total systematic uncertainty on each value is summarised in the tables at the end of this section.

6.7.1 Alternative Ω_b^- fit model

In the $\Omega_b^- \to \Omega_c^0\pi^-$ decay mode three partially reconstructed decays are added to the final fit model. The shape of the $\Omega_b^- \to \Omega_c^{*0}\pi^-$ and $\Omega_b^- \to \Omega_c^0\rho^-$ decays are determined with the assumption that the Ω_b^- candidates are not polarised. The different available line shapes, determined by the different helicity components, are shown in Fig. 6.22. The different hypotheses depending on couplings are given by the dashed lines. The different spin components have been tested in the total fit model and the differences on the final results with respect to the default fit model are quoted as a systematic uncertainty. The fit models with the different components of the $\Omega_c^{*0}\pi^-$ and $\Omega_c^0\rho^-$ are shown in Fig. 6.23 and 6.24, respectively. The most notable change is in the fit to the $\Omega_c^{*0}\pi^-$ component.

Additionally, the shape of the signal component has been varied to a double Crystal Ball function and a Novosibirsk function combined with a Gaussian function. These are then compared to the default fit of a double Gaussian function, and the difference in fit parameters is quoted as a systematic uncertainty. The shapes are chosen due to their accurate description of the simulated sample. Similar studies have been performed to the $\Omega_b^- \to \Xi_c^+K^-\pi^-$ decay. In the default fit model the ratio of $N(X_cK^-)/N(X_c\pi^-)$ is fixed to 2.8%, where X_c is Ω_c^0 or $\Xi_c^+K^-$. To determine a systematic uncertainty on this approximation the ratio is shifted by $\pm 20\%$ and the difference to the fit parameters is calculated.

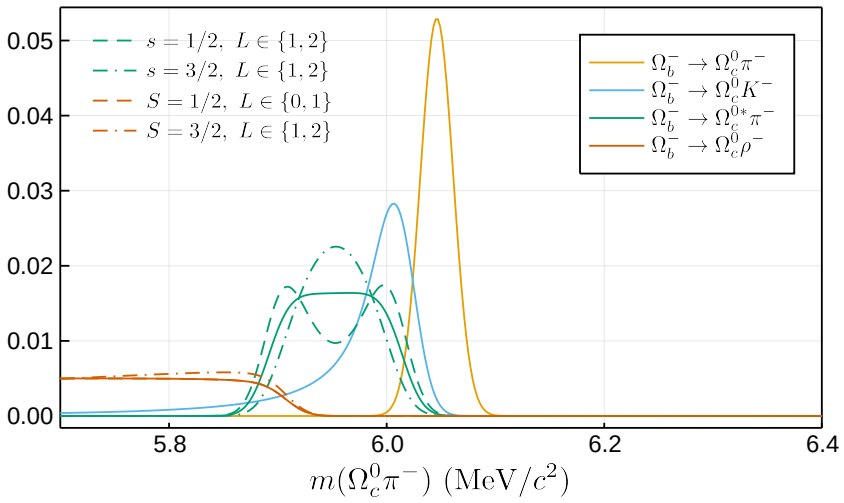

Figure 6.22 Analytical calculation of the different shapes for the model to the $\Omega_c^0\pi^-$ mass spectrum. The partially reconstructed components for the spin-less particles are shown by the solid lines. Different spin hypotheses depending on the couplings give the dashed lines.

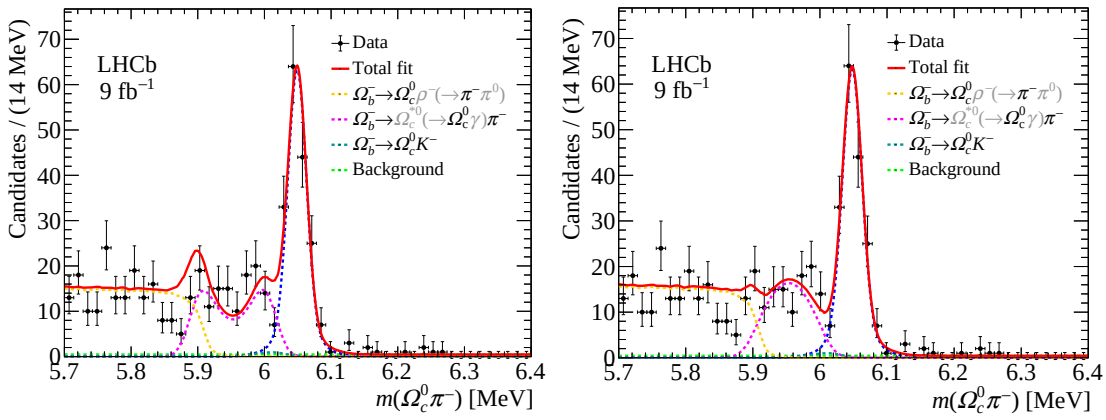

(a) S=1/2 (b) S=3/2

Figure 6.23 Total fit model of the $\Omega_c^0\pi^-$ mass distribution with the different helicity components of the Ω_c^{*0}.

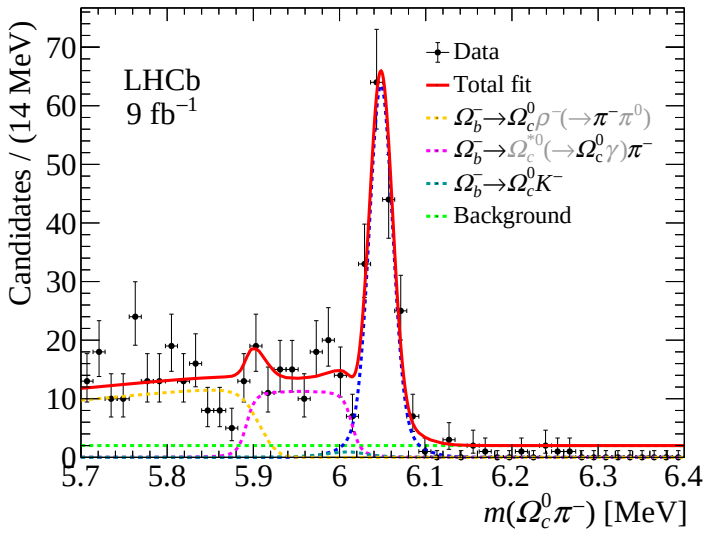

Figure 6.24 Total fit model performed on the $\Omega_c^0\pi^-$ mass distribution with the alternative helicity component of the $\Omega_c^0\rho^-$.

6.7.2 Momentum calibration

A momentum calibration is applied to all samples used in the analysis process. The momentum calibration is known with a precision of 0.03%. A systematic uncertainty is found by taking ±0.03% of the Q-value of the decay, where Q is the available kinetic energy of the decay, given by:

$$Q = m_{parent} - \sum m_{children}, \tag{6.32}$$

where in our case m_{parent} is the mass of the Ω_b^- and $m_{children}$ are the masses of the decay products. More information on the momentum calibration can be found in Ref. [91]. The Q-value of the $\Omega_b^- \to \Xi_c^+ K^- \pi^-$ decay is smaller than the $\Omega_b^- \to \Omega_c^0 \pi^-$ decay, leading to a smaller systematic uncertainty.

6.7.3 Variations effecting the BDT output

- **Binned weighting of the Ξ_c^+ Dalitz plot**: The Ξ_c^+ Dalitz distribution is generated through phase-space in simulation, providing a flat distribution. The simulation is weighted according to data, described in Sec. 5.6.1. The weight of each bin in the data sample is applied to each bin in the simulated sample. To estimate a systematic uncertainty on the weighting procedure the binning scheme has been varied and the effect on the overall results

is quoted as a systematic. The bin width is varied by ±20% to allow for a conservative estimation. Simulated samples with a different bin width for the Ξ_c^+ Dalitz plot are used as the signal input for the multivariate analysis and the BDT classifier is trained again using the same background sample. A small change in BDT output is observed, affecting the end result. The selection on the BDT response is noted to be the same as the default selection. The difference in results compared to the default model is taken as the systematic uncertainty.

- **Particle identification efficiency**: In the simulated samples of the $\Omega_b^- \to \Xi_c^+ K^- \pi^-$ and $\Omega_b^- \to \Omega_c^0 \pi^-$ decays the particle identification is weighted using calibration data. There is a systematic uncertainty associated to this which must be taken into account when calculating the signal efficiency of each decay mode. The calibration data, developed by the LHCb experiment, is used to weight the PID variables in simulation in order to improve the similarity to the PID performance in the data samples. To determine the systematic uncertainty on the calibration method an alternative template to calculate the PID distributions is used. The BDT classifier is trained using the alternative weighting on the simulated samples and the difference on the overall results are taken as a systematic uncertainty.

- Ω_b^- **kinematic weighting**: The agreements between the Ω_b^- baryon transverse momentum, pseudorapidity and track multiplicity in data and simulation is good but could be improved. To achieve this the Ω_b^- baryon kinematics in simulation are weighted according to the data samples, next the efficiencies are evaluated and a systematic from the difference in final results is quoted. The weights applied to the variables in the simulated samples are an input into the multivariate analysis when training the BDT algorithm. The selection on the BDT response is the same as the default selection. The comparison of the data to simulation before and after the weighting is performed is shown in Fig. 6.25, 6.26, and 6.27 for transverse momentum, η, and track multiplicity, respectively. The data is shown in green and the simulation is in purple. After weighting, the simulation is shown to match the data sample. The systematic uncertainty is taken as the difference between the results from the default model and the model after weights have been applied.

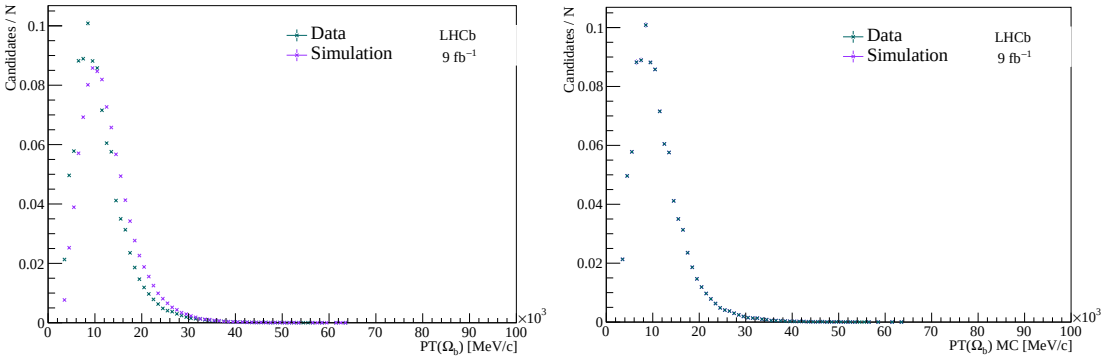

(a) (b)

Figure 6.25 Distributions of the transverse momentum of the Ω_b^- for data (blue) and simulation (purple). Figure (a) shows the distributions before weighting and figure (b) shows the distribution after.

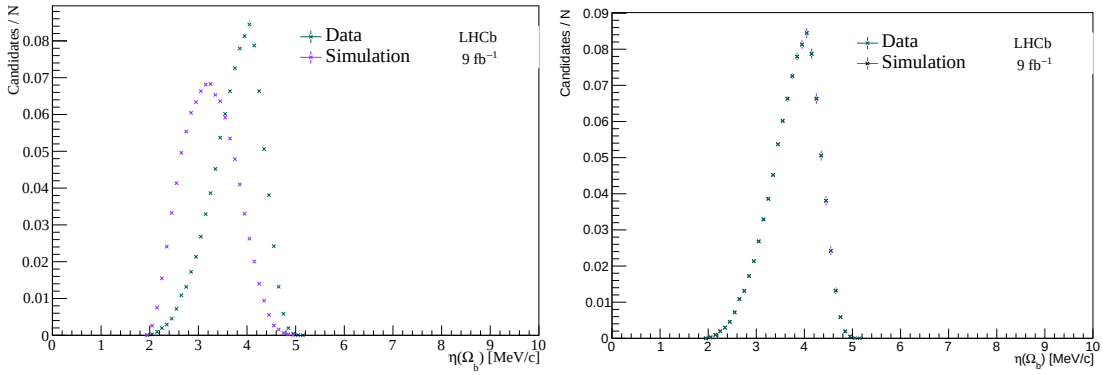

(a) (b)

Figure 6.26 Distribution of η for the Ω_b^- candidates, data is shown in blue and simulation is in purple. Figure (a) shows the distribution before weighting and figure (b) shows the distribution after.

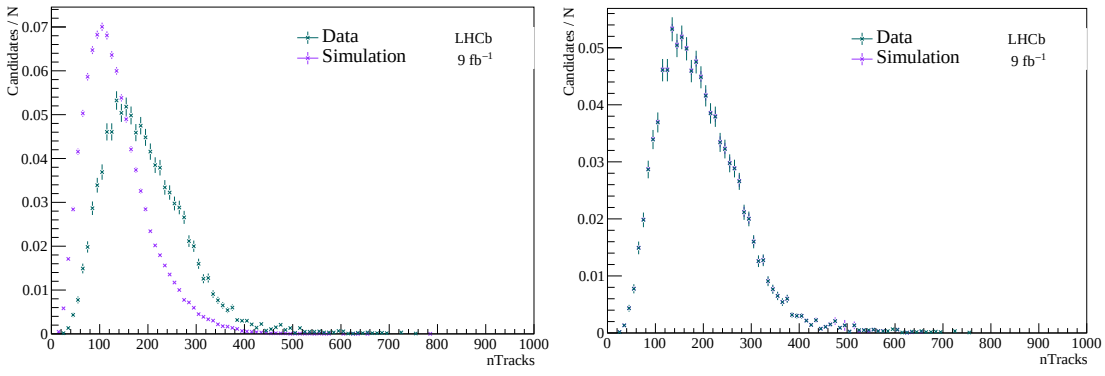

(a) (b)

Figure 6.27 Distribution of the track multiplicity in data (blue) and simulation (purple). Figure (a) shows the distribution before weighting and figure (b) is after.

Table 6.11 Absolute values of the changes of the mass and width parameters of $\Omega_c(3000)^0$, $\Omega_c(3050)^0$, $\Omega_c(3065)^0$, and $\Omega_c(3090)^0$ in MeV. The model includes an alternative resolution of the Gaussian function compared to the default model.

Resolution	Δm_1	Δm_2	Δm_3	Δm_4	$\Delta\Gamma_1$	$\Delta\Gamma_2$	$\Delta\Gamma_3$	$\Delta\Gamma_4$
-10%	< 0.01	< 0.01	< 0.01	0.02	0.17	< 0.01	0.39	0.20
$+10\%$	0.01	< 0.01	-0.02	0.02	0.13	< 0.01	0.41	0.20

6.7.4 Efficiency parameterisation

The efficiency found on the Dalitz plane of the $\Omega_b^- \to \Xi_c^+ K^- \pi^-$ decay is parameterised by an expansion of Legendre polynomials. To determine a systematic uncertainty on this factor the expansion is varied to two different combinations. The default model uses $L_{max} = (1, 5)$ and the combinations (2,6) and (1,4) are tested. The difference to the final results are taken as the systematic.

6.7.5 Alternative $\Xi_c^+ K^-$ model

Alternative fit models to the $\Xi_c^+ K^-$ mass distribution are tested in order to determine systematic uncertainties on the masses, widths, and production rates of the Ω_c^{**0} states. Firstly, the resolution of each Gaussian function, used to describe detector resolution, has been varied by $\pm 10\%$, and the variation on the masses and widths from the default model is taken as the systematic on this quantity, shown in Table 6.11.

In addition, the interference between model components are considered. In a series of fits the amplitudes of the neighbour peaks are included coherently with an additional complex phase as a fit parameter. Interference of every resonance with the background is also tested. Table 6.12 summarises the deviations of the mass and width of each state found from this variation.

The parametisation of the signal components includes the orbital angular momentum of the $\Omega_c^{**0} \to \Xi_c^+ K^-$ decay, determined by the spin of the components. In the default fit model the value is set to $l = 0$. To determine a systematic uncertainty on this assumption values of $l = 1$ and $l = 2$ are tested, together with different values of the size parameter R. The value of l is varied for the background component as well. The angular distribution of the background component for the angular analysis is changed as follows: $l = 0 \to J = 1/2$, $l = 1 \to J = 3/2$, and

Table 6.12 Changes in the mass and width parameters of $\Omega_c(3000)^0$, $\Omega_c(3050)^0$, $\Omega_c(3065)^0$, and $\Omega_c(3090)^0$ in MeV. The first columns states which amplitudes are added coherently. 0 refers to the threshold enhancement, b refers to the background component.

Interf.	ΔNLL	Δm_1	Δm_2	Δm_3	Δm_4	$\Delta\Gamma_1$	$\Delta\Gamma_2$	$\Delta\Gamma_3$	$\Delta\Gamma_4$
$\lvert 0+1\rvert^2$	-0.94	0.66	-0.01	< 0.01	-0.03	1.37	< 0.01	0.13	-0.16
$\lvert 1+2\rvert^2$	0.05	0.03	-0.02	< 0.01	-0.0	-0.11	0.03	-0.01	-0.01
$\lvert 2+3\rvert^2$	-0.23	-0.01	0.09	-0.11	0.04	0.09	0.14	0.13	-0.15
$\lvert 3+4\rvert^2$	-0.09	< 0.01	< 0.01	-0.17	0.39	-0.05	< 0.01	-0.15	-0.33
$\lvert 0+b\rvert^2$	-0.15	-0.08	-0.0	< 0.01	-0.01	0.52	< 0.01	-0.0	-0.15
$\lvert 1+b\rvert^2$	-0.7	0.7	-0.01	< 0.01	-0.04	2.09	< 0.01	0.17	-0.28
$\lvert 2+b\rvert^2$	-0.19	-0.02	0.1	-0.01	-0.01	0.13	0.07	0.1	0.17
$\lvert 3+b\rvert^2$	-0.19	0.02	0.01	-0.28	0.1	-0.18	< 0.01	-0.03	-0.89
$\lvert 4+b\rvert^2$	-0.01	< 0.01	-0.0	0.01	-0.17	-0.02	< 0.01	0.06	-0.01

$l = 2 \to J = 5/2$. All changes to the significance are summarised in Table 6.16.

6.7.6 Modification to combinatorial background

The combinatorial background equates to less than 5% of the selected events in the $\Xi_c^+ K^-$ mass range. Its distribution in the $\Xi_c^+ K^-$ and $\cos\theta$ dimensions are constrained by the fit to the upper side band in the $\Xi_c^+ K^- \pi^-$ invariant mass spectrum. When determining the shape of the distribution the selection on the BDT response was reduced to increase the number of candidates and improve the fit quality. Previously a selection of $\mathrm{BDT}_{bkg} > 0$ was used, here the requirement is changed to $\mathrm{BDT}_{bkg} > 0.1$ and the fit is performed again using a new parameterisation of the background. The number of background sample events are reduced by half, however, the estimated shapes of the $\Xi_c^+ K^-$ and $\cos\theta$ distributions are similar, shown in Fig. 6.28. The deviation on the mass, width and yield of the signal components are negligible compared to other systematic uncertainties. An updated $J = 1/2$ rejection significance for the $\Omega_c(3050)^0$ and $\Omega_c(3065)^0$ states are found to be 2.3σ and 4.2σ. The rejection of the H_0 combined hypothesis is 3.4σ.

6.7.7 Summary

The different results are split into five categories: measurements of masses, widths, ratio of branching fractions, significance and spin rejection hypotheses. The tables below show the relevant sources of the systematic uncertainties for each

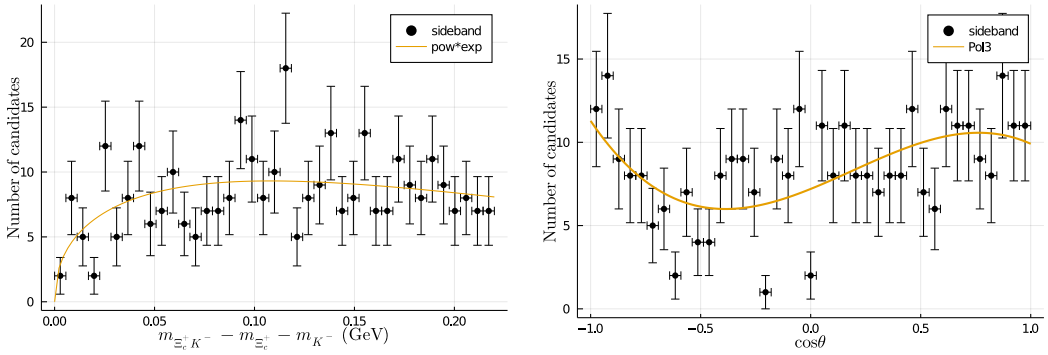

Figure 6.28 Background distribution with the modified requirement on the BDT response, to be compared to Fig. 6.8. The parameters of the mass fit on the $\Xi_c^+ K^-$ mass spectrum (left) are: $\alpha = 0.44 \pm 0.17$, $\beta = -4.0 \pm 2.2$. The parameters of the fit to the $\cos\theta$ distribution (right) are: $c_1 = 0.74 \pm 0.28$, $c_2 = 0.47 \pm 0.25$, $c_3 = -0.84 \pm 0.42$.

result. Table 6.13 shows the systematic uncertainties for the masses of the Ω_b^-, the branching fraction and the production rate of each excited Ω_c^0 state. The systematic uncertainties for the masses and widths of each excited Ω_c^0 resonance is shown in Tab. 6.14. For the yield of the missing $\Omega_c(3119)^0$ and the width of the $\Omega_c(3050)^0$ state an upper limit is set. An estimation of the impact of the systematic uncertainties to the limit values is done by presenting the limit for every source, shown in Table. 6.15. The conservative upper limit is found by choosing the lowest value. The significance of each excited Ω_c^0 state, corrected for systematic uncertainty, is shown in Table. 6.16. Finally, the systematic uncertainties for the spin hypothesis rejection is shown in Tab. 6.17.

Table 6.13 Systematic uncertainties of the masses, branching fractions and production rates.

Source	$m(\Xi_c^+ K^- \pi^-)$	$m(\Omega_c^0 \pi^-)$	$\frac{\mathcal{B}(\Xi_c^+ K^- \pi^-)}{\mathcal{B}(\Omega_c^0 \pi^-)}$	$\mathcal{P}(\Omega_c(3000)^0)$	$\mathcal{P}(\Omega_c(3050)^0)$	$\mathcal{P}(\Omega_c(3065)^0)$	$\mathcal{P}(\Omega_c(3090)^0)$
Alternative Ω_b^- fit model	< 0.1	0.5	0.05	< 0.01	< 0.01	< 0.01	< 0.01
MC weights (Ξ_c^+ Dalitz)	0.5	0.5	< 0.01	0.03	0.01	< 0.01	0.02
Momentum calibration	0.9	1.0	—	—	—	—	—
PID Efficiency	0.2	0.9	0.01	< 0.01	0.02	0.01	0.03
Ω_b^- kinematics	0.4	1.3	< 0.01	0.01	< 0.01	0.01	0.01
Alternative $\Xi_c^+ K^-$ fit model	—	—	—	0.02	0.01	0.02	0.01
Efficiency Map	—	—	—	< 0.01	< 0.01	< 0.01	< 0.01
Background in $\Xi_c^+ K^-$	—	—	—	< 0.01	< 0.01	< 0.01	< 0.01
Total	1.1	2.0	0.05	0.04	0.02	0.02	0.04

Table 6.14 Systematic uncertainties for the masses and widths of each Ω_c^{**} resonance.

	$\Omega_c(3000)^0$		$\Omega_c(3050)^0$		$\Omega_c(3065)^0$		$\Omega_c(3090)^0$	
Source	m [MeV]	Γ [MeV]	m [MeV]	Γ [MeV]	m [MeV]	Γ [MeV]	m [MeV]	Γ [MeV]
Alternative Ω_b^- fit	< 0.01	< 0.01	< 0.01	< 0.01	< 0.01	< 0.01	< 0.01	< 0.01
Ξ_c^+ Dalitz weights	0.20	1.1	0.10	< 0.01	0.14	0.20	0.32	1.24
Momentum calibration	0.01	—	0.03	—	0.03	—	0.04	—
PID efficiency	0.56	0.1	0.05	< 0.01	0.14	0.2	0.73	2.1
Ω_b^- kinematics	0.13	0.7	0.10	< 0.01	0.21	0.2	0.42	0.9
Alternative $\Xi_c^+ K^-$ fit	0.70	2.1	0.10	0.10	0.28	0.41	0.39	0.9
Efficiency map	< 0.01	< 0.01	< 0.01	< 0.01	< 0.01	< 0.01	< 0.01	< 0.01
Background in $\Xi_c^+ K^-$	0.02	0.09	< 0.01	< 0.01	< 0.01	0.04	< 0.01	0.18
Total	0.9	2.5	0.2	0.1	0.4	0.5	1.0	2.8

Table 6.15 Likelihood scan for the parameters N_5 and Γ_2 for every systematic study.

	N_5		$\Gamma_2^{(\text{upper})}$ [MeV]	
Source	CL 95%	CL 90%	CL 90%	CL 95%
Default model	4.9	6.1	1.0	1.3
Ξ_c^+ weights (40 bins)	2.8	3.7	1.2	1.6
Ξ_c^+ weights (90 bins)	3.1	4.1	0.9	1.2
PID Efficiency	4.7	5.7	1.0	1.4
Ω_b^- kinematics	3.5	4.6	1.0	1.4
Dalitz eff. map of $\Omega_b^- \to \Xi_c^+ K^+ \pi^-$	4.9	6.1	1.0	1.3
Background BDT requirement	4.9	6.1	1.0	1.3
Background in $\Xi_c^+ K^-$: $J = 3/2$	4.9	6.1	1.0	1.3
Background in $\Xi_c^+ K^-$: $J = 5/2$	4.9	6.0	1.0	1.3
The highest upper limit	4.9	6.1	1.2	1.6

Table 6.16 Significance of the peaking structures found by exclusion of the components from the fit. For the four main components the significance is calculated using $\sqrt{2\text{NLL}}$.

Source	$\Delta\text{NLL}^{(0)}$	$n_\sigma^{(0)}$	$n_\sigma^{(1)}$	$n_\sigma^{(2)}$	$n_\sigma^{(3)}$	$n_\sigma^{(4)}$
Default model	18.0	5.4	6.4	10.9	12.2	7.9
Ξ_c^+ weights (40 bins)	18.6	5.5	7.0	10.4	12.4	8.1
Ξ_c^+ weights (90 bins)	19.0	5.6	6.2	10.7	11.9	7.8
PID Efficiency	13.7	4.6	6.4	9.9	11.9	7.9
Ω_b^- kinematics	12.2	4.3	6.8	10.8	12.4	7.9
Dalitz eff. map of $\Omega_b^- \to \Xi_c^+ K^+ \pi^-$	18.0	5.4	6.4	10.9	12.2	7.9
Background BDT requirement	18.6	5.5	6.4	10.9	12.2	7.9
Background in $\Xi_c^+ K^-$: $J = 3/2$	26.5	6.7	6.2	11.0	12.3	8.0
Background in $\Xi_c^+ K^-$: $J = 5/2$	29.4	7.1	6.0	11.1	12.7	8.3
Shape of the threshold structure	16.2	5.1	6.4	10.9	12.2	7.9
Minimal significance	12.2	4.3	6.2	9.9	11.9	7.8

Table 6.17 Systematic uncertainties for the spin hypotheses rejection expressed in the number of Gaussian standard deviations for $\Omega_c(3000)^0$, $\Omega_c(3050)^0$, $\Omega_c(3065)^0$, and $\Omega_c(3090)^0$ as the first, second, third, and fourth number at every column. The rejection of the combined hypothesis $H_0 = (1/2, 1/2, 3/2, 3/2)$ is given in the last column.

Source	$J = 1/2$	$J = 3/2$	$J = 5/2$	H_0
Default model	$[0.7, 2.5, 3.9, 0.6]$	$[0.9, 0.2, 0.9, 1.5]$	$[0.5, 1.3, 1.6, 1.1]$	3.6
Ξ_c^+ weights (40 bins)	$[0.6, 3.3, 3.7, 0.6]$	$[1.3, 1.0, 0.6, 1.2]$	$[0.9, 1.7, 1.6, 1.0]$	4.0
Ξ_c^+ weights (90 bins)	$[0.7, 2.9, 3.7, 1.2]$	$[1.0, 0.6, 0.7, 1.6]$	$[0.6, 1.7, 1.3, 0.8]$	3.8
PID Efficiency	$[1.3, 3.0, 3.7, 1.6]$	$[1.2, 0.9, 0.7, 1.5]$	$[0.4, 1.8, 1.2, 0.5]$	4.1
Ω_b^- kinematics	$[0.6, 2.8, 3.9, 1.0]$	$[0.8, 0.7, 0.8, 0.8]$	$[0.6, 1.8, 1.4, 0.6]$	3.5
Dalitz eff. map of $\Omega_b^- \to \Xi_c^+ K^+ \pi^-$	$[0.7, 2.5, 3.9, 0.6]$	$[0.9, 0.2, 0.9, 1.5]$	$[0.5, 1.3, 1.6, 1.1]$	3.6
Background BDT requirement	$[0.7, 2.5, 3.9, 0.6]$	$[0.9, 0.2, 0.9, 1.5]$	$[0.5, 1.3, 1.7, 1.1]$	3.6
Background in $\Xi_c^+ K^-$: $J = 3/2$	$[0.6, 2.3, 3.6, 0.4]$	$[1.1, 0.1, 0.7, 2.0]$	$[0.7, 1.2, 1.6, 1.5]$	3.6
Background in $\Xi_c^+ K^-$: $J = 5/2$	$[0.5, 2.2, 3.6, 0.3]$	$[1.0, 0.2, 0.6, 1.9]$	$[0.7, 1.3, 1.7, 1.5]$	3.5
Minimal significance	$[0.5, 2.2, 3.6, 0.3]$	$[0.8, 0.1, 0.6, 0.8]$	$[0.4, 1.2, 1.2, 0.5]$	3.5

6.8 Results

The $\Omega_c^0\pi^-$ and $\Xi_c^+K^-\pi^-$ invariant mass spectra have been investigated utilising the Run 1 and Run 2 data sets from the LHCb experiment corresponding to an integrated luminosity of 9 fb^{-1}. Four excited Ω_c^0 states which decay to $\Xi_c^+K^-$ are observed in the exclusive decay for the first time and correspond to the states seen before in the inclusive decays by the LHCb and Belle experiments. Each of the four peaks has a significance of over 5σ. The fifth state, $\Omega_c(3119)^0$, previously seen by the LHCb experiment is not observed. An upper limit on the yield of this state is set: $N_5 < 4.9(6.1)$, with 90%(95%) CL. An enhancement at the $\Xi_c^+K^-$ threshold is seen, and is found to have a significance of 4.6σ. This was interpreted as the feed-down of $\Omega_c(3065)^0 \to \Xi_c^{\prime+}(\to \Xi_c^+\gamma)K^-$ in the inclusive analysis, this explanation does not hold in this case due to the selections made on the Ω_b^- baryon mass. The parameters of the four main states are measured:

$$
\begin{aligned}
M(\Omega_c(3000)^0) &= 2999.2 \pm 0.9\,(\text{stat}) \pm 0.9(\text{syst})\ \text{MeV}/c^2,\\
\Gamma(\Omega_c(3000)^0) &= 4.8 \pm 2.1\,(\text{stat}) \pm 2.5\,(\text{syst})\ \text{MeV},\\
N(\Omega_c(3000)^0) &= 23.8 \pm 7.2\,(\text{stat}) \pm 8.4\,(\text{syst}).
\end{aligned}
$$

$$
\begin{aligned}
M(\Omega_c(3050)^0) &= 3050.1 \pm 0.2\,(\text{stat}) \pm 0.2\,(\text{syst})\ \text{MeV}/c^2,\\
\Gamma(\Omega_c(3050)^0) &< 1.2(1.6)\,\text{MeV},\ (90\%)95\%\ \text{CL},\\
N(\Omega_c(3050)^0) &= 33.1 \pm 6.0\,(\text{stat}) \pm 6.2\,(\text{syst}).
\end{aligned}
$$

$$
\begin{aligned}
M(\Omega_c(3065)^0) &= 3065.9 \pm 0.4\,(\text{stat}) \pm 0.4\,(\text{syst})\ \text{MeV}/c^2,\\
\Gamma(\Omega_c(3065)^0) &= 1.7 \pm 1.0\,(\text{stat}) \pm 0.5\,(\text{syst})\ \text{MeV},\\
N(\Omega_c(3065)^0) &= 50.8 \pm 8.3\,(\text{stat}) \pm 4.8\,(\text{syst}).
\end{aligned}
$$

$$
\begin{aligned}
M(\Omega_c(3090)^0) &= 3091.0 \pm 1.1\,(\text{stat}) \pm 1.0\,(\text{syst})\ \text{MeV}/c^2,\\
\Gamma(\Omega_c(3090)^0) &= 7.4 \pm 3.1\,(\text{stat}) \pm 2.8\,(\text{syst})\ \text{MeV},\\
N(\Omega_c(3090)^0) &= 41.4 \pm 9.1\,(\text{stat}) \pm 8.1\,(\text{syst}).
\end{aligned}
$$

An angular analysis of the Ω_c^{**0} resonances is performed by testing $J = 1/2$,

$J = 3/2$, and $J = 5/2$ hypotheses for every peak. The rejection significance is summarized in Table 6.18. A significance of over 3σ for the rejection of the

State	$J = 1/2$	$J = 3/2$	$J = 5/2$
$\Omega_c(3000)^0$	0.5	0.8	0.4
$\Omega_c(3050)^0$	2.2	0.1	1.2
$\Omega_c(3065)^0$	3.6	0.6	1.2
$\Omega_c(3090)^0$	0.3	0.8	0.5

Table 6.18 The rejection significance for each resonance including systematic uncertainties, expressed in terms of the number of Gaussian standard deviations.

spin-1/2 hypothesis for the $\Omega_c(3065)^0$ state is observed. The angular distribution of the $\Omega_c(3050)^0$ state clearly shows an enhancement at $\cos\theta = \pm 1$, indicating a spin higher than 1/2. However, the significance of the $J = 1/2$ rejection is slightly above 2σ due to its narrow width and low number of candidates. The hypothesis on identifying the states in the 1P multiplet, counting from the $\Omega_c(3000)^0$ peak, is given by:

$$H_0 : 1/2^-,\ 1/2^-,\ 3/2^-,\ 3/2^-.$$

This has been rejected at a 3.5σ confidence level. In addition to the above results, the mass of the Ω_b^- is measured:

$$M(\Omega_b^- \to \Omega_c^0\pi^-) = 6048.4 \pm 1.3\ (\text{stat}) \pm 2.0\ (\text{syst})\ \text{MeV}/c^2,$$
$$M(\Omega_b^- \to \Xi_c^+ K^-\pi^-) = 6044.3 \pm 1.2\ (\text{stat}) \pm 1.1\ (\text{syst})\ \text{MeV}/c^2.$$

A weighted average is calculated by averaging the mass of the Ω_b^- from the $\Omega_b^- \to \Xi_c^+ K^-\pi^-$ decay with the previous LHCb measurements. This corresponds to:

$$\bar{M}(\Omega_b^-) = 6044.8 \pm 1.3\ \text{MeV/c}^2.$$

The result for the Ω_b^- mass is consistent and competitive with the current PDG value. The total number of Ω_b^- candidates found in each decay are $N(\Omega_b^- \to \Omega_c^0\pi^-) = 174.3 \pm 13.9$, and $N(\Omega_b^- \to \Xi_c^+ K^-\pi^-) = 240.4 \pm 17.3$. The ratio of branching fractions of $\Omega_b^- \to \Xi_c^+ K^-\pi^-$ relative to $\Omega_b^- \to \Omega_c^0\pi^-$ is determined:

$$\frac{\mathcal{B}(\Omega_b^- \to \Xi_c^+ K^-\pi^-)\mathcal{B}(\Xi_c^+ \to pK^-\pi^+)}{\mathcal{B}(\Omega_b^- \to \Omega_c^0\pi^-)\mathcal{B}(\Omega_c^0 \to pK^-K^-\pi^+)} = 1.35 \pm 0.11\ (\text{stat}) \pm 0.05(\text{syst}).$$

6.9 Discussion

The narrow Ω_c^{**0} states are observed in exclusive Ω_b^- decays for the first time. We find that the $\Omega_b^- \to \Omega_c^{**0}(\to \Xi_c^+ K^-)\pi^-$ decay is the dominating mechanism for the $\Omega_b^- \to \Xi_c^+ K^- \pi^-$ transition. The states $\Omega_c(3000)^0$, $\Omega_c(3050)^0$, $\Omega_c(3065)^0$, and $\Omega_c(3090)^0$ appear clearly in the $\Xi_c^+ K^-$ projection of the decay $\Omega_b^- \to \Xi_c^+ K^- \pi^-$. The fifth state, $\Omega_c(3119)^0$, is not observed. Nevertheless, it is observed that the threshold enhancement, which was suspected as a feed-down component in the prompt analysis, is significant and likely corresponds to a physical state.

The result for the mass of the Ω_b^- baryon is consistent to within 1σ of the reported mass in the PDG. When a weighted average with the previous LHCb measurements is performed it provides an error which is competitive with the current value from the PDG [6].

It is observed that for the production of the Ω_c^{**0} states in the Ω_b^- decay, possible helicity components of the Ω_c^{**0} are restricted by 1/2 due to the spin of the Ω_b^-. Therefore, a non-trivial angular distribution is emerging for the helicity angle of the $\Omega_c^{**0} \to \Xi_c^+ K^-$ process. The hypotheses, $J = 1/2$, $J = 3/2$, and $J = 5/2$ are tested for the observed four narrow Ω_c^{**0} states. Despite the low number of candidates, the spin of the $\Omega_c(3065)^0$ is observed to be larger than 1/2 with a significance of over 3σ. A strong indication of $J > 1/2$ for the $\Omega_c(3050)^0$ is found, where the rejection significance of $J = 1/2$ is 2.2σ, where the systematic uncertainties have been considered. The naive assumption of the observed four peaks with the lowest states of the $1P$ multiplet in the order 1/2, 1/2, 3/2, 3/2 is excluded with a significance of 3.5σ.

If the threshold peak is proven to be an additional Ω_c^{**0} state with spin 1/2, the observed spectrum can be viewed as a complete $1P$ multiplet formed by spin-1 diquark ss, coupled to the c quark in P-wave. The spin assignment of the states $J = 1/2$(threshold), 1/2, 3/2, 3/2, 5/2 is a plausible hypothesis according to the present analysis.

Chapter 7

Conclusions and outlook

The work presented in this thesis has been focused around the commissioning of the upgraded RICH detector for the LHCb experiment and the observation of excited Ω_c^0 states in the $\Xi_c^+ K^-$ projection in $\Omega_b^- \to \Xi_c^+ K^- \pi^-$ decays.

Firstly, the work completed for the upgraded RICH1 and RICH2 detectors is described. Starting with the study of signal-induced noise of the RICH1 MaPMTs in order to define the installation scheme in the detector. The MaPMTs were divided into groups in terms of quality and spread of the gain, which allowed for the re-shuffling campaign of the photon detectors in the elementary cells to commence. The highest quality MaPMTs have been placed in the high-occupancy regions of the detector. The testing sequence for the commissioning of the RICH2 columns is explained, where all 24 columns have been tested to ensure full operation of the hardware. The new RICH2 columns were installed into the LHCb detector in February 2021. Currently, the LHCb experiment is in the final preparations for the start of Run 3. It has been fully upgraded to handle the increased luminosity, where lots of exciting new measurements will be taken in the coming years.

Secondly, four excited Ω_c^0 states which decay to $\Xi_c^+ K^-$ are observed in the exclusive decay for the first time and correspond to the states seen before in the inclusive decays by the LHCb and Belle experiments. An enhancement at the $\Xi_c^+ K^-$ threshold is seen, and is found to have a significance of 4.6σ. The masses and natural widths of the four main states are measured:

$$
\begin{aligned}
M(\Omega_c(3000)^0) &= 2999.2 \pm 0.9\,(\text{stat}) \pm 0.9(\text{syst})\ \text{MeV}/c^2, \\
\Gamma(\Omega_c(3000)^0) &= 4.8 \pm 2.1\,(\text{stat}) \pm 2.5\,(\text{syst})\ \text{MeV}, \\
N(\Omega_c(3000)^0) &= 23.8 \pm 7.2\,(\text{stat}) \pm 8.4\,(\text{syst}).
\end{aligned}
$$

$$
\begin{aligned}
M(\Omega_c(3050)^0) &= 3050.1 \pm 0.2\,(\text{stat}) \pm 0.2\,(\text{syst})\ \text{MeV}/c^2, \\
\Gamma(\Omega_c(3050)^0) &< 1.2(1.6)\,\text{MeV},\ (90\%)95\%\ \text{CL}, \\
N(\Omega_c(3050)^0) &= 33.1 \pm 6.0\,(\text{stat}) \pm 6.2\,(\text{syst}).
\end{aligned}
$$

$$
\begin{aligned}
M(\Omega_c(3065)^0) &= 3065.9 \pm 0.4\,(\text{stat}) \pm 0.4\,(\text{syst})\ \text{MeV}/c^2, \\
\Gamma(\Omega_c(3065)^0) &= 1.7 \pm 1.0\,(\text{stat}) \pm 0.5\,(\text{syst})\ \text{MeV}, \\
N(\Omega_c(3065)^0) &= 50.8 \pm 8.3\,(\text{stat}) \pm 4.8\,(\text{syst}).
\end{aligned}
$$

$$
\begin{aligned}
M(\Omega_c(3090)^0) &= 3091.0 \pm 1.1\,(\text{stat}) \pm 1.0\,(\text{syst})\ \text{MeV}/c^2, \\
\Gamma(\Omega_c(3090)^0) &= 7.4 \pm 3.1\,(\text{stat}) \pm 2.8\,(\text{syst})\ \text{MeV}, \\
N(\Omega_c(3090)^0) &= 41.4 \pm 9.1\,(\text{stat}) \pm 8.1\,(\text{syst}).
\end{aligned}
$$

where the first error is statistical and the second is systematic. The hypothesis on identifying the states in the 1P multiplet, starting at the $\Omega_c(3000)^0$ peak, is given by:

$$H_0 : 1/2^-,\ 1/2^-,\ 3/2^-,\ 3/2^-.$$

This has been rejected with a significance of 3.5σ. In addition to the above results, a new precise mass of the Ω_b^- is measured:

$$\bar{M}(\Omega_b^-) = 6044.8 \pm 1.3\ \text{MeV/c}^2.$$

The result for the Ω_b^- mass is consistent and competitive with the current PDG value. This work can be found in Ref. [92].

These results will spark further investigation into the Ω_c^{**0} states. One of the states seen in the prompt production of the Ω_c^0 baryons is argued to be a pentaquark candidate, and interestingly wasn't observed to be produced from Ω_b^- decays or in e^+e^- collisions. The larger statistics produced from Run 3 will greatly improve

the sensitivity to the spin measurements. The work completed is essential to understanding the structure of hadrons and can improve our knowledge of HQET.

Bibliography

[1] LHCb collaboration, R. Aaij *et al.*, *Observation of new Ξ_c^0 baryons decaying to $\Lambda_c^+ K^-$*, Phys. Rev. Lett. **124** (2020) 222001, arXiv:2003.13649.

[2] LHCb Collaboration, R. Aaij *et al.*, *Observation of two new excited Ξ_b^0 states decaying to $\Lambda_b^0 K^- \pi^+$*, Phys. Rev. Lett. **128** (2022) 162001.

[3] LHCb Collaboration, *Observation of an exotic narrow doubly charmed tetraquark.*, Nat. Phys. **18** (2022) .

[4] LHCb collaboration, R. Aaij *et al.*, *Observation of New Resonances Decaying to $J/\psi K^+$ and $J/\psi\phi$*, Phys. Rev. Lett. **127** (2021) 082001, arXiv:2103.01803.

[5] LHCb collaboration, R. Aaij *et al.*, *Observation of five new narrow Ω_c^0 states decaying to $\Xi_c^+ K^-$*, Phys. Rev. Lett. **118** (2017) 182001, arXiv:1703.04639.

[6] Particle Data Group, P. A. Zylaet *et al.*, *Review of particle physics*, Prog. Theor. Exp. Phys. **2020** 083C01 (2020) and 2021 update.

[7] LHCb Collaboration, R. Aaij *et al.*, *Evidence for a new structure in the $J/\psi p$ and $J/\psi \overline{p}$ systems in $B_s^0 \to J/\psi p \overline{p}$ decays*, Phys. Rev. Lett. **128** (2022) 062001.

[8] LHCb Collaboration, *Study of the doubly charmed tetraquark T_{cc}^+.*, Nat. Commun. **13** (2022) .

[9] LHCb collaboration, R. Aaij *et al.*, *Observation of a narrow $P_c(4312)^+$ state, and of two-peak structure of the $P_c(4450)^+$*, Phys. Rev. Lett. **122** (2019) 222001, arXiv:1904.03947.

[10] Belle Collaboration, S.-K. Choi *et al.*, *Observation of a narrow charmonium like state in exclusive $B^\pm \to K^\pm \pi^+ \pi^- J/\psi$ decays*, Phys. Rev. Lett. **91** (2003) 262001.

[11] Belle Collaboration, S.-K. Choi *et al.*, *Observation of a resonance like structure in the $\pi^{+-}\psi'$ mass distribution in exclusive $B^0 \to K^\mp \pi^{+-} \psi'$ decays*, Phys. Rev. Lett. **100** (2008) 142001.

[12] LHCb Collaboration, R. Aaij *et al.*, *Observation of $J/\psi p$ resonances consistent with pentaquark states in $\Lambda_b^0 \to J/\psi K^- p$ decays*, Phys. Rev. Lett. **115** (2015) 072001.

[13] LHCb collaboration, R. Aaij *et al.*, *Search for the lepton flavour violating decay $B^+ \to K^+\mu^-\tau^+$ using B_{s2}^{*0} decays*, JHEP **06** (2020) 129, arXiv:2003.04352.

[14] LHCb collaboration, R. Aaij *et al.*, *Test of lepton universality with $\Lambda_b^0 \to pK^-\ell^+\ell^-$ decays*, JHEP **05** (2020) 040, arXiv:1912.08139.

[15] LHCb Collaboration, *Test of lepton universality in beauty-quark decays.*, Nat. Phys. **18** (2022) .

[16] R. Mann, *An Introduction to Particle Physics and the Standard model*, CRC Press, 2010.

[17] K. J. Barnes, *Group Theory for the Standard Model of Particle Physics and Beyond*, CRC Press, 2010.

[18] M. Gell-Mann, *Symmetries of baryons and mesons*, Phys. Rev. **125** (1962) 1067.

[19] Particle Data Group, M. Tanabashi *et al.*, *Review of Particle Physics*, Phys. Rev. **D98** (2018) 030001.

[20] W. Roberts and M. Pervin, *Heavy baryons in a quark model*, Int. J. Mod. Phys. **A23** (2008) 2817, arXiv:0711.2492.

[21] T. Yoshida *et al.*, *Spectrum of heavy baryons in the quark model*, Phys. Rev. **D92** (2015) 114029, arXiv:1510.01067.

[22] N. Isgur and M. B. Wise, *Weak decays of heavy mesons in the static quark approximation*, Phys. Lett. **B232** (1989) 113.

[23] N. Isgur and M. B. Wise, *Weak transition form factors between heavy mesons*, Phys. Lett. **B237** (1990) 527.

[24] B. Grinstein, *The static quark effective theory*, Nucl. Phys. **B339** (1990) 253.

[25] H. Georgi, *An effective field theory for heavy quarks at low energies*, Phys. Lett. **B240** (1990) 447.

[26] E. Eichten and B. R. Hill, *An effective field theory for the calculation of matrix elements involving heavy quarks*, Phys. Lett. **B234** (1990) 511.

[27] A. F. Falk, H. Georgi, B. Grinstein, and M. B. Wise, *Heavy meson form factors from QCD*, Nucl. Phys. **B343** (1990) 1.

[28] A. G. Grozin, *Introduction to the heavy quark effective theory*, arXiv:hep-ph/9908366.

[29] T. Mannel, *Effective theory for heavy quarks*, Lect. Notes Phys. **479** (1997) 387, arXiv:hep-ph/9606299.

[30] S. F. Biagi *et al.*, *Properties of the Charmed Strange Baryon A+ and Evidence for the Charmed Doubly Strange Baryon T0 at 2.74-GeV/c**2*, Z. Phys. C **28** (1985) 175.

[31] G. Chiladze and A. F. Falk, *Phenomenology of new baryons with charm and strangeness*, Phys. Rev. **D56** (1997) R6738, arXiv:hep-ph/9707507.

[32] H.-X. Chen *et al.*, *P-wave charmed baryons from QCD sum rules*, Phys. Rev. **D91** (2015) 054034, arXiv:1502.01103.

[33] M. Padmanath, R. G. Edwards, N. Mathur, and M. Peardon, *Excited-state spectroscopy of singly, doubly and triply-charmed baryons from lattice QCD*, in *Proceedings, 6th International Workshop on Charm Physics (Charm 2013): Manchester, UK, August 31-September 4, 2013*, 2013, arXiv:1311.4806.

[34] H. Garcilazo, J. Vijande, and A. Valcarce, *Faddeev study of heavy baryon spectroscopy*, J. Phys. **G34** (2007) 961, arXiv:hep-ph/0703257.

[35] S. Migura, D. Merten, B. Metsch, and H.-R. Petry, *Charmed baryons in a relativistic quark model*, Eur. Phys. J. **A28** (2006) 41, arXiv:hep-ph/0602153.

[36] D. Ebert, R. N. Faustov, and V. O. Galkin, *Masses of excited heavy baryons in the relativistic quark model*, Phys. Lett. **B659** (2008) 612, arXiv:0705.2957.

[37] Z. Shah, K. Thakkar, A. K. Rai, and P. C. Vinodkumar, *Mass spectra and Regge trajectories of Λ_c^+, Σ_c^0, Ξ_c^0 and Ω_c^0 baryons*, Chin. Phys. **C40** (2016) 123102, arXiv:1609.08464.

[38] M. Padmanath and N. Mathur, *Quantum Numbers of Recently Discovered Ω_c^0 Baryons from Lattice QCD*, Phys. Rev. Lett. **119** (2017) 042001, arXiv:1704.00259.

[39] R. N. Faustov and V. O. Galkin, *Heavy baryon spectroscopy*, EPJ Web Conf. **204** (2019) 08001, arXiv:1811.02232.

[40] M. Praszalowicz, *Exotic interpretation of Ω_c excited states*, in *53rd Rencontres de Moriond on QCD and High Energy Interactions*, 123–126, 2018, arXiv:1805.03862.

[41] K.-L. Wang, L.-Y. Xiao, X.-H. Zhong, and Q. Zhao, *Understanding the newly observed Ω_c states through their decays*, Phys. Rev. **D95** (2017) 116010, arXiv:1703.09130.

[42] H.-Y. Cheng and C.-W. Chiang, *Quantum numbers of Ω_c states and other charmed baryons*, Phys. Rev. D **95** (2017) 094018.

[43] S. Capstick and N. Isgur, *Baryons in a relativized quark model with chromodynamics*, Phys. Rev. **D34** (1986) 2809.

[44] H. Huang, J. Ping, and F. Wang, *Investigating the excited Ω_c^0 states through $\Xi_c\bar{K}$ and $\Xi_c'\bar{K}$ decay channels*, Phys. Rev. **D97** (2018) 034027, arXiv:1704.01421.

[45] Z. Zhao, D.-D. Ye, and A. Zhang, *Hadronic decay properties of newly observed Ω_c baryons*, Phys. Rev. **D95** (2017) 114024, arXiv:1704.02688.

[46] B. Chen and X. Liu, *New Ω_c^0 baryons discovered by LHCb as the members of $1P$ and $2S$ states*, Phys. Rev. **D96** (2017) 094015, arXiv:1704.02583.

[47] S.-Q. Luo, B. Chen, X. Liu, and T. Matsuki, *Predicting a new resonance as charmed-strange baryonic analog of $D_{s0}^*(2317)$*, Phys. Rev. **D103** (2021) 074027, arXiv:2102.00679.

[48] V. O. Galkin and R. N. Faustov, *Heavy baryon spectroscopy*, Phys. Part. Nucl. **51** (2020) 661.

[49] Z. Shah, K. Thakkar, A. Kumar Rai, and P. C. Vinodkumar, *Excited State Mass spectra of Singly Charmed Baryons*, Eur. Phys. J. A **52** (2016) 313, arXiv:1602.06384.

[50] M. Karliner and J. L. Rosner, *Very narrow excited Ω_c baryons*, Phys. Rev. D **95** (2017) 114012, arXiv:1703.07774.

[51] S. S. Agaev, K. Azizi, and H. Sundu, *Interpretation of the new Ω_c^0 states via their mass and width*, Eur. Phys. J. **C77** (2017) 395, arXiv:1704.04928.

[52] H.-X. Chen *et al.*, *Decay properties of P-wave charmed baryons from light-cone QCD sum rules*, Phys. Rev. **D95** (2017) 094008, arXiv:1703.07703.

[53] Z.-G. Wang, *Analysis of $\Omega_c(3000)$, $\Omega_c(3050)$, $\Omega_c(3066)$, $\Omega_c(3090)$ and $\Omega_c(3119)$ with QCD sum rules*, Eur. Phys. J. **C77** (2017) 325, arXiv:1704.01854.

[54] R. Chen, A. Hosaka, and X. Liu, *Searching for possible Ω_c-like molecular states from meson-baryon interaction*, Phys. Rev. **D97** (2018) 036016, arXiv:1711.07650.

[55] H.-C. Kim, M. V. Polyakov, and M. Praszałowicz, *Possibility of the existence of charmed exotica*, Phys. Rev. **D96** (2017) 014009, Erratum ibid. **D96** (2017) 039902, arXiv:1704.04082.

[56] C. S. An and H. Chen, *Observed Ω_c^0 resonances as pentaquark states*, Phys. Rev. **D96** (2017) 034012, arXiv:1705.08571.

[57] A. Ali *et al.*, *A new look at the Y tetraquarks and Ω_c baryons in the diquark model*, Eur. Phys. J. **C78** (2018) 29, arXiv:1708.04650.

[58] G. Montaña, A. Feijoo, and A. Ramos, *A meson-baryon molecular interpretation for some Ω_c excited states*, Eur. Phys. J. **A54** (2018) 64, arXiv:1709.08737.

[59] V. R. Debastiani, J. M. Dias, W. H. Liang, and E. Oset, *Molecular Ω_c states generated from coupled meson-baryon channels*, Phys. Rev. **D97** (2018) 094035, arXiv:1710.04231.

[60] ARGUS Collaboration, J. Stiewe, *Proceedings of the international conference on high energy physics*, .

[61] P. Frabetti *et al.*, *Observation and mass measurement of $\Omega_c^0 \to \Sigma^+ k^- k^- \pi^+$*, Phys. Lett. B **338** (1994) 106.

[62] CLEO Collaboration, D. Cronin-Hennessy *et al.*, *Observation of the Ω_c^0 charmed baryon at CLEO*, Phys. Rev. Lett. **86** (2001) 3730.

[63] BaBar collaboration, B. Aubert *et al.*, *Observation of an excited charm baryon Ω_c^{*0} decaying to Ω_c^0 gamma*, Phys. Rev. Lett. **97** (2006) 232001, arXiv:hep-ex/0608055.

[64] LHCb collaboration, R. Aaij *et al.*, *First observation of the decay $B_{s2}^*(5840)^0 \to B^{*+}K^-$ and studies of excited B_s^0 mesons*, Phys. Rev. Lett. **110** (2013) 151803, arXiv:1211.5994.

[65] LHCb collaboration, R. Aaij *et al.*, *Measurements of the mass and lifetime of the Ω_b^- baryon*, Phys. Rev. **D93** (2016) 092007, arXiv:1604.01412.

[66] E. Mobs, *The CERN accelerator complex - 2019. Complexe des accélérateurs du CERN - 2019*, , General Photo.

[67] LHCb collaboration, A. A. Alves, Jr. *et al.*, *The LHCb Detector at the LHC*, JINST **3** (2008) S08005.

[68] C. Elsässer, *$\bar{b}b$ production angle plots*, lhcb.web.cern.ch/speakersbureau/html/bb_ProductionAngles.html, Accessed: 06-10-2021.

[69] LHCb Online collaboration, *Lhcb operations plots webpage*, lbgroups.cern.ch/online/OperationsPlots/index.htm, Accessed: 07-10-2021.

[70] LHCb Outer Tracker Group, R. Arink *et al.*, *Performance of the LHCb Outer Tracker*, JINST **9** (2014) P01002, arXiv:1311.3893.

[71] LHCb calorimeter group, I. Machikhiliyan, *The LHCb electromagnetic calorimeter*, J. Phys. : Conf. Ser. 160 **012047** (2009).

[72] LHCb collaboration, R. Aaij *et al.*, *Design and performance of the LHCb trigger and full real-time reconstruction in Run 2 of the LHC*, JINST **14** (2019) P04013, arXiv:1812.10790.

[73] *Letter of Intent for the LHCb Upgrade* , CERN, Geneva, 2011.

[74] L. Collaboration, *LHCb Tracker Upgrade Technical Design Report* , 2014.

[75] LHCb collaboration, M. Andreotti *et al.*, *Characterisation of signal-induced noise in Hamamatsu R11265 Multianode Photomultiplier Tubes*, JINST **16** (2021) P11030, arXiv:2110.00831.

[76] Hamamatsu Photonics collaboration, *Photomultiplier tubes, basics and applications, fourth edition*, www.hamamatsu.com/content/dam/hamamatsu-photonics/sites/documents/99_SALES_LIBRARY/etd/PMT_handbook_v4E.pdf, 2017.

[77] T. Sjöstrand, S. Mrenna, and P. Skands, *A brief introduction to PYTHIA 8.1*, Comput. Phys. Commun. **178** (2008) 852, arXiv:0710.3820; T. Sjöstrand, S. Mrenna, and P. Skands, *PYTHIA 6.4 physics and manual*, JHEP **05** (2006) 026, arXiv:hep-ph/0603175.

[78] I. Belyaev *et al.*, *Handling of the generation of primary events in Gauss, the LHCb simulation framework*, J. Phys. Conf. Ser. **331** (2011) 032047.

[79] D. J. Lange, *The EvtGen particle decay simulation package*, Nucl. Instrum. Meth. **A462** (2001) 152.

[80] Geant4 collaboration, J. Allison *et al.*, *Geant4 developments and applications*, IEEE Trans. Nucl. Sci. **53** (2006) 270; Geant4 collaboration, S. Agostinelli *et al.*, *Geant4: A simulation toolkit*, Nucl. Instrum. Meth. **A506** (2003) 250.

[81] LHCb collaboration, R. Aaij *et al.*, *Measurement of the Ω_c^0 lifetime*, Phys. Rev. Lett. **121** (2018) 092003, arXiv:1807.02024.

[82] LHCb collaboration, R. Aaij *et al.*, *Search for CP violation in $\Xi_c^+ \to pK^-\pi^+$ decays with model-independent techniques*, arXiv:2006.03145, submitted to JHEP.

[83] LHCb Collaboraton collaboration, R. Aaij *et al.*, *Precision Measurement of D meson mass differences*, JHEP (2013) , arXiv:1304.6865.

[84] H. Voss, A. Hoecker, J. Stelzer, and F. Tegenfeldt, *TMVA - Toolkit for Multivariate Data Analysis with ROOT*, PoS **ACAT** (2007) 040; A. Hoecker *et al.*, *TMVA 4 — Toolkit for Multivariate Data Analysis with ROOT. Users Guide.*, arXiv:physics/0703039.

[85] G. Punzi, *Sensitivity of searches for new signals and its optimization*, eConf **C030908** (2003) MODT002, arXiv:physics/0308063.

[86] G. A. Cowan, D. C. Craik, and M. D. Needham, *RapidSim: an application for the fast simulation of heavy-quark hadron decays*, Comput. Phys. Commun. **214** (2017) 239, arXiv:1612.07489.

[87] LHCb collaboration, R. Aaij *et al.*, *Measurements of the Λ_b^0, Ξ_b^-, and Ω_b^- baryon masses*, Phys. Rev. Lett. **110** (2013) 182001, arXiv:1302.1072.

[88] M. Schmelling, *Averaging correlated data*, Phys. Scr. **51** (1994) 676.

[89] G. Ranucci, *The profile likelihood ratio and the look elsewhere effect in high energy physics*, Nuclear Instruments and Methods in Physics Research Section A: Accelerators, Spectrometers, Detectors and Associated Equipment **661** (2012) 77.

[90] JPAC collaboration, M. Mikhasenko *et al.*, *Dalitz-plot decomposition for three-body decays*, Phys. Rev. D **101** (2020) 034033, arXiv:1910.04566.

[91] LHCb collaboration, R. Aaij *et al.*, *Precision measurement of D meson mass differences*, JHEP **06** (2013) 065, arXiv:1304.6865.

[92] LHCb Collaboration, R. Aaij *et al.*, *Observation of excited Ω_c^0 baryons in $\Omega_b^- \to \Xi_c^+ K^- \pi^-$ decays*, Phys. Rev. D **104** (2021) L091102.